Doppler Lidar Vector Retrievals

and

Atmospheric Data Visualization in Mixed/Augmented Reality

by

Nihanth Wagmi Cherukuru

A Dissertation Presented in Partial Fulfillment
of the Requirements for the Degree
Doctor of Philosophy

Approved April 2017 by the
Graduate Supervisory Committee:

Ronald Calhoun, Chair
Rob Newsom
Huei-Ping Huang
Kangping Chen
Werner Dahm

ARIZONA STATE UNIVERSITY

May 2017

ABSTRACT

Environmental remote sensing has seen rapid growth in the recent years and Doppler wind lidars have gained popularity primarily due to their non-intrusive, high spatial and temporal measurement capabilities. While lidar applications early on, relied on the radial velocity measurements alone, most of the practical applications in wind farm control and short term wind prediction require knowledge of the vector wind field. Over the past couple of years, multiple works on lidars have explored three primary methods of retrieving wind vectors viz., using homogeneous windfield assumption, computationally extensive variational methods and the use of multiple Doppler lidars.

Building on prior research, the current three-part study, first demonstrates the capabilities of single and dual Doppler lidar retrievals in capturing downslope windstorm-type flows occurring at Arizona's Barringer Meteor Crater as a part of the METCRAX II field experiment. Next, to address the need for a reliable and computationally efficient vector retrieval for adaptive wind farm control applications, a novel 2D vector retrieval based on a variational formulation was developed and applied on lidar scans from an offshore wind farm and validated with data from a cup and vane anemometer installed on a nearby research platform. Finally, a novel data visualization technique using Mixed Reality (MR)/ Augmented Reality (AR) technology is presented to visualize data from atmospheric sensors. MR is an environment in which the user's visual perception of the real world is enhanced with live, interactive, computer generated sensory input (in this case, data from atmospheric sensors like Doppler lidars). A methodology using modern game development platforms is presented and demonstrated with lidar retrieved wind fields. In the current study, the possibility of using this

technology to visualize data from atmospheric sensors in mixed reality is explored and demonstrated with lidar retrieved wind fields as well as a few earth science datasets for education and outreach activities.

"We keep moving forward, opening new doors, and doing new things,

because we're curious and curiosity keeps leading us down new paths."

- Walt Disney

To my advisor, Dr. Ronald Calhoun,

who taught me to keep my curiosity alive and to not be afraid of opening new doors…

ACKNOWLEDGMENTS

Firstly, I would like to express my deepest appreciation to my advisor, Dr. Ronald Calhoun for the continuous support, patience and motivation in all my scholarly endeavors. I am also grateful to my committee members, Dr. Rob Newsom, Dr. Huei Ping Huang, Dr. Werner Dahm and Dr. Kang Ping Chen for their precious time in offering their valuable suggestions and feedback.

The material presented in this dissertation was supported by the National Science Foundation (NSF) grants AGS-1160730, US Navy Neptune Program, ASU Lightworks; without whom, this work would not have been possible. I also appreciate the valuable inputs and mentorship of former graduate students Dr. Aditya Choukulkar and Dr. Raghavendra Krishnamurthy as well as the wonderful company of my fellow PhD students Sreevatsan Bhaskaran and Kai Zhou.

Special thanks to Tim Scheitlin, Matt Rehme, Dr. Raghu Raj Prasanna Kumar and Dr. Richard Loft of the Computational and Information Systems Laboratory at NCAR for their wonderful mentorship and collaboration in the mobile augmented reality research. Last but not the least, I would like to thank my parents and my fiancée for their unconditional love and support throughout.

TABLE OF CONTENTS

Page

CHAPTER Page

LIST OF TABLES

LIST OF FIGURES

Figure Page

Figure Page

Figure Page

Figure Page

CHAPTER 1

INTRODUCTION

Lidar (acronym for 'Light detection and ranging') is a remote sensing device that works by emitting laser radiation and analyzing the backscattered light. Among the different types of lidars, pulsed-coherent Doppler lidars (referred as Doppler Lidar from now on) measure, range resolved, line of sight wind velocity in the atmosphere. There is a growing body of literature, ranging from meteorology (e.g. Banta et al., 1996; Choukulkar et al., 2012; Newsom & Banta, 2003), wind resource assessment (Frehlich & Kelley, 2008; Krishnamurthy, et al. 2013) and aviation safety (Shun & Chan, 2008; Shun, 2003) ever since Doppler lidars were first used in environmental remote sensing for measuring wind fields. With the recent commercial availability & affordability of compact solid state lidars, the use of multiple lidars in Dual-Doppler and multiple-Doppler modes is becoming more feasible. In this chapter, a brief description of the measurement principle of Doppler lidars, along with the description of popular vector retrievals is presented.

1.1 Coherent Doppler Lidar Working Principle

As the name suggests, a Doppler lidar obtains the line of sight velocity by measuring the Doppler shift of particles (aerosols) in the atmosphere. A coherent Doppler lidar first sends an eye-safe infrared laser pulse into the atmosphere. Due to the particular wavelength regime (i.e., in the infrared range ~1.5μm – 2 μm), this laser beam is scattered back by aerosols (e.g., dust, pollen, sea salt etc.) transported by the wind, as the pulse travels through the atmosphere. Backscattered light is collected by a transceiver

(a transmitter and a receiver in a single unit) and optically mixed with a continuous wave laser (Local Oscillator, LO) from which the initial laser pulses were derived (See Figure 1). This mixing process (heterodyning) results in an optical signal with a frequency corresponding to the difference between the LO frequency and the backscattered field (i.e., beat frequency) which is then passed onto a photo detector with a pass band corresponding expected range of Doppler shift frequencies. The resulting signal from the photo detector will be of the form

$$s(t) \propto \cos\left[\left(\delta\omega_{doppler} + \omega_{transmitted} + \omega_{intermediate} - \omega_{LO}\right)t + \Delta\varphi\right] \quad (1.1)$$

where, $\delta\omega_{doppler}$ is the Doppler shift in frequency (the main quantity of interest) (Newsom, 2012). In an ideal case, $\omega_{transmitted}$(frequency of the transmitted pulse) will be equal to ω_{LO} (frequency of the local oscillator) and they cancel each other out. $\omega_{intermediate}$ is a small frequency shift added to the outgoing pulse. At this stage, one of the popular methods to obtain $\delta\omega_{doppler}$ is from the Fourier transform of the autocovariance of the signal given in Eq. (1.2). Since the signal from the atmosphere is inherently noisy, to reduce the effect of noise, the complex autocovariance at each range gate is accumulated/averaged over a number of pulses prior to the Doppler frequency detection stage. Although increasing the averaging reduces the frequency of measurement, the SNR of the Doppler spectrum increases as the square root of the number of pulses that are averaged (Cariou & Boquet, 2011). From the Doppler shift frequency, the velocity is determined by

$$V_r = -\frac{\lambda}{2}.\frac{\delta\omega_{doppler}}{2\pi} \quad (1.2)$$

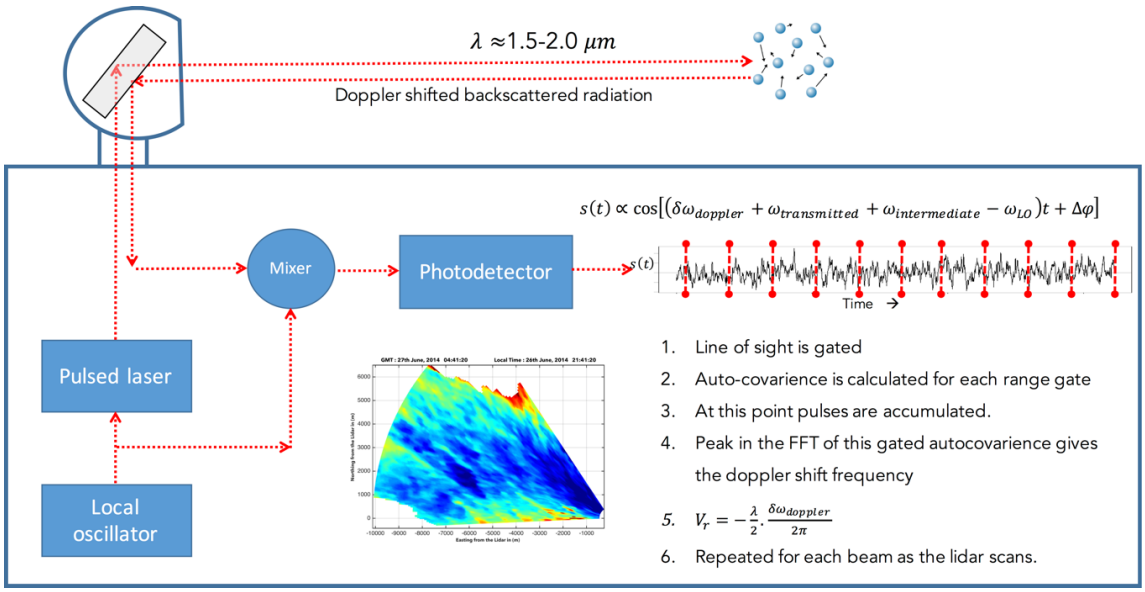

Figure 1. Working principle of a coherent Doppler lidar

where, λ is the wavelength of outgoing laser radiation, V_r is the line of sight velocity (referred to as radial velocity from this point forward) (Newsom, 2012). In the absence of $\omega_{intermediate}$ (See Eq (1.1)), both positive and negative Doppler shifts would result in the same Fourier spectrum due to the cosine term encompassing $\delta\omega_{doppler}$. By adding this known frequency ($\omega_{intermediate}$) to the outgoing pulse, positive and negative Doppler shifts could be uniquely determined about this intermediate frequency.

In addition to the velocity along the line of sight, most of the commercially available Doppler lidars report signal to noise ratio (A measure of signal strength to noise strength in the spectral domain), backscatter (most simply, SNR adjusted for the signal degradation with range) and spectral width (width of the spectrum around the Doppler shift frequency peak, e.g., full width at half the maximum value). By means of mirrors

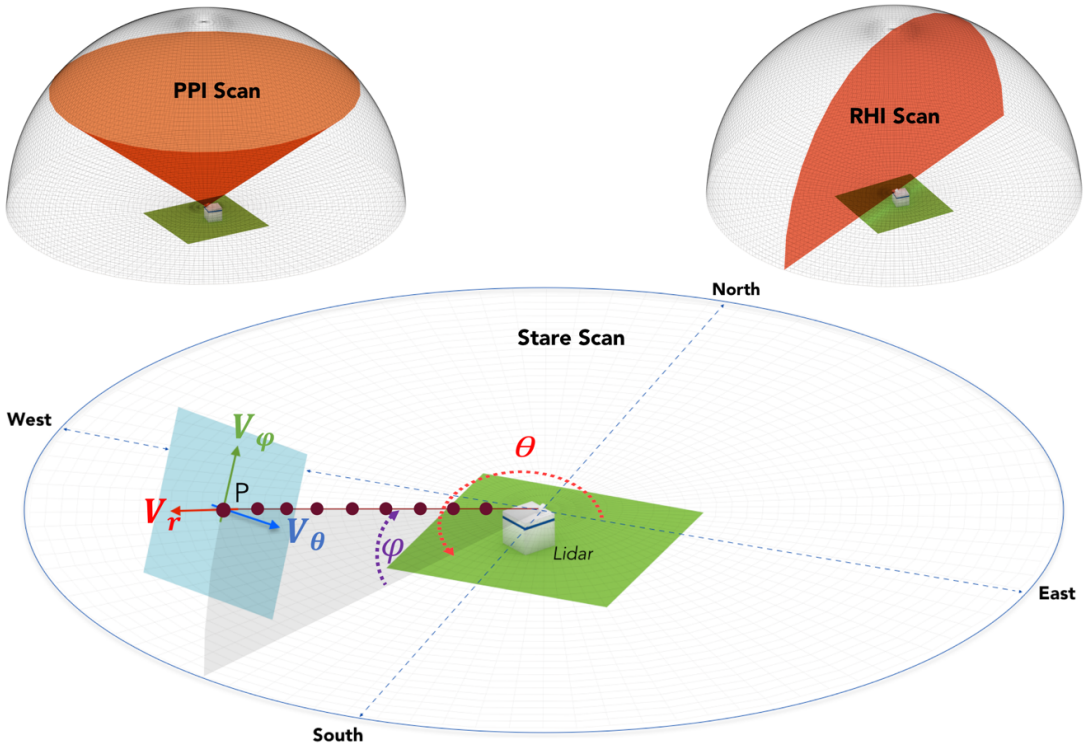

Figure 2. Common scan configurations- PPI, RHI and stare scan. θ is the azimuth angle (angle measured in the horizontal plane) and φ is the elevation angle (angle measured in the vertical plane). V_r, V_φ and V_θ are the three velocity components at a point 'P' in the lidar's spherical coordinate system. The lidar measures V_r. The dots along the beam represent range gates.

fixed in a rotating scanning head, the lidar beam can be pointed in any direction in the hemisphere, to map the surrounding winds. Three fundamental scan configurations can be set up to map the domain of interest: (a) Range Height Indicator scans (RHI scans): where in the azimuthal angle is fixed and the lidar performs a scan in the vertical plane,

(b) Plan Position Indicator scans (PPI scans): where the elevation angle is fixed and the lidar performs a conical scan along the azimuthal direction, and (c) Stare: where the lidar fixes both the azimuth and elevation angle to obtain the time varying LOS velocity measurement (See Figure 2).

1.2 What Is Radial Velocity?

Consider a Doppler lidar positioned at some location and scanning the atmosphere around it. At any given instant of time, the pointing direction of the scanning head (and the lidar beam) can be determined using the azimuth and elevation angles (θ, φ). For instance, a value of (0°,0°) would correspond to the lidar beam directed parallel to the ground pointing to the East (See Figure 2). Let (u,v,w) be the Cartesian velocity components of the wind vector at some point (P) in space (see Figure 2). The Cartesian velocity components and their spherical counterparts (V_r, V_θ, V_φ), at this location, are related by the following equations:

$$V_r = u.cos\theta cos\varphi + v.sin\theta cos\varphi + w.sin\varphi \quad (1.3a)$$

$$V_\theta = -u.sin\theta + v.cos\theta \quad (1.3b)$$

$$V_\varphi = -u.cos\theta sin\varphi - v.sin\theta sin\varphi + w.cos\varphi \quad (1.3c)$$

where, V_r is the component of velocity along the lidar's line of sight, V_θ is the tangential component of velocity in the azimuthal direction, and V_φ is the tangential component of velocity perpendicular to both V_r and V_θ. As mentioned earlier, a lidar can only measure the Doppler shift corresponding to the radial velocity component (V_r, See Eq (1.3a)) and thus, 3D-wind field reconstruction from a single measurement results in an

underdetermined linear system with infinite number of solutions necessitating additional models or assumptions regarding the flow to close the linear system.

1.3 Wind Retrievals

Most of the existing flow field reconstruction algorithms rely on one of the following: a) Homogeneous wind field assumption, b) Variational methods based on computational fluid dynamics (CFD) models, c) Use of multiple Doppler lidars.

1.3.1 Retrievals based on homogeneous wind field assumption.

By far the most popular and widely used retrievals, in these retrievals, the velocity field is assumed to be horizontally homogeneous/uniform within a certain analysis region. This facilitates the vector wind field reconstruction by combining radial velocity measurements from multiple look angles to determine the vector field which fits best with the measurements. Velocity azimuth display (VAD), sector-VAD, Volume Velocity Processing, and Doppler Beam Swing (DBS) retrievals fall in this category.

a) ***Velocity Azimuth Display (VAD).*** Velocity Azimuth Display (VAD) is named after the plot used to visualize the radial velocity product from a 360° PPI scan at a fixed range gate (Figure 3a). For a given elevation angle 'φ' the lidar is configured to perform a full 360°, conical scan. When the flow is assumed to be horizontally homogeneous in the area swept by the scan and the lidar is perfectly leveled with the ground, the radial velocity measurements from any fixed height can be expressed as a function of azimuth alone (Figure 3b). This radial velocity equation has a characteristic of a sinusoid (Lehremitte and Atlas, 1961) whose

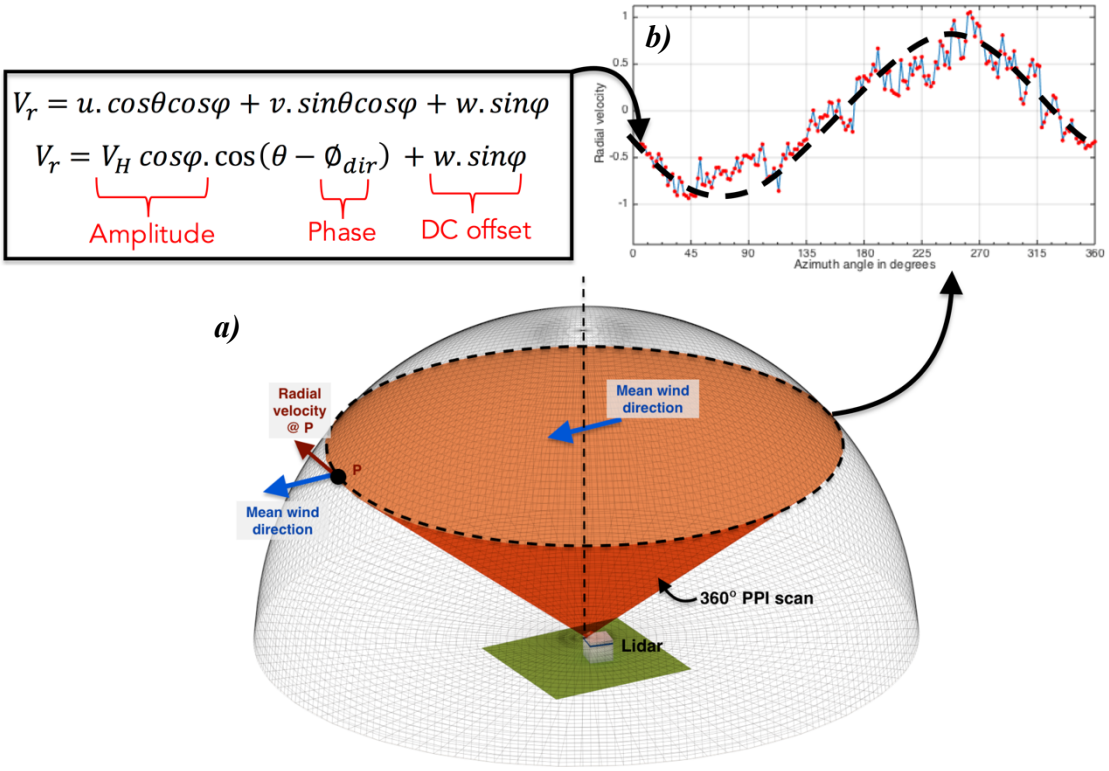

Figure 3. a) A 360° azimuth coverage PPI scan at a fixed elevation angle showing the velocity azimuth display (VAD) plot (b). In the red dots depict radial velocity measurements for each line of sight and the vector field which best fits the equation is shown with a black dotted line. The amplitude, phase and DC offset of the best fit sinusoid correspond to the horizontal wind speed, wind direction and vertical velocity respectively.

amplitude corresponds to the horizontal wind speed, phase corresponds to the wind direction and the DC shift corresponds to the vertical velocity component. Thus, the algorithm basically involves determining the sinusoid that best fits the given radial velocity measurements and repeating the process for each range gate

to produce vertical profiles of the three components of wind velocity. VAD was first developed for Doppler radars and different methods for obtaining the best fit sinusoid were explored by previous works including Fourier series expansion (Browning & Wexler, 1968; Lehermitte & Miller, 1970), Least squares approach (Boccippio, 1995), quadratic curve fitting at the maximum (Siemen & Holt, 2000) and combining scans from multiple elevation (Extended VAD or EVAD-Srivastava et al., 1986).

The main disadvantage of VAD stems from the homogeneity assumption which only holds when in stable atmospheric conditions. Also, there is a trade-off between shorter sampling time and the stability of the algorithm. Due to the presence of turbulence and lidar data being noisy, the stability of the retrieval is dependent on the number of radial velocity measurements at each elevation (i.e., number of lines of sight). However, increasing the density typically involves either reducing the pulse averaging (which could increase the noise in the measurements) or decreasing the scan speed (which could invalidate the homogeneity assumption).

a) ***Doppler Beam Swing (DBS).*** Doppler beam swinging (DBS) is an extension of VAD which could be used to retrieve vertical profiles of the wind vector from only a few beams as opposed to a full 360° conical scan. The measurements must be taken from at least two orthogonal azimuths and the vertical to retrieve all the components (e.g. Lane et al., 2013, Lundquist et al., 2015). DBS has an advantage of having shorter acquisition times thereby reducing the errors caused

due to the deviation from the uniform wind field assumption. However, DBS retrieval is more sensitive to noise than VAD and a least squares minimization is typically implemented to obtain the best fit primarily due to it stability in noisy conditions.

b) ***Volume Velocity Processing (VVP).*** VVP works on a similar principle as VAD to retrieve 2D and 3D vector fields from multiple PPI scans. The algorithm involves decomposing the spatial region covered by the lidar scan(s) into 2D (or 3D) sections and fitting the radial velocity measurements within each volume to a simple linear wind model (Eq. (1.3a)) to obtain the three components of velocity (Koscielny et al., 1982; Doviak & Zrnic, 1993, Boccippio, 1995). Arc scans, work on a similar formulation like VVP, but applied on PPI sectors (Wang et al., 2015) as opposed to a full volume. The sectors (or analysis volumes) must be chosen such that the rage of azimuth angles of individual lines of sight span at least 30°, for the fluctuations in radial velocity caused by the change in look angle to be higher than the turbulent fluctuations (Clifton, 2015).

1.3.2 Retrievals based on variational methods.

Variational methods obtain the vector wind field by minimizing a cost function comprising of constraint equations deduced from the observations. These methods have an advantage of handling some degree of inhomogeneity of the wind field (Clifton et al., 2015). 2D/3D-VAR, 4D-VAR and Optimal Interpolation fall in this category. The in depth literature pertaining to these methods is given in Chapter 3.

1.3.3 Use of simultaneous multiple Doppler lidars.

The idea behind multiple Doppler configuration is to setup different lidars such that each lidar probes, concurrently, the same volume in space from three different directions (ideally, three orthogonal directions) to reconstruct the 3D velocity vector using:

$$V_{ri} = u.cos\theta_i cos\varphi_i + v.sin\theta_i cos\varphi_i + w.sin\varphi_i \quad (1.4)$$

where, V_{ri} is the radial velocity measured from the ith lidar, i =1,2(Dual Doppler) or 3 (triple doppler) correspond to each Lidar. The three equations in Eq (1.4) can be solved for the three unknowns (u, v, w). Multiple lidars could be used for high temporal measurements at a single point (rather a pulse volume) in space (Mann et al., 2008, Mikkelsen et al., 2008, Newman et al., 2015), along a vertical line (Calhoun et al., 2006) and 2D spatial measurements (Rothermel et al., 1985, Newsom et al., 2008). The majority of previous works have been limited to two Doppler lidars due to the higher costs associated with the operating multiple units.

One of the first Dual-Doppler Lidar analyses using periodic coordinated scans was described by Rothermel et al. (1985) in the context of the Joint Airport Weather Studies (JAWS) experiment. A configuration described in Collier et al. (2005) sought to intersect the two lidar beams at precise points in space to obtain turbulence measurements with short time averages. Calhoun et al. (2006) devised a method to obtain mean vertical profiles of velocity at a large number of intersections ("virtual towers") using two Doppler lidars in Joint Urban 2003 atmospheric dispersion study (JU 2003). Coplanar PPI scans (Newsom et al., 2008) and coplanar RHI scans (Hill et al., 2010) were used to

extract wind fields in the scan overlap region giving new insights into the flow structures. An analysis of errors associated with dual-Doppler lidar turbulence measurements was described in Davis et al., (2005). Stawiarski et al., (2013) gave an overview of the errors caused by non-optimal scanning techniques and instrument configuration. Another advantage of using multiple Doppler lidars is that, 3D wind components and their statistics could be retrieved with high temporal resolution making them ideal for turbulence studies is the atmosphere (Mann et al. 2008, Newman et al. 2015).

Since, the present study focuses on vector wind retrievals, works related to the measurement of turbulence statistics from single Doppler lidars were not included in the previous section. A detailed review of turbulence measurements using ground based Doppler lidars is presented by Sathe & Mann (2013) and Sathe et al. (2015). In general, the measurement of turbulence statistics from single Doppler lidars remains to be a challenging field due to the inherent averaging involved in obtaining the radial velocity from a 30m-100m probing volume (range gate). Due to this most of the previous works involved determining unfiltered turbulence statistics by combining raw lidar measurements with an isotropic turbulence model (Krishnamurthy et al., 2011, Sathe et al., 2011). Alternate methods involve retrieving the Reynolds stress components by combining multiple VAD type scans (Eberhard et al., 1989), combining data from two orthogonal RHI scans to retrieve dissipation and other turbulence statistics (Gal-Chen et al., 1992) and a six beam method to obtain the Reynolds stress components from the radial velocity variances obtained from five equally spaced azimuthal stare scans and a vertical stare (Sathe et al., 2015).

Table 1.1

Popular retrieval algorithms

Retrieval	Scans	Advantages	Limitations
Vertical Profiles			
Velocity Azimuth Display (VAD)	A full 360° conical scan at a fixed elevation angle	• Retrieves vertical profiles of velocity • Fast runtime • Stable, Reliable estimates in simple flows	• Horizontal homogeneity assumption of the wind field • Long acquisition time
Doppler Beam Swing (DBS)	Combination of stare scans	• Retrieves vertical profiles of velocity • Faster than VAD	• Horizontal homogeneity assumption of the wind field • More sensitive to noise than VAD
*Virtual Towers	Two RHI scans/ two RHI scans and a vertical stare in the scan intersection region	• Can produce vertical profiles of wind in complex flow conditions	• Requires atleast two lidars • The angle subtended by any to lines of sight from each lidar must be atleast 30°
6-beam method	5 equally spaced azimuth scans and one vertical stare and uses	• Can measure TKE and velocity variances	• Probe volume averaging affects the

	radial velocity variance measurement	• Measurement errors and bias are independent of height	turbulence measurements
Turbulence retrievals from conical scans	VAD type conical scans with a vertical stare	• Can retrieve velocity variances, TKE and covariances	• Measurements are less reliable and biased for low elevation scans
2D, 3D vector fields			
Retrieval	**Scans**	**Advantages**	**Limitations**
Volume Velocity Processing (VVP)	Stack of PPIs	• Can retrieve 2D,3D vector fields	• Only valid when the flow field is horizontally homogeneous within each retrieval volume
Sector VAD/ Arc scans	PPI scans	• Can retrieve vectors along a sector for each range gate • Comparatively fast	• Only valid when the flow field is horizontally homogeneous • Angle limitation
2D,3D-VAR; Optimal Interpolation (OI)	PPI scans/ Stack of PPI scans	• Can retrieve vectors along a plane or 3D space	• Depending on the optimization scheme used, the retrieval could be slow

		• Can handle complex flow situations	• Limited by the validity of the constraints used • OI can be used only scans at low elevation angles • OI in the current formulation is not fully automated and needs user input for the weights which vary based on the type of flow
4D-VAR	PPI/ Stack of PPI scans	• High spatial and temporal resolution retrievals	• Computationally expensive • Accuracy is limited by the assumptions of the underlying model
*Co-planar dual Doppler scans	Two RHI/PPI scans	• 2D profiles with comparatively high spatial resolutions can be obtained	• Higher operational cost • Might be difficult to coordinate the lidars

*Triple Doppler lidar scans	Combination of stare scans Or Virtual tower with a stare at the scan intersection	• Suitable for turbulence measurements • Very high temporal resolution	• Higher operational cost • Difficult to coordinate the three lidars • Might not be suitable for all deployments depending on the surrounding topography

** Dual/ Multiple Doppler lidar technique*

1.4 Objectives of The Present Study

This dissertation has three sections aimed at exploring the capabilities of existing retrieval algorithms in capturing complex atmospheric phenomenon, the development of a novel fast 2D-VAR algorithm to address the need for an efficient vector retrieval for complex flows, and the demonstration of a novel Mixed reality/Augmented Reality based data visualization technique for atmospheric data. The objectives of each of these sections are given below.

Section I. Various single and dual Doppler lidars along with a suite of other weather sensors were used to capture downslope windstorm-type flows occurring at Arizona's Meteor Crater as a part of the second Meteor Crater Experiment (METCRAX II) during calm, undisturbed nights. A description of the methodology, scan patterns and the error analysis are given in chapter 2.

The research objectives of this section are:

- To design a coplanar dual-Doppler lidar scan strategy to capture downslope windstorm-type flows occurring in Arizona's Barringer Meteor Crater
- To design single Doppler lidar scan strategies required to capture the upstream flow at the crater
- To perform an error analysis to identify potential sources of errors in the retrievals employed in METCRAX II

Section II. Applications like wind power forecasting and dynamic wind turbine control require a reliable retrieval algorithm with real-time application capabilities. To

address this need, a novel 2D-VAR retrieval was developed and tested on lidar data from an onshore wind farm in Tehachapi, CA and the Alta Ventus windfarm located in the North Sea, the details of which are given in chapter 3. The general retrieval is based on the minimization of a cost function comprised of the radial velocity advection, radial velocity, tangential velocity and background equations.

The research objectives of this section are:

- To develop a 2D-VAR retrieval capable of preserving small scale flow structures, while being computationally efficient to have real-time application capabilities
- To test the retrieval on lidar data in a complex flow scenario
- To assess the accuracy of the retrieval using data from other instruments in the field

Section III. Given the improving capabilities of atmospheric sensors and the ability to acquire 2D-3D measurements with higher spatial and temporal resolutions, a new data visualization method based on mixed/augmented reality (MR/AR) is presented in chapter 4. This visualization technique allows users to view the sensor data anchored to the real world objects when viewed through a hand-held or head mounted display making the data visualization task more intuitive. The AR technique is demonstrated on a tablet computer with the dual- Doppler lidar data acquired during METCRAX II. The application was further extended to earth science datasets for education and outreach activities through a smartphone, iPad application developed in collaboration with the National Center for Atmospheric Research (NCAR).

The research objectives of this section are:

- To explore the use of Mixed/Augmented reality technique to visualize Doppler lidar (any atmospheric sensor data)
- To develop the visualization application using popular game development platforms
- Demonstrate the application using lidar data from METCRAX II
- Demonstrate the application on earth science datasets for education and outreach activities

CHAPTER 2

CASE STUDY: LIDARS IN THE SECOND METEOR CRATER EXPERIMENT (METCRAX II)

During the fall of 2013, multiple Doppler lidars along with a suit of other meteorological instruments were deployed at the Arizona's Barringer Meteor Crater to study downslope-windstorm type flows occurring there. This chapter describes the lidar experimental setup, scan strategies and different single and multiple Doppler lidar vector retrieval techniques employed to obtain vertical profiles of the wind as well as 2D cross sections of the flows inside the crater.

2.1 Downslope Windstorms

Downslope windstorms are very strong, gusty and occasionally violent surface winds that blow down the steep lee slope of a mountain range (Durran, 2003). These

Figure 4. Aerial view of the crater looking southeast. Photograph by Shane Torgerson , CC BY 3.0

windstorms occur frequently near foothills of mountains and are known to cause substantial damage to life and property (Whiteman & Whiteman, 1974).

Arizona's Barringer Meteor Crater (Figure 4), located 40 km east of Flagstaff in Northern Arizona, was formed by a meteorite impact that occurred approximately 50,000 years ago. The crater has a bowl-shaped morphology with a diameter of 1.2 km and a depth of 180 m. The crater rim rises 30-60 m above the surrounding plain (Kring, 2007). During the first Meteor Crater experiment (METCRAX) field campaign in 2006, short lived, episodic nocturnal warm air intrusions were detected on the west sidewall of the crater, while studying the characteristics of stable nocturnal boundary layer in basin (Whiteman et al., 2008). These high wind and high turbulence events bore resemblance to downslope windstorms. Adler et al. (2012) hypothesized that these warm air intrusions were associated with hydraulic jumps that are produced as the supercritical flow (along the lee slope) recovers to the ambient downstream subcritical conditions inside the crater. Meteor Crater Experiment-II (METCRAX-II), a follow-on collaborative research program with principal investigators from University of Utah, Arizona State University and National Centre for Atmospheric Research (NCAR), was designed to examine the causes of these warm air intrusions to aid the development and testing of relevant conceptual and numerical models pertaining to forced flow over mountains.

The spatial extent and the morphology of the crater provided a natural laboratory-like setting that could be used to investigate these downslope wind storm type flows (DWF) and their sensitivity to the changes in the ambient approach flow. Different instruments including three coherent Doppler lidars were set up inside and around the

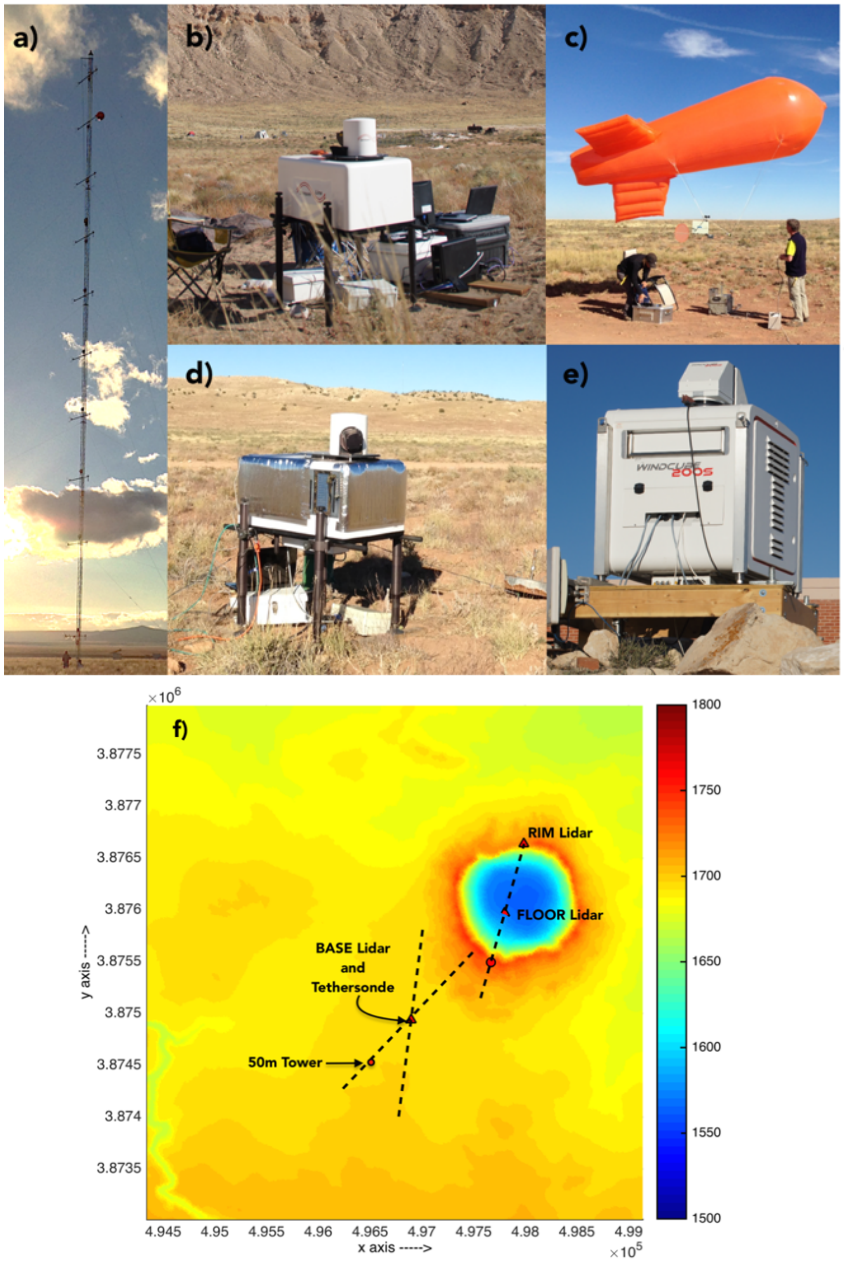

Figure 5 (a) 50m tower, (b) FLOOR lidar, (c) Tethersonde at BASE lidar site, (d) BASE lidar, (e) RIM lidar, (f) Terrain surrounding the crater along with instrument location. The dotted lines represent the RHI scan plane of the lidars.

crater to measure wind speed, wind direction, temperature, humidity, pressure and

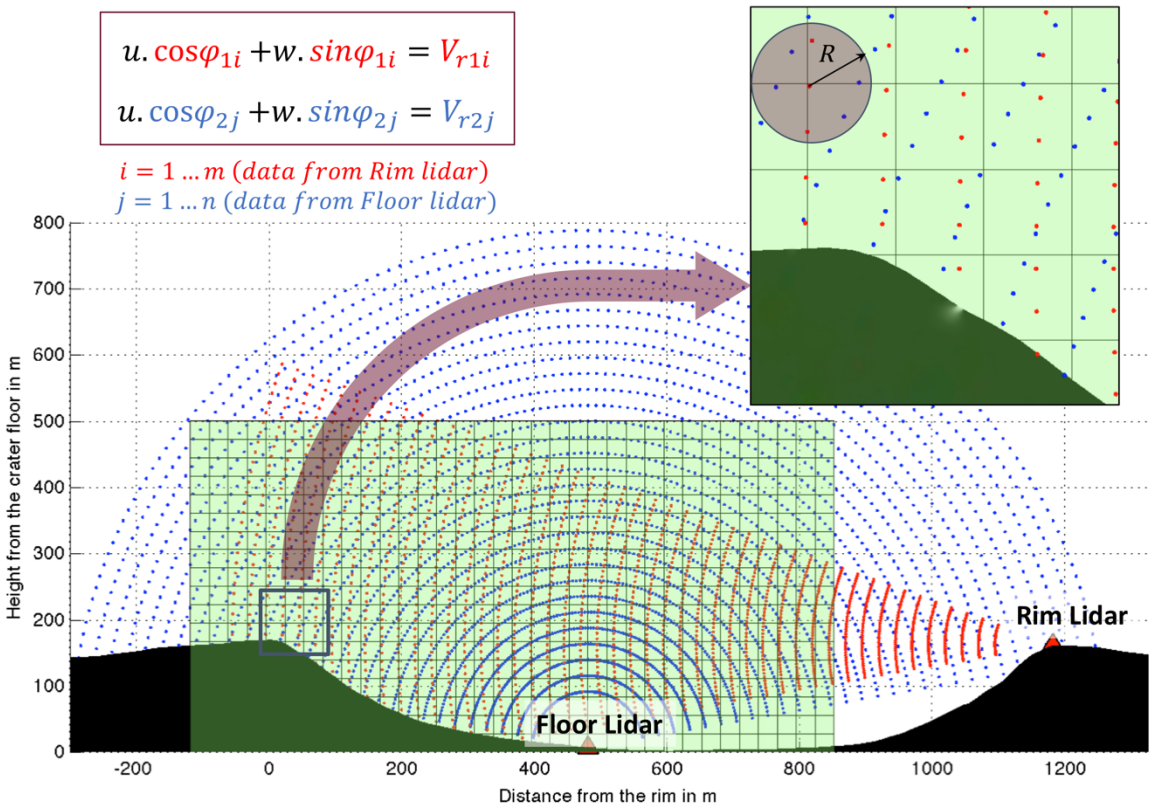

Figure 6. Location of the lidars and the scan sectors as viewed perpendicular to the scan plane. The vertical axis shows the height from the crater floor and horizontal axis shows the distance from the highest point on the rim in the scan plane.

surface fluxes. Among the lidars, two units (Halo-photonics' Streamline lidar and Leosphere's Windcube-200S lidar) were installed to perform dedicated coplanar RHI scans across the crater and another Halo-photonics' Streamline lidar was placed outside to monitor the approach flow.

2.2 METCRAX II Field Deployment

The field deployment lasted from 30th September, 2013 till 30th October, 2013, during which several instruments monitored the flow inside the crater and on the

surrounding plain. A detailed summary of the instrumentation can be found in Lehner et al. (2015). To supplement these continuous measurements, 7 nighttime intensive observational periods (IOPs) were conducted, during which, the instruments including tethersondes, were operated from late afternoon till little after sunrise. The IOPs were selected based on the forecast of quiescent nighttime condition which is essential for the formation of the katabatic drainage flow (Savage et al., 2008). In this study, IOP data from the three Doppler lidars, tethersonde soundings and a 50m tower were used. The RIM Lidar (Leosphere's Windcube 200S, Figure 5e) and the FLOOR Lidar (Halo Photonics' Streamline Doppler Lidar, Figure 5b) were installed to perform dedicated, synchronous RHI scans in Dual-Doppler mode, along the vertical plane passing through the South-Southwest gap in the crater rim. The radial velocity data from both the Lidars were combined to retrieve the 2D in-plane vector wind, giving insight into the spatial structure and evolution of the DWF events. The BASE Lidar (Halo Photonics' Streamline Doppler Lidar, Figure 5d) which was installed outside the crater to monitor the approach flow, performed periodic (every 15 minutes), 70° elevation - VAD scans along with repeated RHI scans at 15.5° azimuth and 42° azimuth. The radial velocity data from the RHI scans were combined to construct vertical velocity profiles of 5 m resolution, every 2 minutes. The specifications and settings of the Doppler lidars are given in Table (2.1).

Table 2.1

Lidar Specifications in METCRAX II

Lidar make	**Halo Photonics Streamline lidar**	**Leosphere's Windcube 200S**
Location	BASE, FLOOR	RIM
Wavelength	1.548 μm	1.543 μm
Pulse repetition frequency	15000 Hz	10000 Hz
Pulse width	150 ns	200 ns
Range gate size used	24 m	25 m
Pulses averaged	10000	10000
Pulse Energy	~0.1 mJ	~0.1 mJ
Radial velocity range	±19.4 m/s	±30 m/s

The temperature measurements used in this study were obtained from the 50 m tower (Figure 5a), and the tethersonde (Figure 5c) soundings at the BASE lidar site. The 50m tower (installed by NCAR's Earth Observing Laboratory), located to the southwest of the crater (Figure 5f), was equipped with CSAT3 sonic anemometers and hygrothermometers at 5m intervals. The tethersonde soundings provided measurements above 50m with an ascent time between 15-20 minutes.

2.3 Scanning Strategies and Wind Retrievals

2.3.1 Co-planar dual-Doppler lidar retrieval (RIM lidar and FLOOR lidar)

The main advantage of using two lidars in the field is that they will provide radial velocity measurements along two different directions from which the two velocity components (in this case, u and w) can be extracted using simple geometric relations.

a) Methodology. The retrieval used in the current study is based on Hill et al. (2010). The retrieval technique first involves constructing a 2D Cartesian grid in the scan overlap region. At each grid intersection point, circular regions with a radius of influence: $R = \Delta p / \sqrt{2}$ are defined. This specific value ensures the complete coverage or the retrieval. Any range gate center that falls within a radius of 'R'from a grid intersection point is associated with it (Figure 6). In addition, a weighting function is defined to take into account the length of range gate that falls within the circle of influence. After the radial velocities and their corresponding weights are assigned, an overdetermined linear system is formed using the geometric relationship between the vectors and their corresponding radial velocities (See Figure 6). This overdetermined system is solved using the weighted least squares approach (Eq. (2.1)).

$$\mathbf{U} = \left(\mathbf{A}^{\mathbf{T}}\mathbf{W}\mathbf{A}\right)^{-1}\mathbf{A}^{\mathbf{T}}\mathbf{W}\mathbf{R} \tag{2.1}$$

where, $\mathbf{A}_{(m+n),2} = \begin{pmatrix} \cos\varphi_{1j} & \sin\varphi_{1j} \\ \cos\varphi_{2k} & \sin\varphi_{2k} \end{pmatrix}, \mathbf{U}_{\mathbf{2,1}} = \begin{pmatrix} u \\ w \end{pmatrix}, \mathbf{R}_{(m+n),1} = \begin{pmatrix} rv_{1j} \\ rv_{2k} \end{pmatrix},$

$$\mathbf{W}_{(m+n),(m+n)} = \begin{pmatrix} \tilde{w}_j \delta_{jl} & 0_{m,n} \\ 0_{n,m} & \tilde{w}_k \delta_{kl} \end{pmatrix}$$

$\mathbf{W}$ is the weighting function matrix. The weighting function ($\tilde{w}_j$) should be taken based on the relative importance of the measurement, for instance, they could be based on the relative distance from the corresponding Cartesian grid intersection point. The subscript j runs from 1 to m and the subscript k runs from 1 to n, where

m and n are the number of hits from lidar-1 and lidar-2 respectively. Due to the comparitively small range gates possible with the lidars used in METCRAX II, the weighting function matrix was replaced with an identity matrix (Cherukuru et al., 2015). An alternate procedure is to take the mean of the radial velocities from each lidar within each cell and to solve the two-equation linear system. These two methods can be derived from one another under certain conditions detailed in appendix A.

To minimize the number of empty cells, the grid spacing is set equal to the range gate length. If the lidars have different range gate lengths, the larger range gate length is selected. The continuous scan mode software provided with the lidar determines the scan rate based on the total time taken for the scan, which is defined by the user. Hence, the scan rate was optimized using the total time taken for the scan from Eq. (2.2). The equation is derived in a way that the lidar beam intersects the cell at least once within a specified time frame.

$$T_i = \left(\frac{\left| \phi_i^{start} - \phi_i^{end} \right|}{d\varphi_i B_i} \right), i = 1,2 \tag{2.2}$$

where, T_i is the total time taken to complete the scan, ϕ_i^{start} and ϕ_i^{end} are elevation angles at the start and end of the scan respectively, and B_i is the frequency given by the ratio of PRF and averaging used. $d\varphi_i$ is the approximate angle subtended by the farthest cell.

$$d\varphi_i = \left(\frac{180 L_c}{\pi D_i} \right) \tag{2.3}$$

Where L_c is the grid spacing and D_i is the distance between the farthest cell and the lidar. The index 'i' corresponds to each of the lidars.

b) Coplanar Dual-Doppler Lidar Simulator. In order to determine the best possible scan strategy and the optimal instrument configuration for METCRAX-II, a coplanar lidar simulator was developed. The simulator works on a background windfield from an LES simulation of the downslope-windstorm type flow occurring at the crater. The LES simulations were performed to aide in the placement of different instruments for the actual field deployment.

- *Background wind field*. An idealized 2D numerical simulation of the flow was previously performed using the Cloud Model 1 (CM1) release 16. The simulation was run for a 15-minute period and wind velocity fields were obtained every second. Horizontal and vertical grid spacing was 2m. The initial temperature and wind profiles were selected to qualitatively reproduce the flow field and the warm-air intrusions that were observed in the west part of the Crater during METCRAX 2006.

- *Estimation of radial velocity.* The radial wind velocity was estimated using Eq. (2.4), which is the line integral of the weighted velocities along the beam (Frehlich et al. 1998). The weighting function (Eq. (2.5)) was obtained by convolving a range gate indicator function (which is a step function centered over the range gate location) with the laser pulse (which is a gaussian)

$$v_r^{R_{rg}}(t) = \int_{-\infty}^{\infty} \mathrm{W}_{\Delta p}(r') v_{r'}(r', t)\, dr' \tag{2.4}$$

$$\begin{aligned} \mathrm{W}_{\Delta p}^{R_{rg}}(r') &= \int_{-\infty}^{\infty} \left(\frac{2}{\Delta p \sqrt{\pi}\tau c} \right) \exp\left[\frac{-4\left[(r' - R_{rg}) - r''\right]^2}{\tau^2 c^2} \right] dr'' \\ &= \frac{1}{2\Delta p} \operatorname{erf}\left[\frac{2(r' - R_{rg}) + \Delta p}{\tau c} \right] - \operatorname{erf}\left[\frac{2(r' - R_{rg}) w - \Delta p}{\tau c} \right] \end{aligned} \tag{2.5}$$

where $v_{r'}$ denotes the radial velocity measured at a given instance of time at a distance r' . $v_r^{R_{rg}}$ is the radial velocity as measured by the lidar at a range

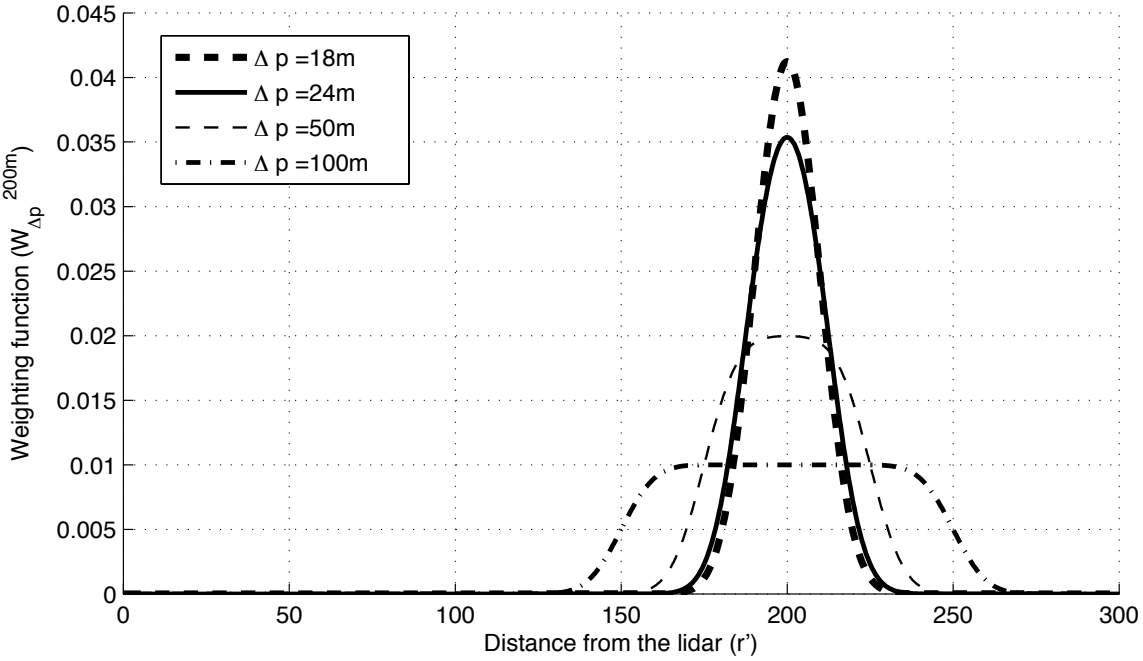

Figure 7. Figure showing the weighting function ($\mathrm{W}_{\Delta p}^{200}$) for a range gate at a distance of 200m, as a function of radial distance from the lidar (r′). Δp is the range gate length in m.

gate which is at a distance R_{rg} from the lidar and $W_{\Delta p}^{R_{rg}}$ is its corresponding weighting function measured along the beam. τ is the FWHM of the laser pulse and c is the speed of light. r' is the distance from the range gate center and Δp is the length of the range gate.

c) Error analysis. The major sources of error in dual-Doppler lidar retrievals stem from: (i) the assumption that the wind field is homogeneous within the grid cell- Spatial error, (ii) the assumption that wind field is stationary within the time taken to perform the scan- Temporal error, and (iii) the retrieval technique (matrix inversions)- Retrieval error. There are other sources of errors occurring due to the signal noise, atmospheric conditions, inhomogeneity of the aerosols in the illuminated volume etc., which would play a major role in reality but for the simple simulation work, they were not considered. These errors combine with one another and give rise to the net error in the measurement.

- *Spatial error.* In an ideal case, only the radial velocity values from the range gates which intersect the grid should be considered. Since, the retrieved velocity is obtained by combining radial velocity values from a region and not a single point, spatial error is defined as a measure of deviation from this spatial homogeneity assumption. the variance of the radial velocity would give a measure of the amount of variation within a cell for a given grid spacing. To obtain the net effect over the domain, the variance is normalized

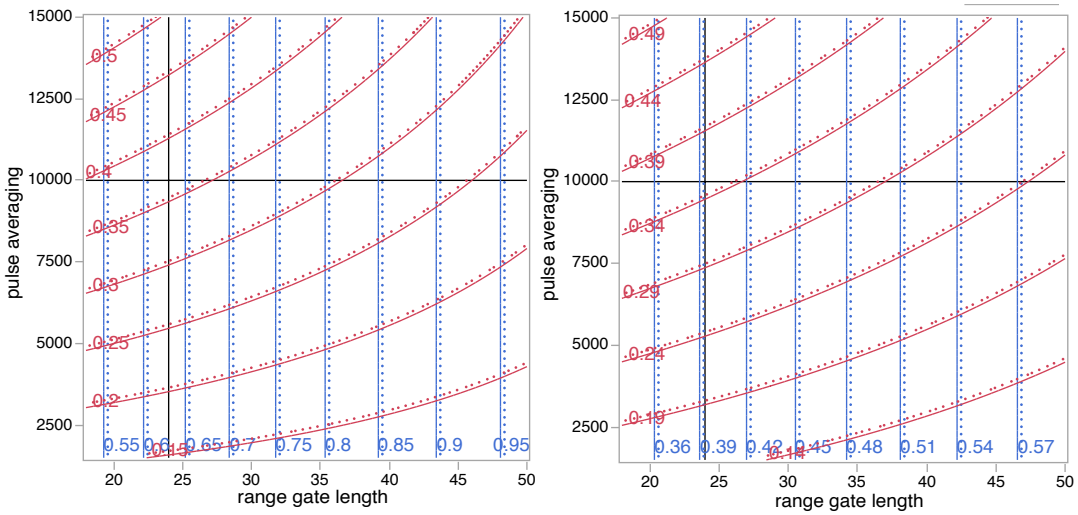

Figure 8. Spatial errors (blue lines) and temporal errors (red lines) for (a)u component and (b) w component, calculated from the coplanar dual Doppler simulator. The dots along the lines show the direction of the error gradient.

with the mean velocity and its RMS value is taken as a measure of the spatial component of error (Eq. 2.6)

$$E_{\Delta s}(t) = \sqrt{\frac{1}{MN}\sum_{i=1}^{M}\sum_{j=1}^{N}\left[\frac{\sigma_{\Delta s}^2(i,j,t)}{\tilde{v}(i,j)}\right]^2} \qquad (2.6)$$

$$\overline{E}_{\Delta s} = \frac{1}{K}\sum_{t=1}^{K} E_{\Delta s}(t)$$

where $\sigma_{\Delta s}^2(i,j,t)$ gives the variance in the cell (i,j) at time 't' and $\tilde{v}(i,j)$ gives the spatial average over the cell. 'M' and 'N' denote the total number of cells in the horizontal and vertical direction. This process is repeated at

each time step and that would give the total spatial error for a given grid spacing.

- *Temporal error.* The radial velocity measurements that are combined to obtain the vector wind are not simultaneous measurements i.e., the lidar scans are not instantaneous and take some finite time 'T'. Thus, the temporal error is the measure of the deviation from the 'frozen wind field' assumption during the finite acquisition time. The temporal error is taken to be the RMS value of the fluctuations about the mean. As mentioned previously, in order to combine the errors in space, the errors are normalized by the mean value (Eq. 2.7).

$$E_{\Delta t}(i,j) = \sqrt{\frac{1}{t}\sum_{t=1}^{K}\left[\frac{\sigma_{\Delta s}^2(i,j,t)}{\bar{v}(i,j)}\right]^2} \tag{2.7}$$

$$\overline{E}_{\Delta t} = \frac{1}{MN}\sum_{i=1}^{M}\sum_{j=1}^{N} E_{\Delta t}(i,j)$$

- *Retrieval error.* The method of least squares determines the approximate solution by minimizing the sum of squares of the residuals. Thus, it is an approximate solution of the overdetermined linear system and the retrieval error (quadratic difference between wind retrievals and background LES wind field) is the measure of deviation of the retrieved value from the mean in a given cell. Retrieval errors are strongly based on noise in the measurements and for this study they were not considered.

An ideal scanning technique would the wind field as closely as possible within the specified time window. Using this idealistic simulator, insights regarding these different sources of errors (Spatial and temporal errors) and their dependence on the individual lidar parameters were obtained.

2.3.2 Vertical Profiles from upwind RHI scans (BASE lidar).

Assuming horizontally homogeneous flow over the plain surrounding the crater, vertical profiles at 5m resolution could be retrieved from the RHI scans. Thus, the retrieval is representative of a horizontally averaged wind. This method is loosely based on Gal-Chen's turbulence parameter retrieval from lidar RHI scans (Gal-Chen et al. 1992).

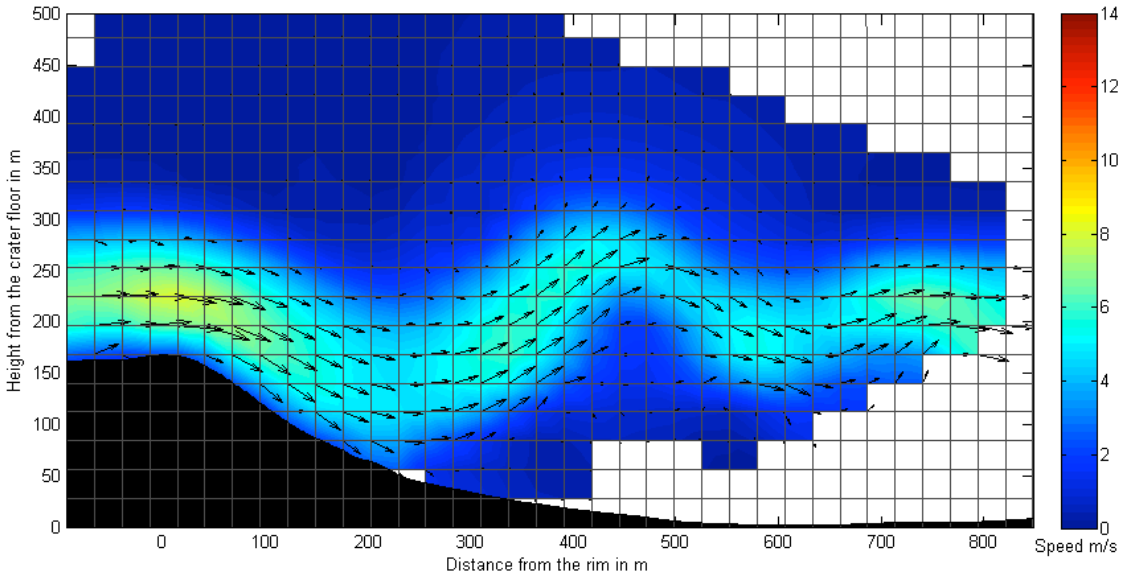

Figure 9. Coplanar Dual Doppler retrieval applied on the data from the lidar simulator. The background windfield is derived from an LES simulation.

First, the radial velocity values from the two RHI scans (at 15.5° *and* 42° azimuth) were segregated into vertical bins of the user specified resolution (5m in this case) and a time interval (~2 minutes). At each vertical bin, the horizontal velocity is retrieved in a least squares sense from an expression similar to Eq (2.1), except the indices, 'j' and 'k' refer to the data from the 15° and 42° RHI scan respectively. Further, to minimize the crater effect on the retrieval, only range gates upwind (i.e., pointing away from the crater) were considered in the retrieval.

2.3.3 Vertical Profiles from VAD scans (Base Lidar)

A VAD retrieval based on Boccippio (1995) was performed on the 70° elevation, full PPI scan at 15 minute intervals. At this elevation angle, vertical wind profiles with 23.18m resolution could be retrieved. To increase the statistical robustness of the retrieval, a singular value decomposition based, iterative regression scheme with outlier/influence point rejection based on Cook's distance was employed in place of a straightforward matrix inverse.

2.4 Results

2.4.1 Results from the Dual Doppler Lidar simulator

A lidar simulator was constructed on LES data to observe the dependence of spatial and temporal errors on the lidar parameters (e.g. range gate length and pulse averaging, scanning speed). A response surface analysis (Figure 8) revealed that spatial errors were independent of the pulse averaging used and were linearly dependent on the range gate length. As expected, it was seen that smaller range gates had a smaller spatial

error. However, both range gate size and pulse averaging influenced temporal errors. For a fixed range gate, increasing the averaging resulted in an increase in temporal errors due to the longer scan time required to ensure complete spatial coverage. On the other hand, for a fixed averaging value, increasing the range gate size resulted in a decrease in temporal errors due to the increase in grid resolution allowing faster scans according to Eq (2.2). Although the smallest errors were observed for lower values of pulse averaging and smaller range gates, a higher value of averaging and range gate had to be used based on the atmospheric and instrument limitations. A retrieval from the dual-doppler simulator, with lidar parameters that were used later in the field experiment is shown in Figure. 9.

2.4.2 Results from the field experiment

The upstream conditions were explained based on the data from IOP-4, during which the strongest warm air intrusions/ DWF events were observed inside the crater. The time-height display of horizontal wind derived from the RHI scans along with temperature contours obtained from the tethersonde (above 50m) and the 50m tower (5m-50m) is given in Figure. 10. Meteor crater is located in the painted desert which is a largely flat plain with very sparse vegetation. The plane surrounding the crater rises by ~1° to the Southwest (towards the Mogollon rim). Shortly after sunset, radiative cooling of the ground in turn causes the air atop to cool, forming a surface-based inversion which grew in depth as the night progressed. Simultaneously, cold air being denser, resulted in the formation of a mesoscale nocturnal drainage flow on the plain (Katabatically driven hydraulic flow, Savage et al., 2008). The absence of strong directional shear, and the

ambient flow having a South-Southwesterly direction could have caused the maximum speed of this nocturnal flow to exceeded 6m/s and reach heights of about 60m, which is higher than expected.

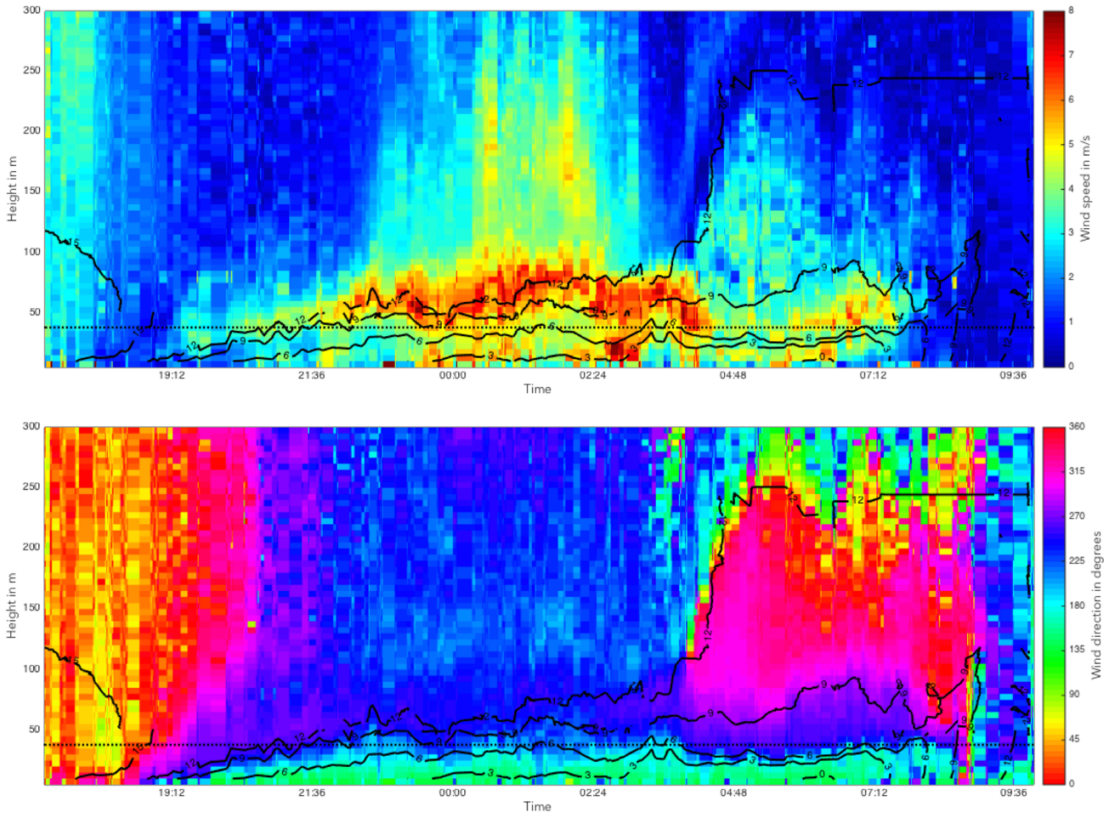

Figure 10. Time-Height plot of horizontal wind speed (above) and wind direction (below) derived from the RHI scans of BASE lidar for IOP-4 (19th-20th October, 2013). The temperature contours were obtained from the tethersonde (50m-300m) and the 50m tower (5m-50m). The dotted line represents the height of the crater rim on the SSW side.

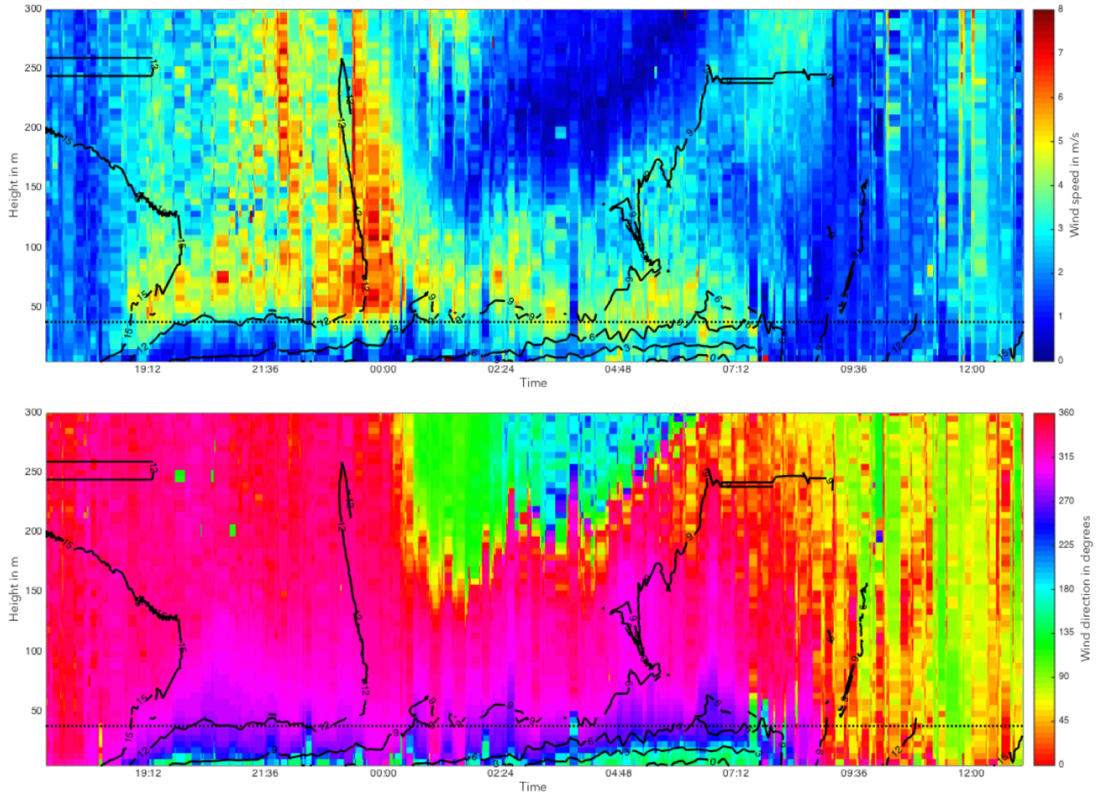

Figure 11. Same as figure 10 but for IOP-5 (21st-22nd October, 2013). The strong northerly drainage flow prevented the formation of a well defined drainage flow.

As the drainage flow height crossed the rim of the crater, strong lee waves associated with DWF events were observed inside the crater past 23:00. In contrast, during IOP-5, a strong ambient Northerly flow prevented the formation of the drainage flow (Figure 11) throughout the night and no DWF events were registered inside the crater. Thus, the presence of the katabatic drainage flow could be pointed as an essential factor for DWF events which is consistent with the previous hypothesis regarding the warm air intrusions from METCRAX I (Adler et al., 2011).

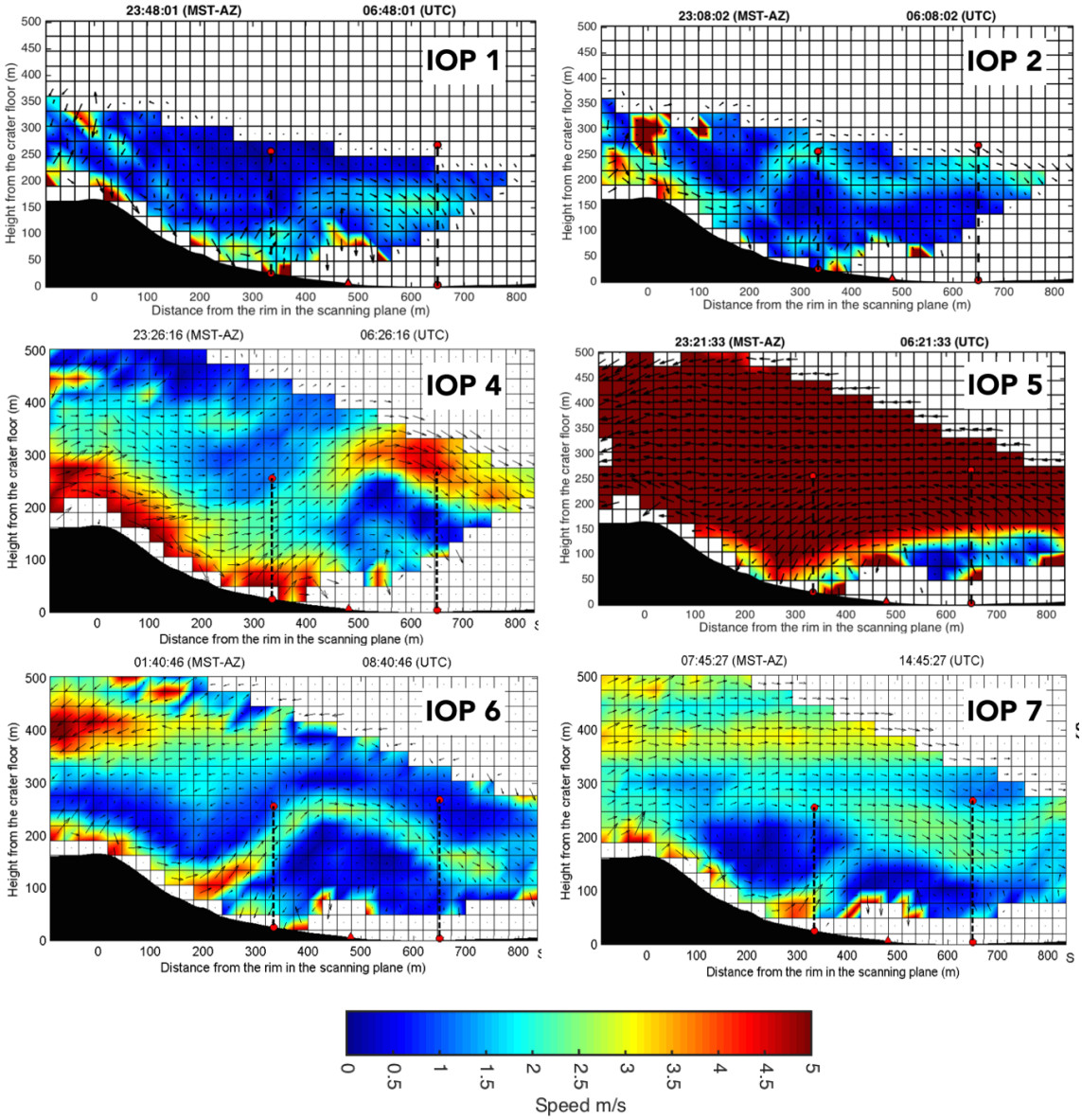

Figure 12. Coplanar Dual-Doppler lidar retrievals during showing DWF events inside the crater during different IOPs. IOP-3 was omitted due to poor data quality. DWFs were not observed during IOP-5 due to the strong Northerly ambient flow. The dotted vertical lines show the locations of the two tethersondes inside the crater (Data from these tethersondes are not not used in this study).

Figure 12 shows various DWF events as captured by the dual–Doppler lidar retrieval during different IOPs (Except IOP-3). Although only a single event for each IOP is shown in Figure 12, these events were intermittent and occasionally retreated up the slope. The dual-Doppler results from IOP-3 were omitted from the results due to the poor data quality. However, tethersonde soundings from inside the crater confirmed the presence of strong DWF events throughout the night (Similar to IOP-4). As shown, the strength and depth DWF events varied from very strong (IOP-4) to weak (IOP-1,2,6 and

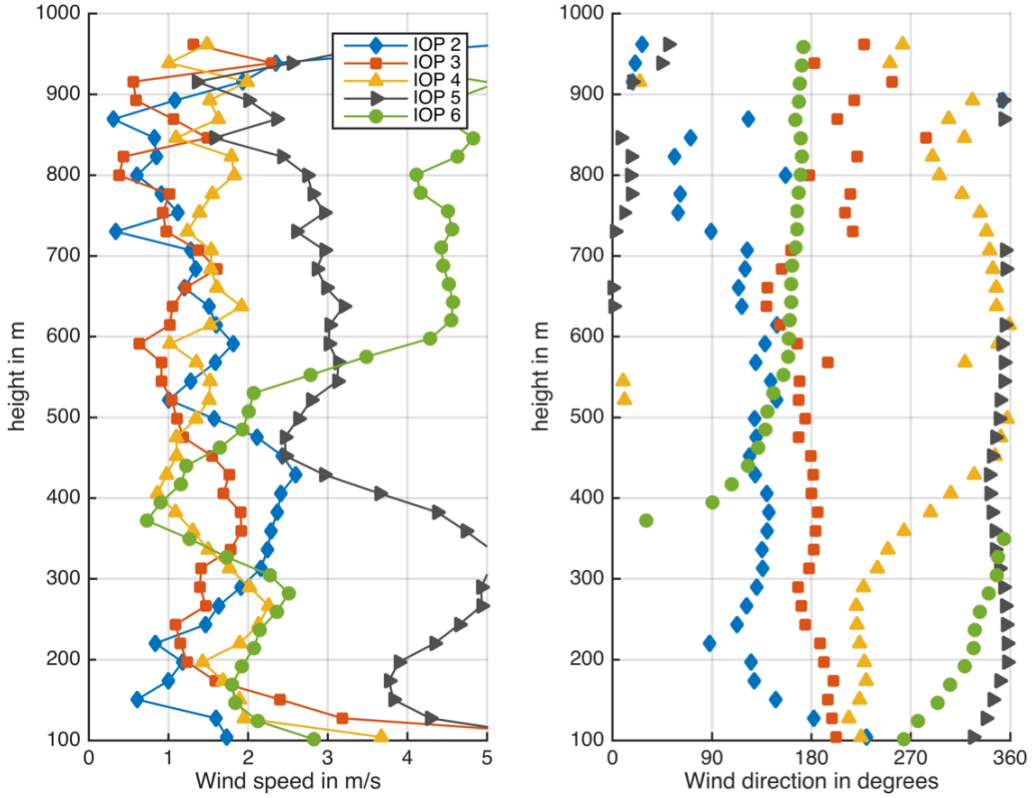

Figure 13. Vertical profiles of wind speed and wind direction from VAD scans of the BASE lidar during the DWF events presented in figure 12. BASE lidar was not functional until IOP-2 and was moved away from the site for IOP-7.

7). Most of the DWF events occurred shortly after the nose of the katabatic drainage flow reached the crater rim, except IOP-7 (Figure 12) when the DWF event was observed shortly after sunrise at 7:45am. The VAD profiles from the BASE lidar during each of these DWF events are shown in Figure 13 (The BASE Lidar wasn't operational until IOP-1 and was moved to the west rim for IOP-7). VAD profiles from the BASE lidar point to the strength and depth of the drainage flow as major factors in determining the occurrence of DWF type events in the crater.

2.5 Validation

Almost all the instruments in METCRAX II field experiment took complementary measurements and a proper error assessment of the retrievals using data from other instruments in the field was challenging. However, the Dual-Doppler retrieval, VAD retrieval and the vertical profiles from RHI scans were compared with measurements from the tethersonde at the southwest slope inside the crater, tethersonde at the base and the 50m tower located upslope on the surrounding plane respectively. A detailed description of all the instrumentation in METCRAX II (including the ones not used for the validation study) is given in Lehner et al. (2016). These inter-comparisons were used to assess the accuracy of the retrievals as well as to identify sources of discrepancies between the measurements. This will be valuable in designing future field deployments requiring similar scanning strategies.

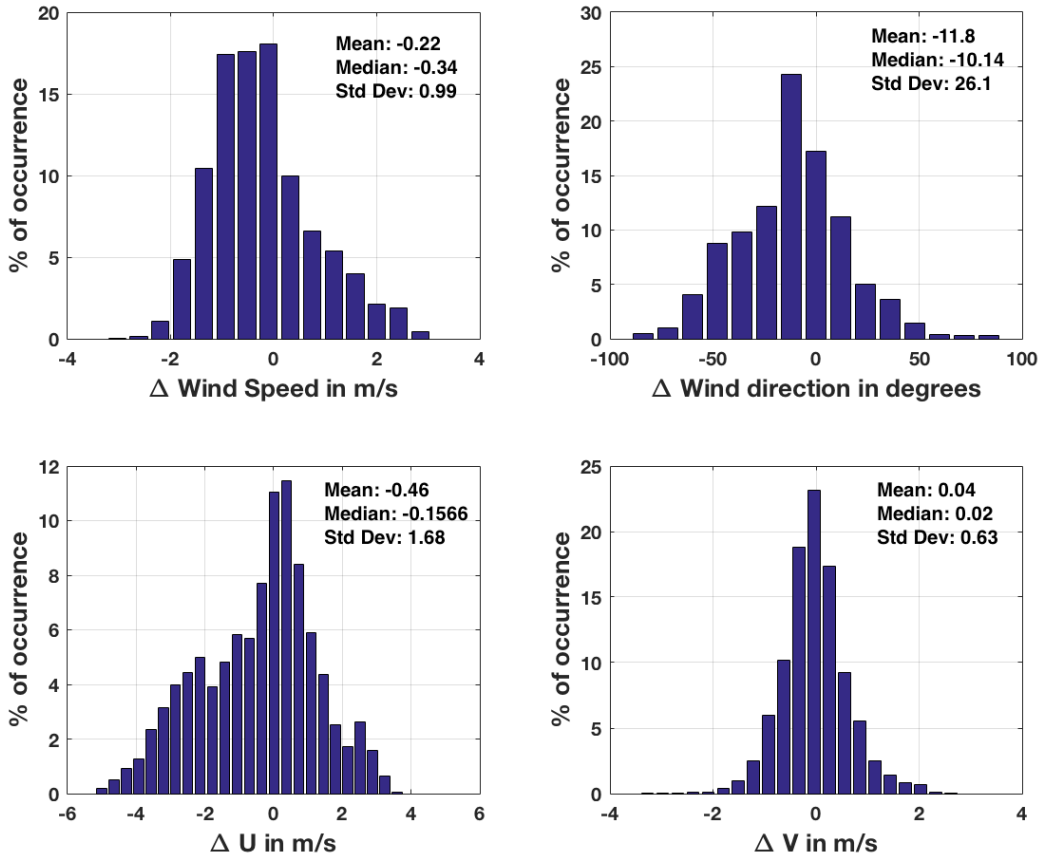

Figure 14. Clockwise from the top left, Histograms of Wind speed error, Wind direction error, Error in 'v' component and error in 'u' component of the vertical profiles obtained from RHI scans against the 50m tower.

2.5.1 Profiles from RHI scan.

A 50m tower was erected by NCAR's Earth Observing Laboratory on the surrounding plane at BASE site for continuous monitoring of the katabatic flow upstream to the crater. Among other instrumentation on the tower, three axis CSAT3 sonic anemometers installed at 5m intervals measured the three wind components. The 60 Hz wind measurements from the tower were quality controlled and 5 minute averaged

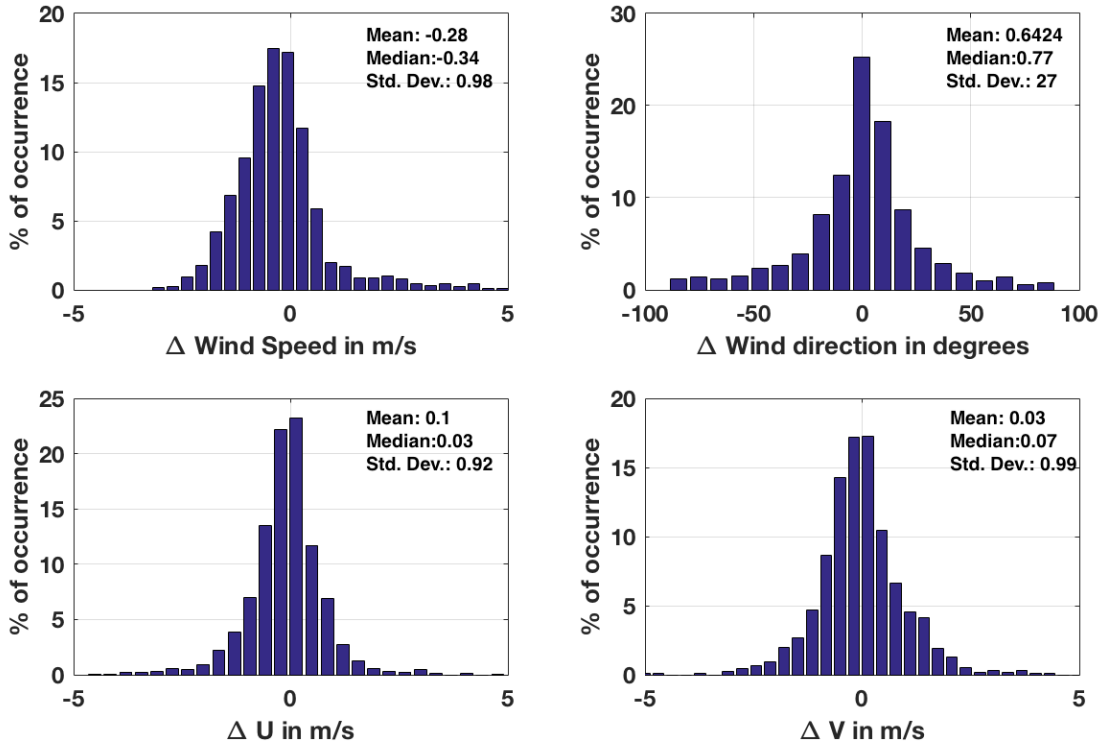

Figure 15. Clockwise from the top left, Histograms of Wind speed error, Wind direction error, Error in 'v' component and error in 'u' component of the vertical profiles obtained from VAD scans against the tethersonde measurements.

horizontal wind speed and wind direction values were used for comparing the retrieved wind components from the lidar RHI scans. The 'w' (vertical) component was extremely small compared to the other two components and were omitted in the inter-comparison study.

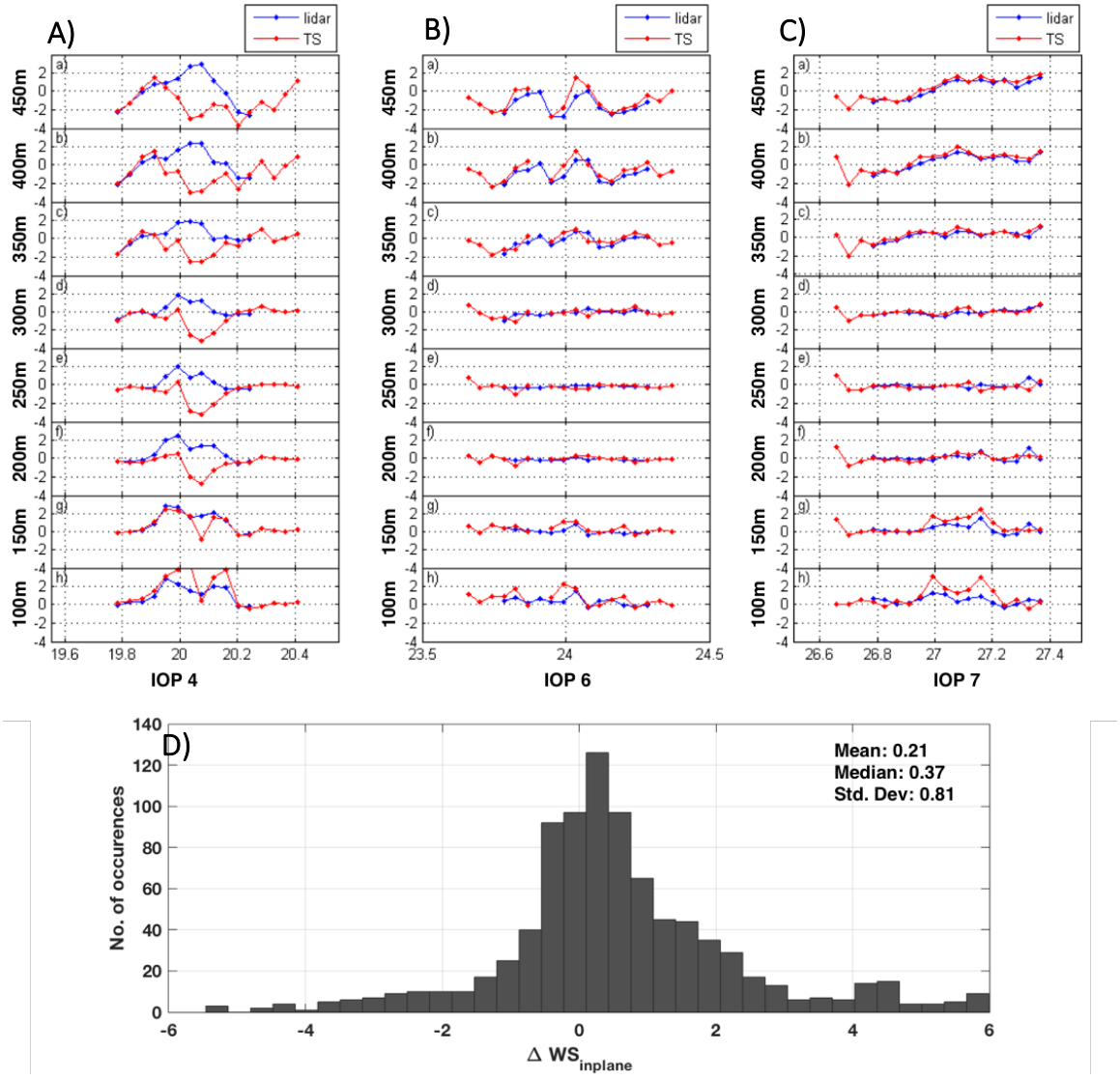

Figure 16. Top three figures show the in-plane component of the horizontal wind speed retrieved from Coplanar, dual-Doppler scans compared with the tethersonde soundings taken from the S-SW wall inside the crater. a) IOP-4, b) IOP-6 c) IOP-7. d) Histogram of the error between the retrieval and the tethersonde measurements.

2.5.2 VAD

The accuracy of the VAD profiles from the lidar at the BASE site was determined by comparing the measurements from a Karlsruhe Institute of Technology's (KIT) tethersonde system operated close to the lidar at the same site. The tethersonde system consisted of a $5m^3$ helium filled balloon fitted with a sonde measuring air pressure, horizontal wind speed, wind direction, temperature and dew point, tethered to a manually-operated electric winch. Continuous measurements upto a height of 250m were recorded by gradual ascents approximately every 15 minutes. The tethersonde data was quality controlled and the wind speed and direction values were used for inter-comparisons.

2.5.3 Coplanar dual Doppler lidar validation

The retrieved wind field from the coplanar dual-Doppler lidar scans, spanned the S-SW cross section of the crater. Horizontal wind speed and direction measurements from the tethersonde (Vaisala Digicora Tethersonde Systems) flown inside the crater from the S-SW wall, was used for comparisons. Although there was a 40m tower with sonic anemometers erected at the crater rim, positioned in line with the scan plane of the lidars, it fell beyond the maximum range of the lidar on the crater rim (~ 900m) due to poor aerosol content in the atmosphere during the IOPs. Since the tethersonde measured vertical profiles of horizontal wind components (u and v components) while the lidar captured vertical and in-plane components of the wind (i.e., u component along the scan plane and w component), only the horizontal in-plane component from both instruments were used for the inter-comparison study.

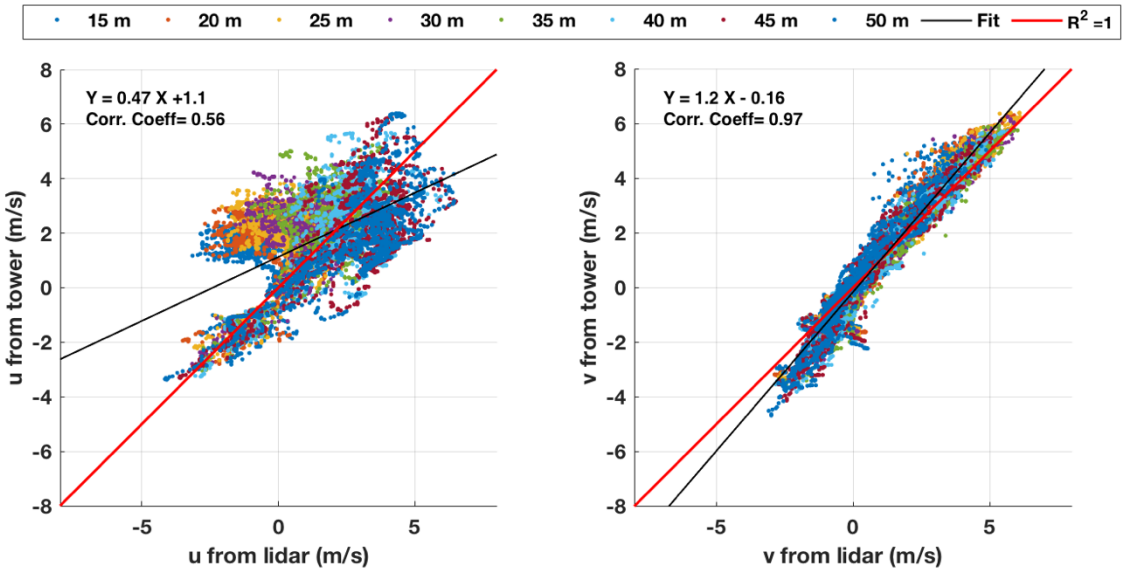

Figure 17. Scatter plot of retrieved 'u' component (left) and retrieved 'v' component from the RHI scans against the corresponding measurements from the 50m tower. The points are color-coded based on the height.

2.5.4 Discussion

While the mean error in wind speed is not too large in the vertical profiles of wind speed and direction retrieved from the RHI scans, there is a considerable scatter in the data. Looking into the errors in the retrieved 'u' and 'v' component (Figure 14), it is evident that the major source of error comes from the 'u' component. The scatter plot of retrieved 'u' and 'v' components (Figure 17) reveal a similar pattern, with the algorithm performing much better in retrieving the 'v' component than the 'u' component of the wind. The source of the large error in the 'u' can be determined by looking into the uncertainties of the lidar measurements and their propagation. The radial velocity measurements from any lidar are often polluted by noise due to the presence of small

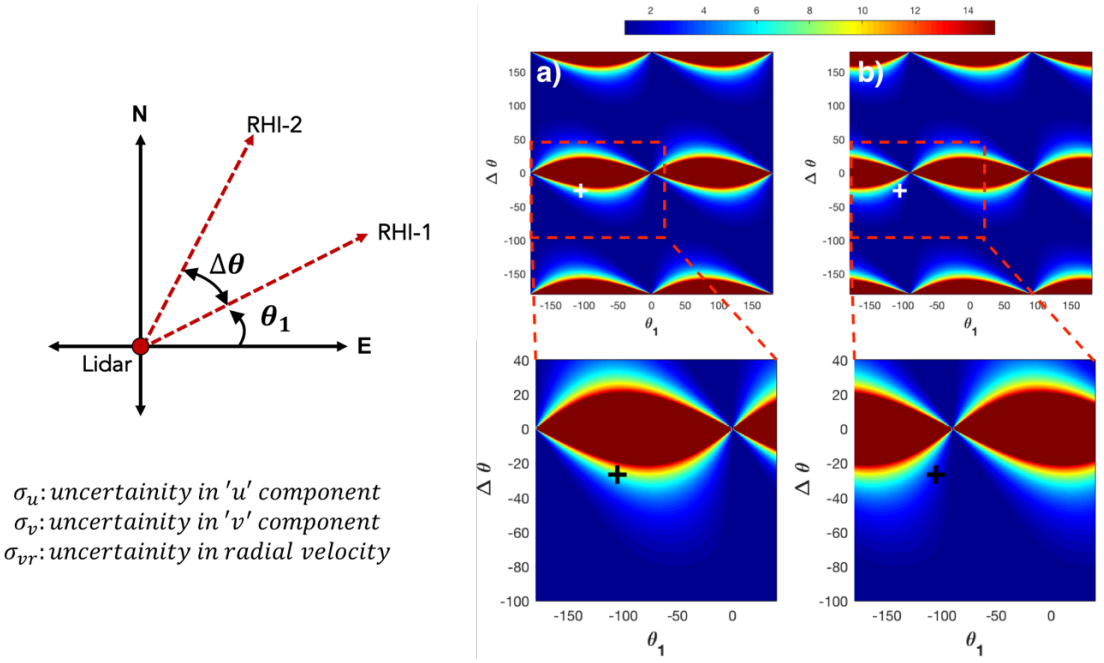

Figure 18. Pre-factor in Eq. (2.10) as a function of the azimuth angle of one RHI scan and the azimuthal separation between the scans for a) uncertainty in 'u' component, b) uncertainty in 'v' component. The '+' marks the setting used in METCRAX II. The two figures below show the same plot magnified around the region containing the settings for METCRAX II

scale turbulent fluctuations within range gate, imperfections in the lenses, digitization errors etc., to name a few (Frehlich et al., 1994). These errors/uncertainties in radial velocity measurements propagate to the retrieved wind field depending on the experimental setup.

Consider two RHI scans from the same lidar, separated by $\Delta\theta°$. Let θ_1 be the azimuthal angle for the first scan. The angles are measured from easting, i.e., 0° for a scan looking east (Figure 18). When the surrounding windfield is assumed to be

horizontally homogeneous, at a given height, the components u and v of the wind vector can be reconstructed from radial velocity measurements ($V_{r1}$and V_{r2}) from both the scans using Eq. (2.8).

$$u = \frac{[V_{r1}.\sin(\theta_1 + \Delta\theta) - V_{r2}.\sin(\theta_1)]}{\sin(\Delta\theta)}$$

$$v = \frac{[-V_{r1}.\cos(\theta_1 + \Delta\theta) + V_{r2}.\cos(\theta_1)]}{\sin(\Delta\theta)} \tag{2.8}$$

Using Gaussian error propagation, the uncertainties in radial velocity measurements (σ_{vr}) can be related to the uncertainty of u and v component (σ_u and $\sigma_v$respectively) using Eq. (2.9).

$$\sigma_u^2 = \left(\frac{\partial u}{\partial V_{r1}}\right)^2 \sigma_{V_{r1}}^2 + \left(\frac{\partial u}{\partial V_{r2}}\right)^2 \sigma_{V_{r2}}^2$$

$$\sigma_v^2 = \left(\frac{\partial v}{\partial V_{r1}}\right)^2 \sigma_{V_{r1}}^2 + \left(\frac{\partial v}{\partial V_{r2}}\right)^2 \sigma_{V_{r2}}^2 \tag{2.9}$$

Since, both the measurements are taken from the same lidar, $\sigma_{Vr1} = \sigma_{Vr2}$. Using Eq. (2.8) in Eq. (2.9), this simplifies to

$$\sigma_u^2 = \frac{[\sin^2(\theta_1 + \Delta\theta) + \sin^2(\theta_1)]}{\sin^2(\Delta\theta)}\sigma_{V_r}^2$$

$$\sigma_v^2 = \frac{[\cos^2(\theta_1 + \Delta\theta) + \cos^2(\theta_1)]}{\sin^2(\Delta\theta)}\sigma_{V_r}^2 \tag{2.10}$$

Figure 18 shows the pre-factor of σ_u^2 and σ_v^2 for various values of θ_1 and $\Delta\theta$. Based on the angles chosen for METCRAX II dataset (Marked by a black '+' in figure X), it is evident that the errors in 'u' will be significantly higher than errors in 'v' based on the geometry of the scans alone. While this explains the poor accuracy of the retrieval in determining the 'u' component, it does not explain the clustering in 'u' seen in the scatter plot of the error (Figure 17). This clustering did not have a strong correlation with stability (Figure 19) or dependence on height (Figure 17). However, considering the wind direction (Figure 20) it is evident that the scatter in 'u' in higher for Southerly and South-Westerly winds. This behavior can again be explained based on Eq. (2.10).

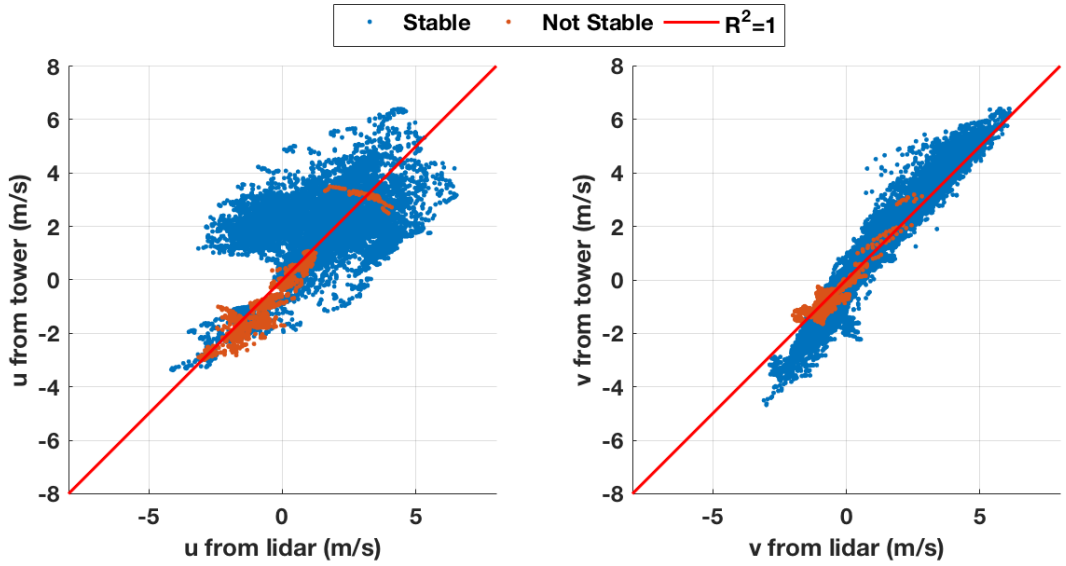

Figure 19. Same plot as in Figure 17 but color coded based on the atmospheric stability; dT/dZ >= Dry adiabatic lapse rate.

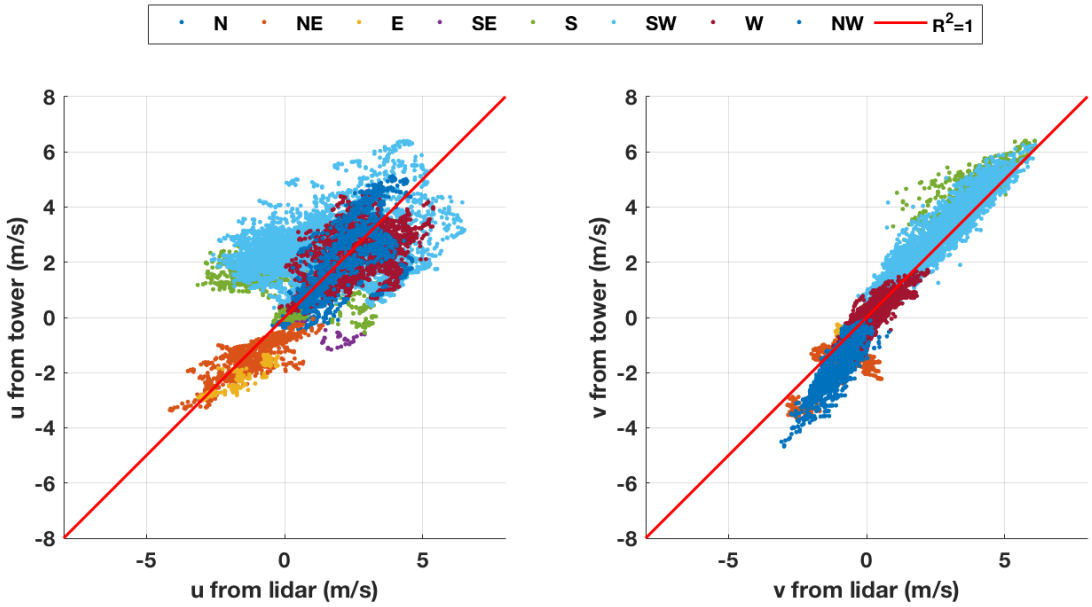

Figure 20. Same plot as in figure 17 but color coded based on the wind direction. It is evident from this plot that Southerly and South-Westerly flows have a much higher scatter.

For a given RHI scan configuration, the uncertainty in the retrieved wind components is directly proportional to the uncertainty in the measured radial velocity which in turn depends on the signal to noise ratio (SNR). Previous works with the halo photonics Streamline Doppler lidar have reported a velocity precision of 0.2 m/s for an SNR > -17 dB or 0.14 (Newsom, 2012). The SNR for the measurements taken during METCRAX II were well below the -17 dB level. Figure 21 shows the average value of measured SNR segregated by the wind direction. This plot shows that the SNR values of N, NE, SE'ly flows were comparatively higher, which could explain the large error in the 'u' component for flows from other directions. The overall low SNR observed for the measurements could be attributed to the poor aerosol content expected during

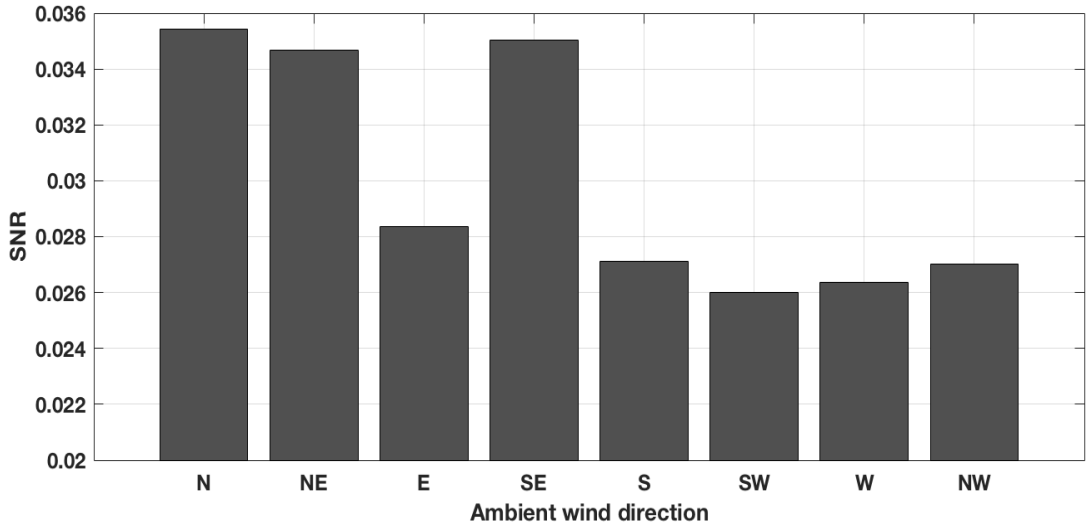

Figure 21. Plot of SNR (signal to noise ratio) of the lidar measurements for different mean wind directions

undisturbed, clear-sky nights, which was characteristic for all IOPs. One possible explanation for the change in SNR based on the wind direction could be the driving force/source for these winds. The mesoscale Southwesterly drainage/katabatic flows observed during the IOPs were much weaker and thus can be expected to have fewer aerosols than the strong Northerly, Northwesterly ambient flows.

The errors for the VAD retrieval compared with the tethersonde soundings at the BASE site are shown in Figure 15. Since, almost all the IOPs were conducted during stable night-time conditions, VAD is expected to perform reasonably well due to the validity of the linear wind field assumption, limited by the SNR of the measurements. Figure 16 shows the 15 minute averaged horizontal wind component measurements in the S-SW direction, taken from the dual-Doppler retrieval and the tethersonde for a few IOPs. The lidar retrieval is assumed to represent 1 minute averaged values whereas the

tethersonde measurements were instantaneous measurements taken during the ascent lasting ~ 15 minutes. This difference in the sampling time between the lidar retrieval and the tethersonde sounding could explain the overall spread in the errors seen in Figure 16. Further, strong warm air intrusions which at times reached the crater floor were observed during IOP-4 and the personnel operating the tethersonde reported large horizontal movements of the tethersonde during the ascents. This could have contributed to the large errors seen during IOP-4 (Figure 16a).

2.6 Summary

The second Meteor Crater Experiment (METCRAX II) was designed to study downslope-windstorm-type flows occurring at the Barringer Meteorite Crater in Arizona. Three Doppler lidars were employed along with other meteorological instruments to study the upstream flow and its response inside the crater during these intermittent events. Inside the crater basin, Doppler wind lidars were deployed to perform coplanar dual-Doppler lidar analysis to capture the two-dimensional (2-D) vertical structure of these flows. This type of analysis allowed the flow to be resolved on a 2-D Cartesian grid constructed in the range height indicator scan overlap region. In order to study the dependence of spatial and temporal errors on different lidar parameters, and to determine the scan strategy that minimizes the under sampling of radial velocities and provides a good spatial as well as temporal coverage of these short- lived events, a lidar simulator was developed using a large Eddy simulation wind field. An expression to calculate the scan speed (Eq. (2.2)) was determined to ensure complete spatial coverage while providing the best possible temporal coverage for a given coplanar scan. A retrieval

technique based on the weighted least squares technique with weights calculated based on the relative location of the lidar range gate centers to the grid intersection point was developed. The instrument configuration was determined by comparing the simulator retrievals to the background wind field and taking into account the limitations of commercially available lidars. To capture the upstream flow, vertical wind profiles were retrieved from VAD scans as well as by combining consecutive RHI scans at 15° and 42° azimuths from the BASE lidar radial velocity measurements. The high resolution-short range wind profiles from RHI scans complemented the long rage-low resolution wind profiles from VAD scans.

When applied to the lidar data from the field experiment, these retrievals proved to be very valuable in capturing the intermittent and short lived DWF events on the lee side of the crater and the upstream conditions in the surrounding plain. The analysis of the lidar data combined with tethersonde and tower data pointed to the depth and strength of the South-Southwesterly drainage flow to be of importance in determining the occurrence of DWF events inside the crater. Most of the instruments in the field experiment were setup to take complimentary measurements and a proper validation of the retrievals was challenging. One of the major limitations of the validation study was the different spatial and temporal sampling of various instruments. However, wherever the measurements of the tethersonde, sonic anemometers on the tower and the lidars overlapped, an intercomparison study was performed to assess the accuracy of the retrievals. Although all the retrievals performed reasonably well, comparatively large errors were observed in the u component of the vertical profiles retrieved from the RHI

scans. A Gaussian error propagation analysis revealed the cause to be the insufficient azimuthal separation between the RHI scans combined with the low SNR of the lidar measurements during the IOPs. In conclusion, lidars played a very important role in METCRAX II and this study highlights the capabilities of Doppler lidar vector retrievals in capturing complex atmospheric phenomenon.

CHAPTER 3

2D-VAR

"Complex flow" (in meteorological sense) is an atmospheric flow with strong spatial and temporal variability caused by a combination of complex terrain, presence of surface elements (e.g., forests, wind turbines, buildings etc.) and meteorological features (e.g., jets, weather fronts etc.) (Clifton, 2015). Most of the popular single Doppler lidar vector retrieval algorithms rely on the homogenous wind field assumption, which plays a vital role in reducing the indeterminacy of the inverse problem of obtaining Cartesian velocity from radial velocity measurements. Consequently, these methods fail in situations where the flow is heterogeneous. Alternate methods are based either on statistical models (e.g., optimal interpolation, Choukulkar et al., 2012) or computationally intensive four dimensional variational methods (Newsom & Banta, 2004). In this chapter, a 2D variational vector retrieval for Doppler lidar that uses the radial velocity advection equation as an additional constraint along with a tangential velocity constraint derived from a new formulation with gradients of radial velocity is described.

3.1 Relevant work

Figure 22 shows two successive Doppler lidar PPI scans acquired within a 60s time interval. We can see radial velocity structures advecting towards the lidar. The idea is to use this information in addition to the radial velocity equation to reduce the indeterminacy of the vector retrieval inverse problem. Previous attempts to retrieve motion/advection information from two consecutive datasets have come from disparate

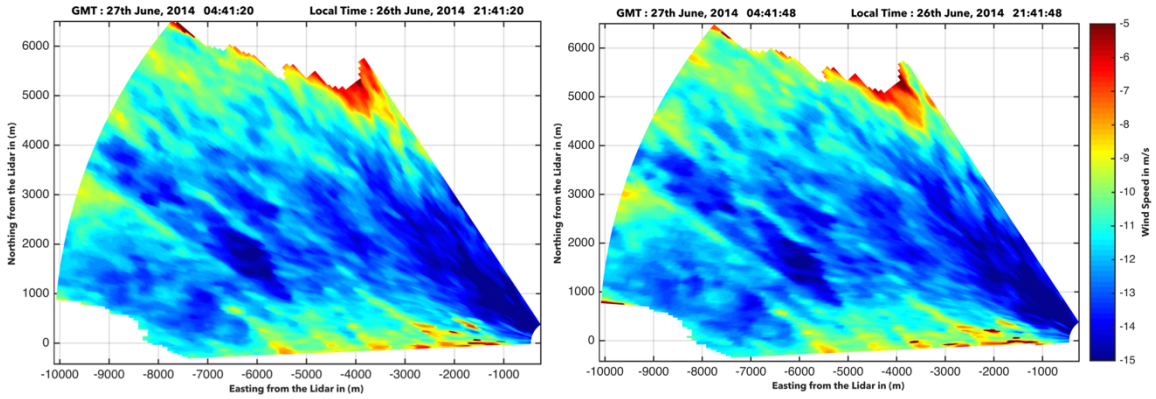

Figure 22. Advection of radial velocity structures seen in two successive radial velocity plots obtained from a Doppler wind lidar in a 60s interval.

disciplines. A review of relevant works that have explored the idea of obtaining the velocity vector using advection information is presented in this section.

3.1.1 Optical flow estimation in computer vision

Optical flow can be described as the velocity field associated with the movement of brightness/intensity patterns between two or more consecutive images. Optical flow is a well-studied problem in the field of computer vision and has many applications. A majority of the popular optical flow estimation methods in use today are derived either from the Horn & Schunck method (Horn & Schunck, 1981, HS81) or the Lucas-Kanade method (Lucas & Kanade, 1981, LK81). The HS81 formulation relies on the brightness constancy assumption between successive image frames to estimate the in-plane velocity vector $\mathbf{v} = (u, v)_{i,j}$, from the Lagrangian conservation equation. To alleviate the under-determined nature of the problem (i.e., there is only one advection equation with two unknowns u, v), an additional smoothness constraint on the velocity field is imposed and the velocity '**v**' is determined such that the cost function in Eq. (3.1) is minimized.

$$J(u,v) = \iint \left[\left(\frac{\partial \eta}{\partial t} + u\frac{\partial \eta}{\partial x} + v\frac{\partial \eta}{\partial y} \right)^2 + \alpha(|\nabla u|^2 + |\nabla v|^2) \right] dx\, dy \quad (3.1)$$

where, η is the brightness of each pixel, (x,y) is the location of the pixel in the image plane and α is the weight for the smoothing term, which controls the degree of smoothness in the flow field.

The LK81 differs from HK81 in the implementation of this method. While HS81 is a global method (i.e., the cost function is evaluated and minimized for the entire image), LK81 solves for **v** in a local sense, (i.e., the method is implemented in local regions, where every pixel within a region is assumed to have the same velocity **v** giving a sparse but more reliable vector field).

3.1.2 Correlation methods

These methods have been extensively used to retrieve winds from non Doppler systems (e.g., Conventional radar, elastic lidar etc.) (Schols & Eloranta, 1992; Mayor et al., 2012). Assuming Lagrangean advection of features in radar reflectivity, methods such as TREC (Tracking Radar Echoes by Correlation - Rinehart & Garvey, 1978; Tuttle & Foote, 1990) estimate the wind field by tracking the centroids of RADAR echoes using correlations between successive scans. The drawback of these methods is that the process is computationally expensive and the resulting flow field might contain large voids in areas lacking traceable flow features. Moreover, Gal-Chen (1982) has demonstrated that for certain advection-diffusion problems, the correlation method could produce multiple solutions.

Although not a pure correlation based method, Laroche & Zawadzki's (1994) variational echo tracking (VET) is based on a similar idea implemented using a variational method with continuity constraint to obtain the velocity field.

3.1.3 Doppler radar retrievals based on Gal-Chen's (1982) formulation

One of the early works by Gal-Chen (Gal-Chen, 1982, GC82) dealt with finding a reference frame moving with the flow, to reduce the errors caused due to the non-simultaneous measurements in a Doppler radar (i.e., 2D radar scans are not acquired in an instant but rather take finite time to complete one scan during which time the features could have advected). What started as a simple correction for advection was further developed into a least squares based vector retrieval by Gal-Chen & Zhang (Zhang & Gal-Chen, 1996 (GC-96); Gal-Chen & Zhang, 1993). Following GC82, an iterative method was implemented to obtain a moving reference frame based on the reflectivity conservation equation and later Eq. (3.2) was implemented in that moving reference plane to obtain the full velocity vector.

$$\mathrm{J(u,v,w)} = \iint \left[\left(\frac{\partial \eta}{\partial t} + u\frac{\partial \eta}{\partial x} + v\frac{\partial \eta}{\partial y} + w\frac{\partial \eta}{\partial z} \right)^2 + \alpha \left(u\frac{x - x_0}{r} + v\frac{y - y_0}{r} + w\frac{z - z_0}{r} - V_r \right)^2 \right] d\Omega\, dt \tag{3.2}$$

where, η is the radar reflectivity, (x_0, y_0, z_0) is the location of the radar, $d\Omega$ is the region over which the algorithm is applied, V_r is the radial velocity and α is a weighting term used to ensure that both the advection constraint and the radial velocity constraint are of the same order of magnitude. It must be noted that Eq. (3.2) is expressed in a fixed frame

of reference but the actual GC-96 retrieval is performed in a reference frame moving with the advection velocity.

3.1.4 Doppler radar variational methods

Variational retrieval methods (Sasaki 1970a, 1970b, 1970c) could be broadly classified into two types (Qiu et al., 2006): a) Parameter identification techniques (PI) and b) 4D-VAR based methods. In the former, data from the radar is used to estimate the unknowns (e.g., Cartesian velocity) by fitting them to a set of control equations pertaining to reflectivity/ radial velocity conservation equation (Qiu & Xu, 1992). The resulting retrieval could be considered as a time-mean estimate over the acquisition time period. The latter method (i.e., 4D-VAR based) relies on a forecast model to obtain the wind field along with thermodynamic variables (Sun et al., 1991). 4D-VAR methods have been known to be computationally expensive to implement and often limited by the underlying assumptions in the forecast model.

The PI techniques involve finding the best time-mean estimate of the control variables ($\mathbf{X}$ = [u,v,w…]) by minimizing a cost function (J($\mathbf{X}$)) of the form:

$$\mathrm{J}(\mathbf{X}) = \frac{1}{2\Omega}\int \left(\sum \mathrm{W}_i \mathrm{C}_i^2\right)\ d\Omega \tag{3.3}$$

where, W_i are the weights pertaining to the relative importance of the constraints C_i, corresponding to the various control equations in a weak sense and $d\Omega$ is the domain over which the minimization is performed. Although, the control equations could be specified as strong constraints (Lewis & Derber, 1985) or weak constraints (Sasaki

1970b,1970c), previous works (Laroche & Zawadzki, 1994; Xu et al., 1994) have shown that the weak constraint formulations perform better in the presence of model errors, especially with the reflectivity/radial velocity conservation equation.

Previous PI works mainly differed in the type of constraints and method used for the minimization of the cost function. Qiu & Xu (1992) first proposed a "simple adjoint method (SA)", to retrieve the time mean winds of artificial data, using only the Lagrangian conservation of radar reflectivity as a strong constraint in the cost function. The SA method was later upgraded to include the eddy diffusion & residual forcing terms in the reflectivity conservation equation in Xu et al. (1994), continuity equation as a strong constraint in Xu & Qiu (1994) and radial velocity equation with algorithmic improvements in Xu & Qiu (1995). Following the SA method, Qiu & Xu (1996) developed a computationally efficient least-squares formulation with weak zero horizontal divergence and vorticity constraint. A single Doppler radar wind retrieval intercomparison study by Shapiro et al. (1995) showed that the least squares formulation performed better the other retrieval methods for the given test case. When compared with the SA method, the least squares formulation was found to robust and yielded similar retrievals for short scan periods. In addition, Gao et al. (2006) added a background constraint to reduce the noise arising from the finite difference calculations of the gradients and to facilitate a smooth transition to fill the data void regions with wind field from the background. In an attempt to preserve local structure, Qiu et al. (2006) developed a two step variational method in which a proxy background was obtained from

a second order expansion of Legendre polynomials. Some of the above methods have been extended for dual Doppler radar by Gao et al. (1999).

3.1.5 Related work with Doppler Lidars

Methods based on 4DVAR of Sun et al. (1991), has been tested on Doppler lidar (Chai et al., 2004, Newsom & Banta (2004a, 2004b), Newsom et al. 2005, Xia et al. 2008). A two-step variational retrieval method based on Qui et al. (2006) was implemented for the Hong Kong International airport lidar dataset to detect flow hazards for airplanes (Chan & Shao, 2007) and was later used in Lagrangean coherent structure analysis by Tang et al. (2011). The same method was implemented for a plume dispersion and air quality study by Chan & Yu (2010).

The general technique used in the current study is based on the 3D-VAR method described by Gao et al. (2006). However, for scans with low elevation angles, further simplifications could be made to the radial velocity equation and an expression for the tangential velocity can be derived. Based on these modifications, a new fast 2D-VAR algorithm was developed for low elevation, repeated PPI scans.

3.2 Formulation

3.2.1 Constraint equations

Consider figure 1 from (Chapter1). At every point on the scan surface, the Cartesian velocity components and their counterparts in spherical coordinates are related by:

$$V_r = u.cos\theta cos\varphi + v.sin\theta cos\varphi + w.sin\varphi \qquad (3.4a)$$

$$V_{th} = -u.sin\theta + v.cos\theta \tag{3.4b}$$

$$V_{tv} = -u.cos\theta sin\varphi - v.sin\theta sin\varphi + w.cos\varphi \tag{3.4c}$$

where, V_r is the radial velocity, V_{th} is the tangential velocity in the horizontal plane, V_{tv} is the tangential velocity in the vertical, (θ, φ) are the azimuth and elevation angles respectively. As mentioned previously, a Doppler lidar can measure only V_r.

Let us consider a repeated PPI scan at low elevation angles and attempt to retrieve the horizontal components of the velocity vector. At low elevation angles ($\varphi \approx 0$), Eq. (3.4a) reduces to

$$V_r = u.cos\theta + v.sin\theta \tag{3.5}$$

Differentiating Eq. (3.5) along the azimuth direction and using Eq. (3.4b) we get

$$\frac{\partial \tilde{V}_r}{\partial \theta} = (-u.sin\theta + v.cos\theta) + \frac{\partial u}{\partial \theta}\, cos\theta + \frac{\partial v}{\partial \theta} sin\theta \tag{3.6}$$

$$= V_{th} + \mathrm{P} \quad , where \ \mathrm{P} = \left(\frac{\partial u}{\partial \theta}\, cos\theta + \frac{\partial v}{\partial \theta} sin\theta\right) \tag{3.7}$$

The term 'P' is identically zero when the simplified constant wind assumption is true (e.g. VAD, VVP). 'P' could be understood as a measure of deviation from this assumption.

We now have two equations (Eq. (3.5) and Eq. (3.7)) and three unknown variables (u,v and P). These equations can be closed by considering the radial velocity advection equation. Assuming that radial velocity patterns advect with the flow, we get

$$\frac{\partial \widetilde{V_r}}{\partial t} + u \frac{\partial \widetilde{V_r}}{\partial x} + v \frac{\partial \widetilde{V_r}}{\partial y} = 0 \tag{3.8}$$

where, $\widetilde{V_r}$ is the filtered radial velocity (e.g., Gaussian filter) introduced to reduce the effect of noise on numerical derivatives. By substituting the partial derivatives with finite differences, and solving Eq. (3.5), (3.7) and (3.8), the horizontal vector field can be determined. Since gradients are prone to become unreliable in regions with high noise levels, a background constraint similar to Gao et al. (2006) is included. The background constraint equation is formulated as the departure of the vector field (u,v) from the vector field derived using VVP or sector VAD (u_b, v_b). The vector field (u,v) can be estimated by minimizing a cost function derived from the above mentioned constraints.

3.2.2 Implementation

The radial velocities from successive scans are first interpolated onto a Cartesian retrieval grid. Based on the above considerations, the cost function is formulated as

$$\mathrm{J(u,v,P)} = \frac{1}{2\Omega}\int (W_a \mathrm{A}^2 + W_b \mathrm{B}^2 + W_c \mathrm{C}^2 + W_d \mathrm{D}_a^2 + W_d \mathrm{D}_b^2 +)\, d\Omega \tag{3.9}$$

$$where, \quad A = \left(\frac{ux}{r} + \frac{vy}{r}\right) - V_r^{obs}, \quad B = \left(-\frac{uy}{r} + \frac{vx}{r}\right) - \frac{\partial V_r^{obs}}{\partial \theta} + \mathrm{P},$$

$$\mathrm{C} = \frac{\partial \widetilde{V_r}}{\partial t} + u \frac{\partial \widetilde{V_r}}{\partial x} + v \frac{\partial \widetilde{V_r}}{\partial y}, \qquad \mathrm{D}_a = u - u_b, \qquad \mathrm{D}_b = v - v_b,$$

$$x = r.cos\theta, \qquad y = r.sin\theta, \qquad r = \sqrt{x^2 + y^2}$$

Here, A is the radial velocity constraint, B is the tangential velocity constraint, C is the radial velocity advection constraint and D is the background constraint. The

objective is to find u, v and P at which the cost function is minimized or the gradients (Eq. (3.10), (3.11) and (3.12)) vanish.

$$\left(\frac{\partial \mathrm{J}}{\partial \mathrm{u}}\right)_{ij} = W_a \mathrm{A}\frac{x}{r} - W_b \mathrm{B}\frac{y}{r} + W_c \frac{\partial \widetilde{V_r}}{\partial x} + W_d \mathrm{D}_a \tag{3.10}$$

$$\left(\frac{\partial \mathrm{J}}{\partial \mathrm{v}}\right)_{ij} = W_a \mathrm{A}\frac{y}{r} + W_b \mathrm{B}\frac{x}{r} + W_c \frac{\partial \widetilde{V_r}}{\partial y} + W_d \mathrm{D}_b \tag{3.11}$$

$$\left(\frac{\partial \mathrm{J}}{\partial \mathrm{P}}\right)_{ij} = W_a . B . P \tag{3.12}$$

The minimization can be performed using any non-linear optimization methods. In the current study, the minimization was performed using the quasi-Newton method (Appendix B).

3.2.3 Selection of Weights

The weights in the cost function address two issues. First, when the individual constraints in the cost function scale differently, constraints with lower order of magnitude (e.g., constraints with spatial derivatives) naturally contribute less to the cost function and thus are less affected by the minimization process. Hence, the weights need to ensure that each constraint has the same order of magnitude. Second, within the retrieval domain, depending on the confidence of the measurement, some of the constraints might be required to have a higher importance than others. For instance, consider the radial velocity advection cost function. For grid points near the boundary of the domain, there is a high probability for the flow structures to advect out of the retrieval domain during the acquisition time for the scans. For such regions, giving equal

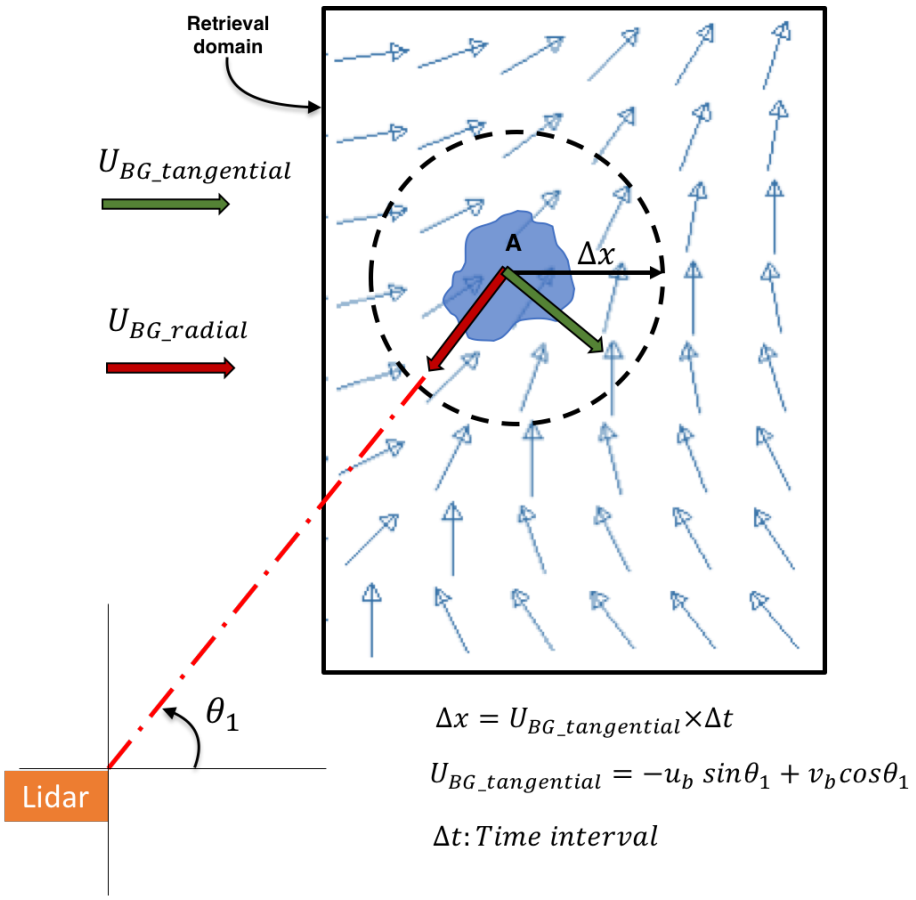

Figure 23. Figure showing the advection of a flow structure and the formulation of the weights for the advection equation.

importance to the advection constraint similar to the other constraints might not be useful, if not detrimental to the retrieval. Hence, the weights are calculated to address these two concerns.

The tangential velocity constraint and the background constraint complement each other. The inclusion of 'P' in the tangential velocity formulation (Eq. (3.9)) allows the retrieval to preserve the local non homogeneity in the flow. However, this equation is very sensitive to noise, since it is comprised of derivatives of radial velocity

measurements. In order to limit the use of this constraint to regions where the homogeneity assumption breaks down, W_b and W_d were chosen based on the R^2 value (coefficient of determination) of the linear wind model used in the construction of the background wind field (usually VVP or sector VAD). The value of R^2 is between 0 and 1; 1 when the variability in the radial velocity measurements is entirely accounted for, by the linear wind model and is lower when it deviates from it. Thus, while calculating the background wind, at each grid point in the retrieval domain, the weight for the background is calculated as

$$W_d(x,y) = 1 - \frac{\sum(Vr_{model}(\theta) - Vr_{observed})^2}{\sigma_{Vr}^2}\Bigg|_{(x,y)} \tag{3.13}$$

$$Vr_{model}(\theta) = u_b.cos\theta + v_b.sin\theta \tag{3.14}$$

where, σ_{Vr}^2 is the variance of the radial velocities within the retrieval region (i.e., in the region of influence of the grid point) and $\sum(Vr_{model} - Vr_{observed})^2$ is the residual. W_b is taken as $W_d - 1$. The weight for the radial velocity (W_a) constraint is taken to be 1.

Consider some flow feature (Figure 23, 'A'), advecting with the surrounding mean flow, that is captured in a lidar scan at a certain instant, as shown in figure 23. In the subsequent scan, this feature could advect to a different location. For every grid point, a circular region with a radius Δx could be defined, within which, the new location of the feature would fall in the subsequent scan. Now, the radial velocity advection constraint is built on the assumption that radial velocity of this feature remains constant from one scan to another. Ideally, this is only valid when the flow direction is along the

beam (i.e., lidar's line of sight) or in a trivial case, when the flow field is stationary. Moreover, the differential equation used to describe the advection only works for small displacements (ideally, 1-2 grid spacing). The weight (W_c) must be formulated such that it takes the aforementioned factors into consideration and identify regions in the retrieval domain where this constraint would be meaningful.

For this, let Δx be defined as:

$$\Delta x = U_{vvpT} \times \Delta t \tag{3.15}$$

where, Δt is the time interval between the two scans for each grid point and U_{vvpT} is the tangential velocity at the grid point obtained from the background wind field (usually VVP or sector VAD) and can be obtained using:

$$U_{vvpT} = -u_b \, sin\theta_1 + v_b cos\theta_1 \tag{3.16}$$

where, $(u_b \, , v_b)$ are the background wind vectors and θ_1 is the azimuth angle for the grid point from the lidar. W_c can now be formulated as an image mask based on some threshold λ as

$$W_c = \begin{cases} 1; & when \;\; \Delta x \leq \lambda \\ 0; & when \;\; \Delta x > \lambda \end{cases} \tag{3.17}$$

where, λ could be defined as: $\lambda = 2(grid \; spacing)$, to satisfy the small displacement condition. Alternatively, the threshold could also be based on the integral length scale of the flow if known a priory.

Defining W_c in this manner satisfies the requirements as follows:

- For a given mean flow, Δx is large when the time difference between the scans is large. This ensures that the small displacement condition is satisfied.
- For a given Δt, Δx is large when the tangential velocity (U_{vvpT}) is large. This ensures that the constant radial velocity during advection condition is satisfied.

3.3 Test cases

3.3.1 Data from Tehachapi, California

a) Description of the data set. This test data was acquired between 25-27th June, 2014, at Tehachapi, California. A Lockheed Martin Coherent Technologies WindTracer® lidar (Table 3.1), was installed on a hill (1450m ASL) at a windfarm (Windland, Inc.) (35.094089° N, 118.341312° W). The lidar performed a 60° sector, repeated 0° elevation, PPI scans looking North-West over Tehachapi city.

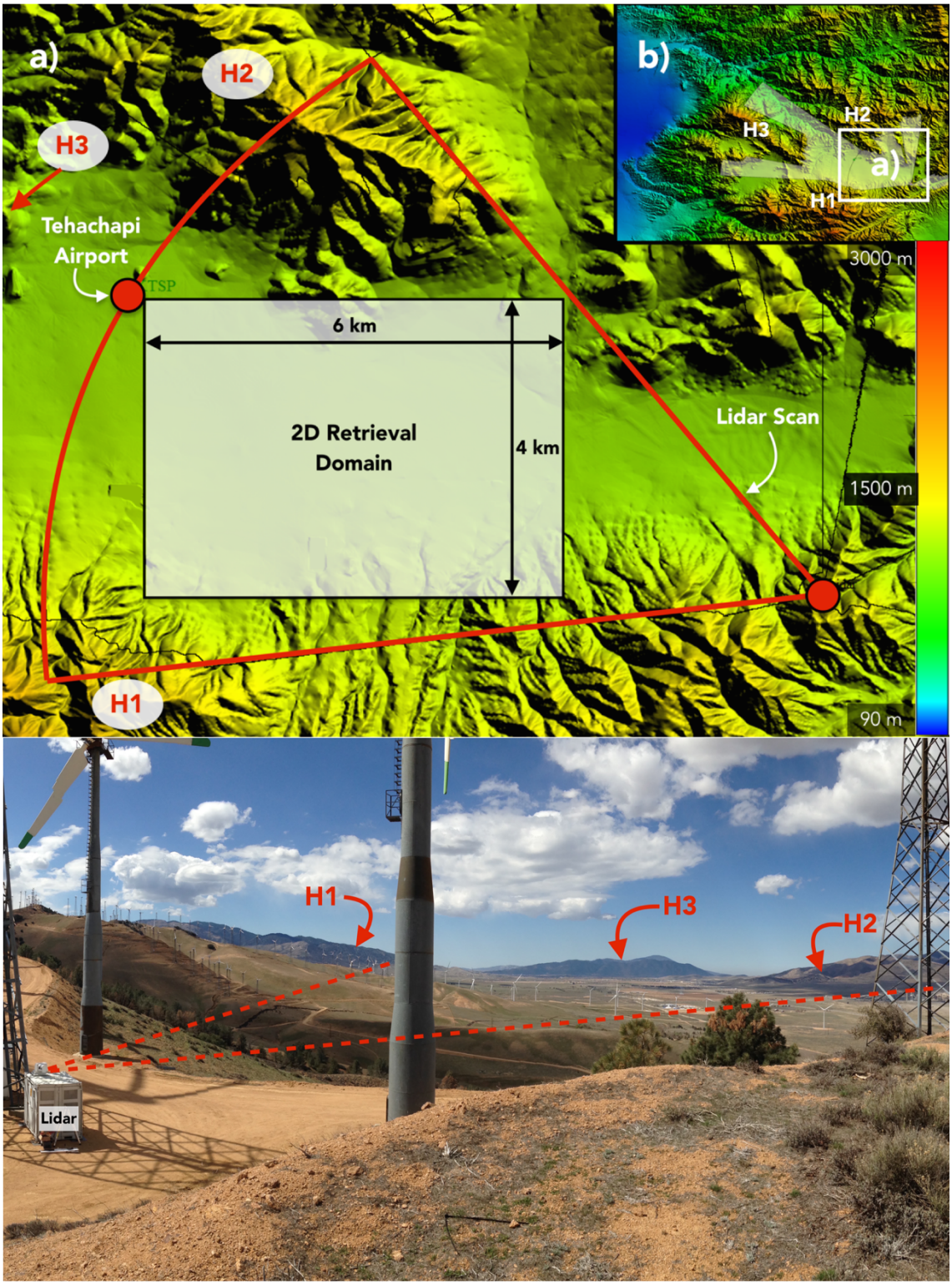
a)
H2
H3
Tehachapi
Airport
TSP
6 km
2D Retrieval
Domain
4 km
Lidar Scan
H1
b)
H3
H2
a)
H1
3000 m
1500 m
90 m
H1
H3
H2
Lidar

Figure 24. A relief map and a photograph of the terrain showing the location of the lidar and the retrieval domain. H1, H2 and H3 and hills visible in the lidars field of view. Based on the relief map, this terrain could be classified as a complex terrain.

Table 3.1:
Specifications of the Lidar used in the study

Lidar type	LMCT WindTracer®
Wavelength	1.617 μm
Pulse repetition frequency	750 Hz
Pulse width	300 ns
Range gate size	100 m
Pulses averaged	100
Pulse Energy	2 mJ
Radial velocity range	±38 m/s

The 2D retrieval was performed on a rectangular domain (6 km × 4 km) on the lidar scan as shown in figure 24. Due to the location of the lidar on the top of a hill, the scan and the retrieval domain were located approximately 200m above the Tehachapi valley. The weights for individual terms in the cost function for this dataset were set at W_a= 1, W_b= 0.5 , W_c= 10^5 and W_a= 0.1 for this preliminary validation. The lidar data was initially quality controlled based on a simple SNR based filter, i.e., points with very high SNR (indicative of hard target returns) and very low SNR (dominated by noise) are rejected. In addition, 2-3 range gates immediately before a hard target return along a line of sight were also removed (Banta et al., 2015).

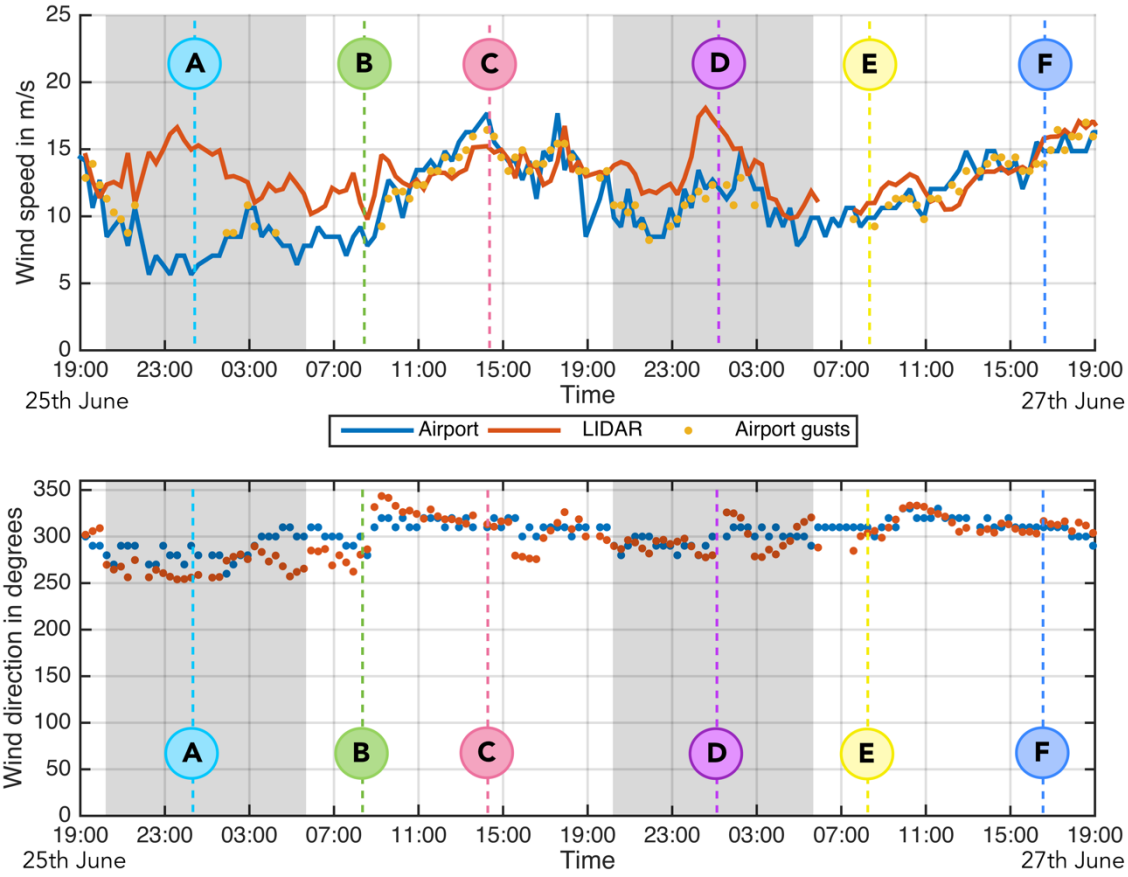

Figure 25 Comparison of lidar retrieved and airport AWOS wind speed (above) and wind direction (below). The retrieval at sections A,B,C,D,E and F are shown figure 26. The gray areas show data acquired at night.

b) ***Initial validation.*** To test the performance of the retrieval, an intercomparison of lidar retrieved winds with Tehachapi airport's wind data was performed. Tehachapi airport maintains a standard airport weather observing system (AWOS) with a cup and vane anemometer measuring horizontal surface winds. Unfortunately, the airport was located just outside maximum range of the lidar and ~230m below the lidar scan (Figure 24) . For the horizontal location

mismatch, the lidar data closest to the airport's location was used in the validation. For the height mismatch, airport data was interpolated to the lidar's elevation using the power law interpolation (Eq. 3.18) with α=1/7 (Spera & Richards 1979).

$$\mathrm{U}_{@\,Z} = \mathrm{U}_{surface}\left(\frac{Z}{Z_{surface}}\right)^{\alpha} \tag{3.18}$$

where, 'U' is the wind speed and 'Z' is the height above the ground. Figure (25) shows the lidar retrieved winds along with the power law extrapolated airport data and gusts (no power law extrapolation) observed at the surface. Gusts were reported when the maximum recorded wind speed exceeded the 10-minute averaged wind speed by 10kts (ICAO 1998). The error in windspeed (ΔU), wind direction (Δφ) and Pearson correlation coefficient (R) are calculated according to Eq. (3.19), (3.20) and (3.21).

$$\Delta\mathrm{U} = \sqrt{\frac{1}{N}\sum_{i=1}^{N}\left(\mathrm{U}_{lidar} - \mathrm{U}_{airport}\right)^2} \tag{3.19}$$

$$\Delta\varphi = \sqrt{\frac{1}{N}\sum_{i=1}^{N}\left[tan^{-1}\left(\frac{u_{lidar}v_{airport} - v_{lidar}u_{airport}}{u_{lidar}u_{airport} + v_{lidar}v_{airport}}\right)\right]^2} \tag{3.20}$$

$$R = \frac{COV(\mathrm{U}_{lidar}, \mathrm{U}_{airport})}{\sigma_{lidar}\sigma_{airport}} \tag{3.21}$$

where, '$COV()$' is the covariance and 'σ' is the standard deviation.

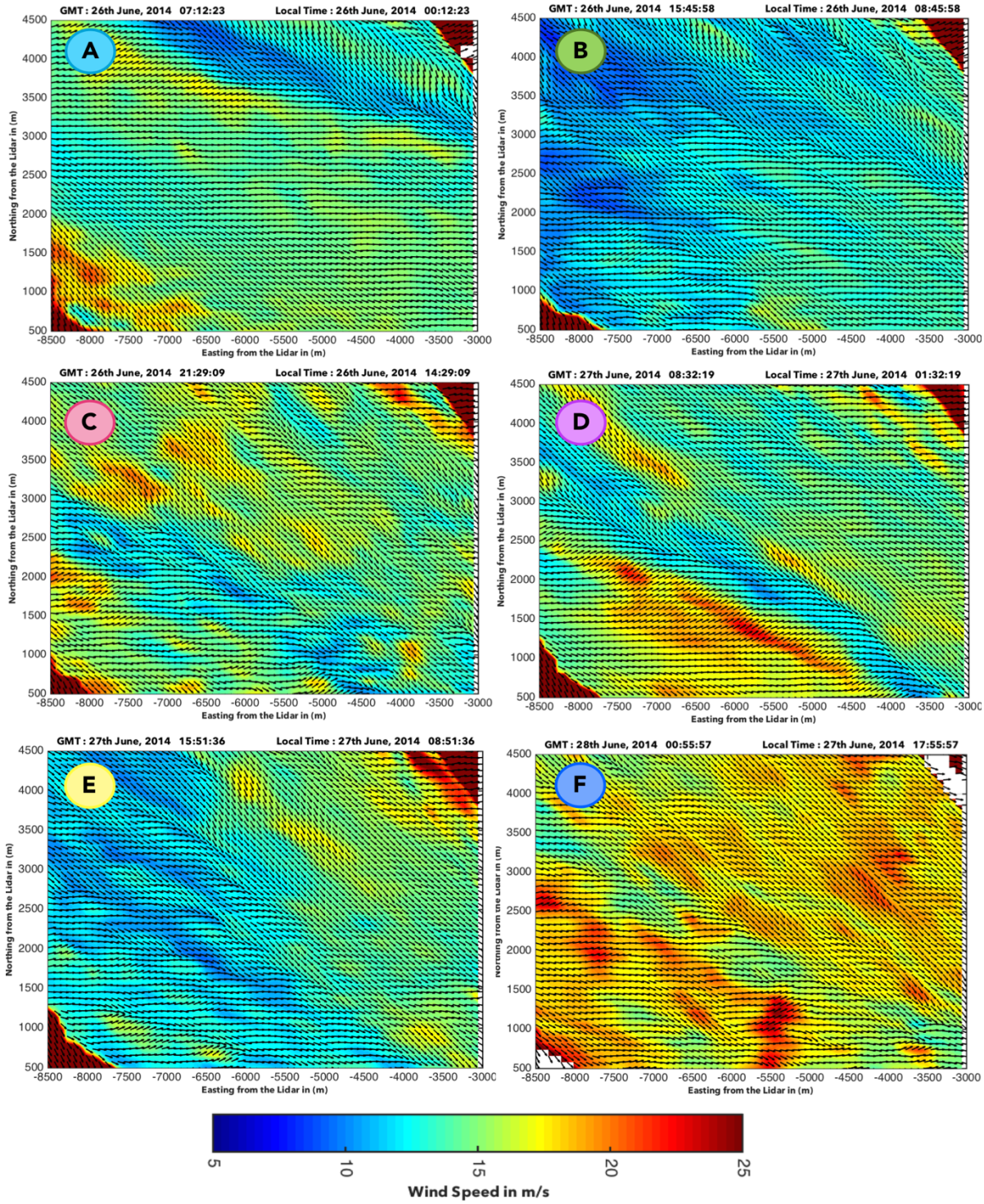

Figure 26. The lidar vector retrieval at sections A, B, C, D, E and F shown figure 25

Table 3.2

Retrieval validation study results

	Wind speed error (ΔU)	**Wind direction error (Δφ)**	**Correlation coefficient (R)**
Day	1.9279 m/s	14.3653°	0.6658
Night	4.5991 m/s	19.4040°	0.2624

From Table 3.2, we can see that errors from the day are lower than errors at night. A possible cause of the error could be the power law interpolation. In general, the power law exponent 'α' in Eq. (3.13) is a complex function that depends on local climatology, terrain, surface roughness, atmospheric stability and time of the day among many other factors. Using a constant value for 'α' could be an oversimplification (Spera & Richards, 1979). However, α=1/7 used in this study approximately holds for neutrally stable atmosphere (i.e., during the day) and could lead to errors in the estimates during the night. This could explain the relatively high errors and smaller correlation values during the night. The higher errors in general could be attributed to the fact that the flow is predominantly "complex". Measurements in complex flows have been known to exhibit persistent differences between point measurements (e.g. sonic anemometers) and area measurements (e.g., lidars, Radars) even when the devices are operated according to industry standards. In the current study, this issue of

variability could be exacerbated due to the location and height mismatch between the measuring devices. In lieu of the above issues, a qualitative comparison from figure 25 and figure 26, shows that flow features (E.g., presence of gusts) are captured and correlate well with when the airport data reports gusts.

3.3.2 Data from FINO-1 platform, North Sea

FINO-1 (Forschungsplattformen in Nord- und Ostsee Nr.1) is a German offshore wind energy research platform located close to the Alpha Ventus wind farm in the North Sea. As a part of an extensive offshore measurement campaign to improve the understanding of marine boundary layer, offshore wake propagation effects and air- sea interaction, two scanning Doppler wind lidars (Leosphere's windcube 100s) were installed on the FINO-1 platform to perform various Dual- doppler and vertical profiling scans. On 31st, August, 2016, one of the lidars was configured to perform repeated low elevation angle (0.5°) PPI scans, primarily for the validation of the new 2D-VAR vector retrieval. The lidar scanned a 90° azimuthal sector in the direction of the wind farm (Figure 27), with a 2°/s scan speed, accumulation time of 1 second and a 25m range resolution, the lidar could produce one scan product approximately every 45 seconds. With a good atmospheric aerosol content, the returns were clean and the lidar was often was able to capture winds at distance exceeding 2.5km.

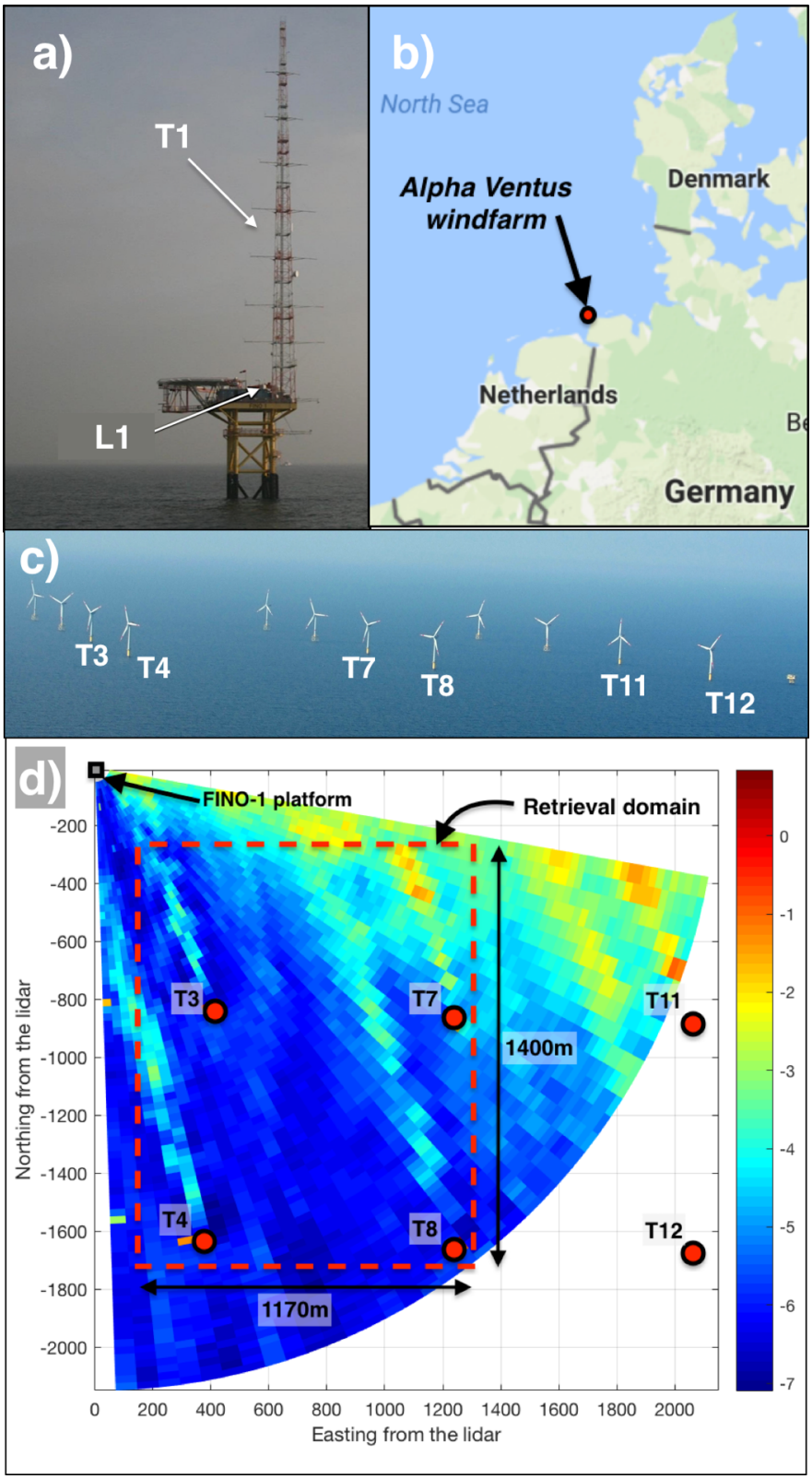
a)
T1
L1
b)
North Sea
Alpha Ventus windfarm
Denmark
Netherlands
Germany
c)
T3
T4
T7
T8
T11
T12
d)
FINO-1 platform
Retrieval domain
T3
T7
T11
T4
T8
T12
1400m
1170m
Northing from the lidar
Easting from the lidar
-200
-400
-600
-800
-1000
-1200
-1400
-1600
-1800
-2000
0
200
400
600
800
1000
1200
1400
1600
1800
2000
0
-1
-2
-3
-4
-5
-6
-7

Figure 27. (a) Fino-1 research platform showing the location of the lidar (L1) and the tower with cup and vane anemometers (T1), (b) Location of Alpha Ventus wind farm in North Sea (b) Photograph of Alpha Ventus windfarm looking North East. Fino-1 platform is situated to the left of the turbine T3 beyond the view of the camera. Photograph by Martina Nolte, CC by 3.0 (c) lidar scan with retrieval domain. T3,T4,T7,T8,T11 and T12 are wind turbines

By combining two successive scans for each time step, the wind field in a 1170m x 1400m domain, with a grid spacing of 30m was retrieved using the 2D-VAR algorithm and the traditional Volume Velocity Processing (VVP) algorithm. The VVP estimates were obtained by pooling all the radial velocity measurements within a 200 m region around each grid point in the domain and estimating the velocity components that best fit the measurements in a least squares sense. The 200m search space for VVP is required to obtain reliable estimates of (u,v) such that the variation in radial velocity due to orientation of the line of sight is greater than turbulent fluctuations in the wind (Clifton 2015). The downside of this implementation is that the VVP estimates become less reliable at grid points far away from the lidar. However, this wasn't an issue in the present study since only the grid point closest to the lidar was considered for obtaining the validation statistics with the anemometer data. The 10-minute averaged wind data from the cup and vane anemometer (CVA) situated at 33m LAT on the meteorological mast was used for corroborating and validating the wind retrieval from both 2D-VAR and

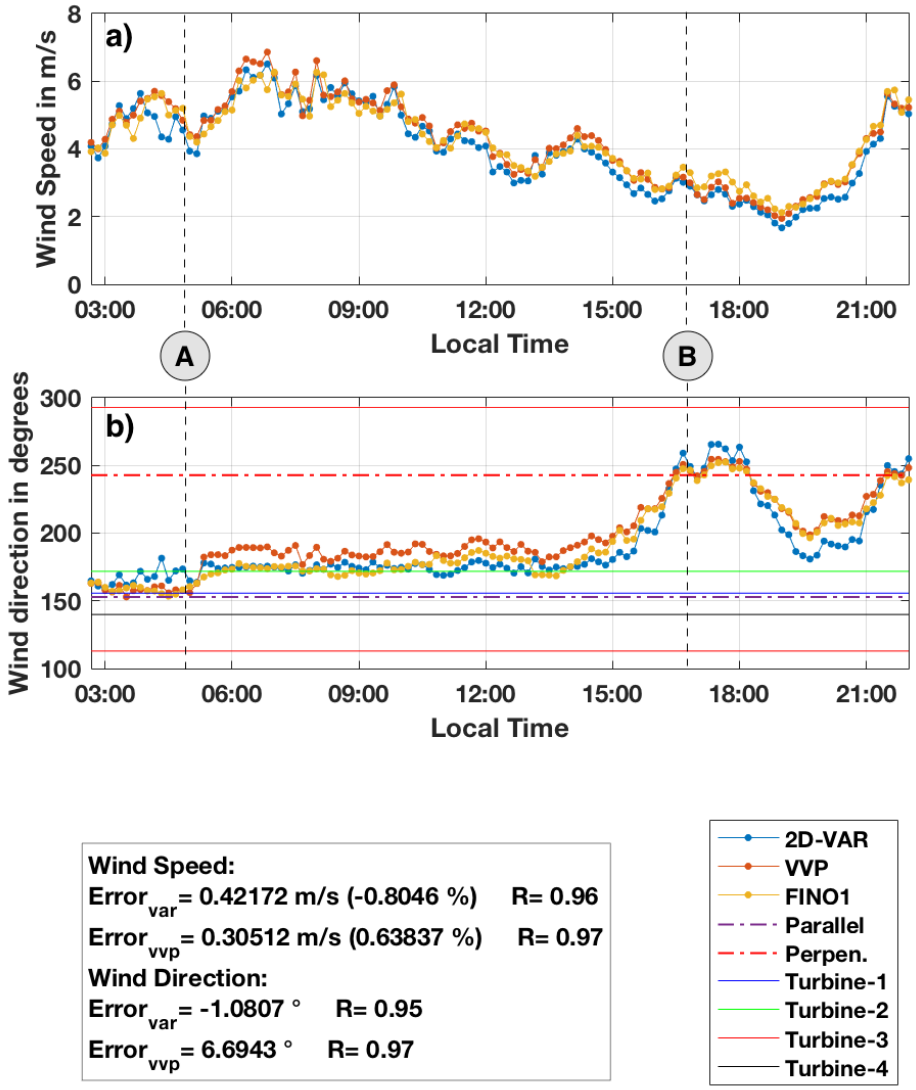

Figure 28. Comparisons of (a) wind speed and (b) wind direction, retrievals from 2D-VAR, VVP and CVA.

VVP algorithms. Since the lidar and the met mast were both located on the FINO-1 platform, retrieved wind vector from the nearest grid point (excluding the points along the boundary) was considered.

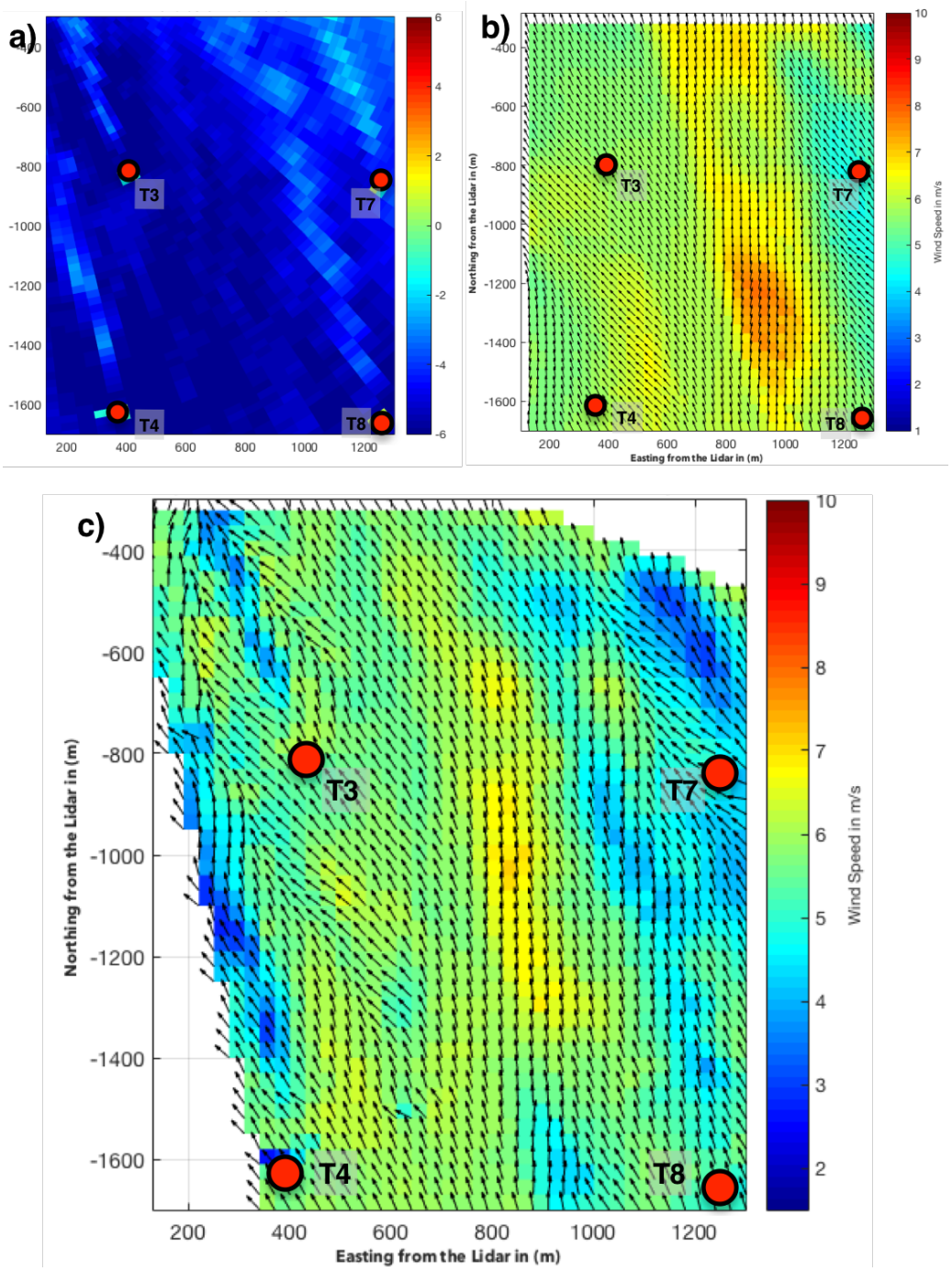

Figure 29. (a) Radial velocity plot, (b) VVP retrieval and (c) 2D-VAR retrieval applied on the data from the lidar at FINO-1 at point 'A' in figure 28. As seen, the 2D-VAR algorithm is able to capture wake and other small scale structures

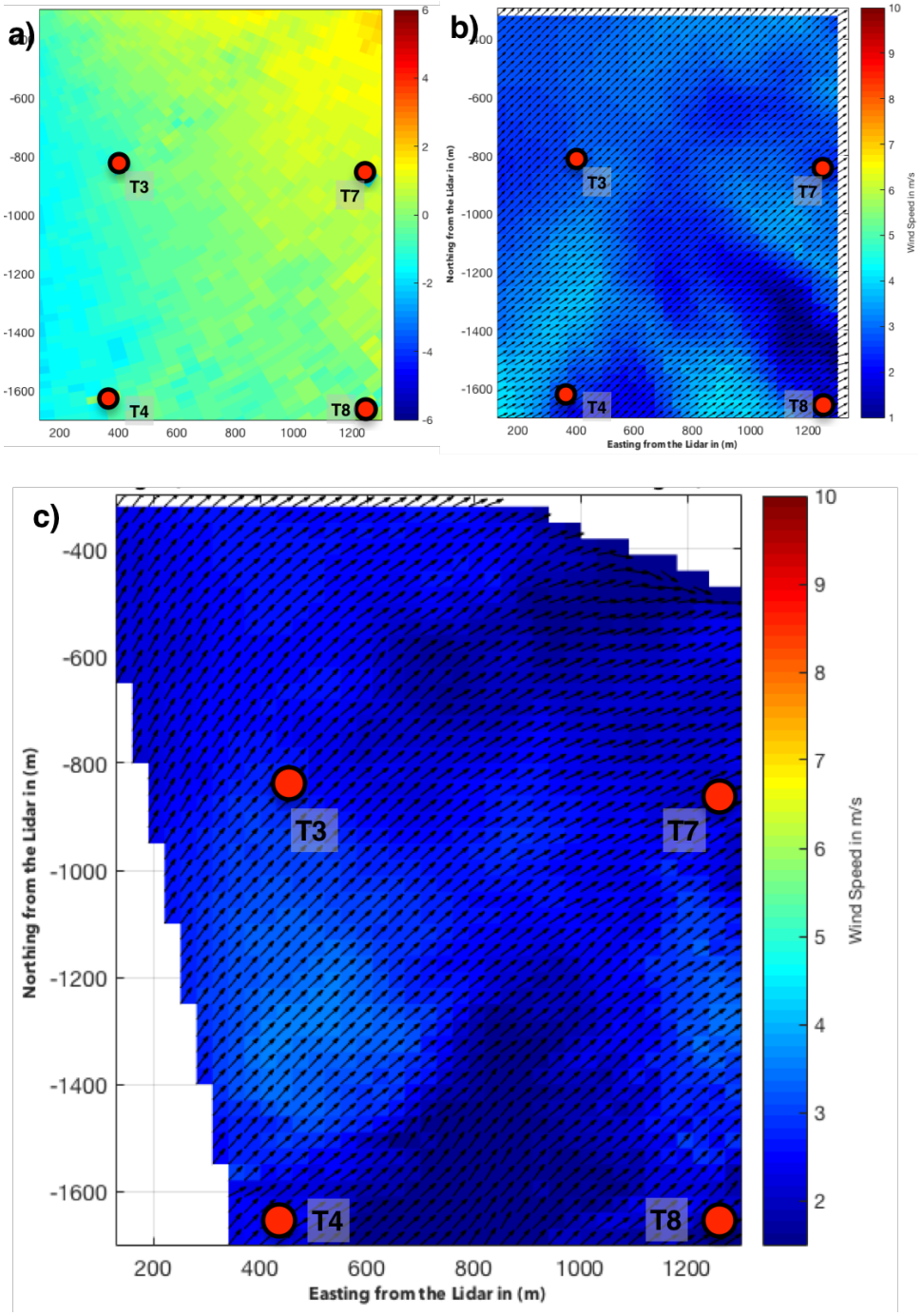

Figure 30. (a) Radial velocity plot, (b) VVP retrieval and (c) 2D-VAR retrieval applied on the data from the lidar at FINO-1 at point 'B' in figure 28 for a case when the flow is perpendicular to the lidar's scan.

In addition, the temporal profiles of wind speed and direction from the lidar were obtained by taking the mean of the retrieved u and v component of velocity within a 10-minute window around the CVA measurement time. The error in wind speed (ΔU), wind direction (Δφ) and Pearson correlation coefficient (R) were calculated according to Eq. (13), (14) and (15).

Figure 28 shows the temporal profiles from VVP, 2D-VAR and CVA. The 2D retrievals along with the radial velocity are shown in figures 29 and 30 corresponding to points 'A' and 'B' given in figure 28. These particular times were chosen to demonstrate instances when the flow was almost parallel and perpendicular to the lidar's view respectively. The violet and red dotted lines in the direction plots correspond to the azimuthal angle and its orthogonal counterpart of the grid point, whose wind values are plotted in the figure. From Table 3.3 and Figure 28, it is evident that both VVP and the 2D-VAR methods accurately estimate the mean flow, although VVP performs slightly better primarily due to its underlying formulation which is designed to obtain the mean quantities. The downside of this is the loss of local flow structure as seen in figure 29. It is evident from this figure that the wind vectors estimated by the 2D-VAR algorithm corroborate well with the radial velocity values (Figure 31 and Figure 32) especially in capturing small scale flow structures, including what appear to be wakes behind the wind turbines. All this small scale information is essentially lost in the VVP retrieval.

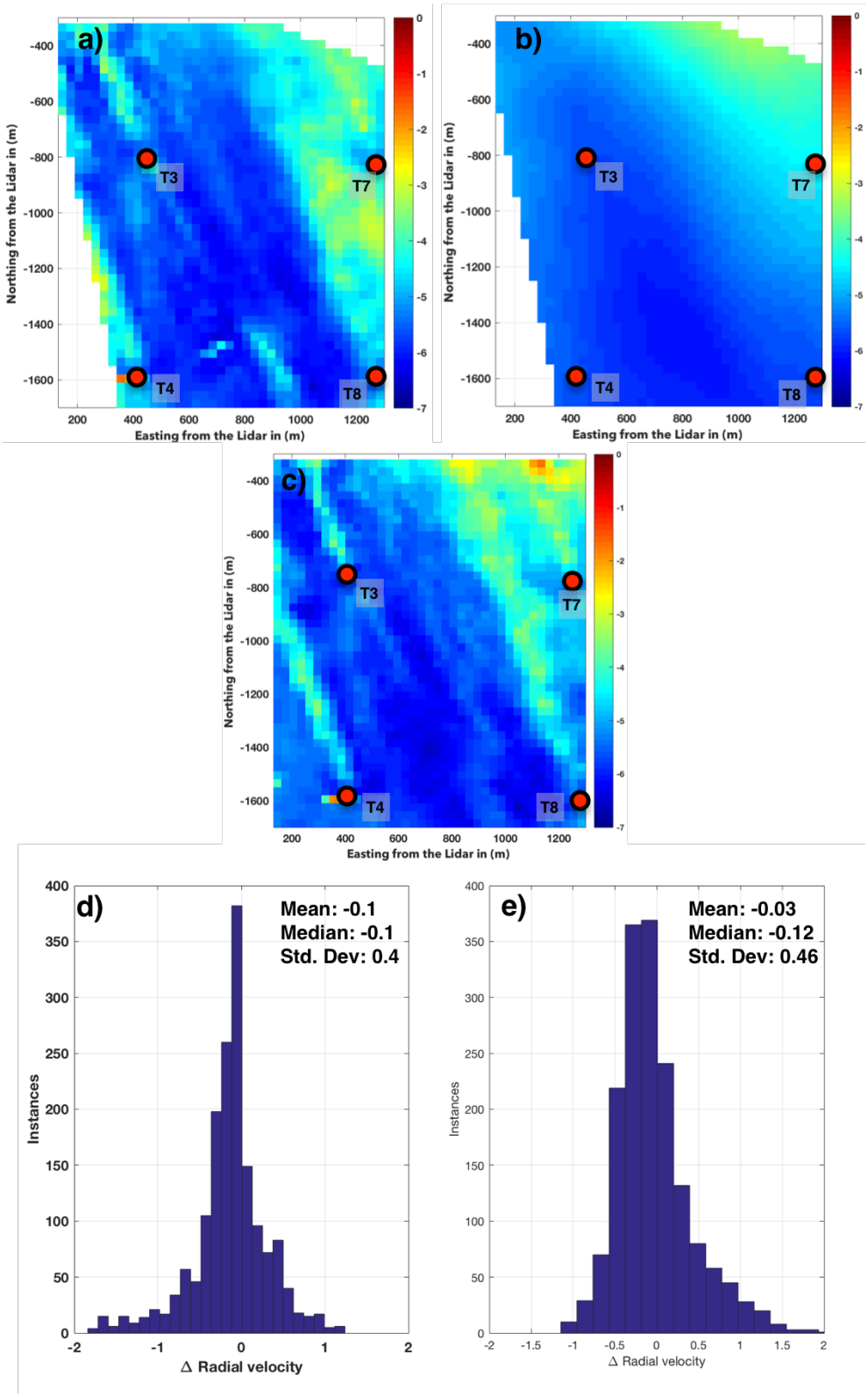
a)
b)
c)
d)
e)
T3
T4
T7
T8
Northing from the Lidar in (m)
Easting from the Lidar in (m)
Mean: -0.1
Median: -0.1
Std. Dev: 0.4
Mean: -0.03
Median: -0.12
Std. Dev: 0.46
Instances
Δ Radial velocity

Figure 31. (a) Radial velocity obtained from 2D-VAR, (b) Radial velocity obtained from VVP retrieval and (c) Observed radial velocity, (d) Histogram of radial velocity error for 2D-VAR, (e) Radial velocity error for VVP retrieval.

Table 3.3. Validation of 2D-VAR and VVP with 10-minute averaged CVA data

Algorithm/ Variable	**Wind speed error**	**Wind speed correlation coefficient**	**Wind direction error**	**Wind direction correlation coefficient**
2D-VAR	0.42 m/s (0.8%)	0.96	-1.1°	0.95
VVP	0.30 m/s (0.6%)	0.97	6.7°	0.97

3.5 Summary

There is a need for accurate and computationally efficient vector retrieval algorithms for Doppler wind lidars especially for applications involving short term wind power forecasting and dynamic wind turbine control. Existing wind retrieval algorithms are either incapable of retrieving small scale (turbine scale) flow structures or computationally expensive to be used in real time applications. To address this, an efficient 2D-VAR algorithm was developed and tested on lidar data from recent field deployment.

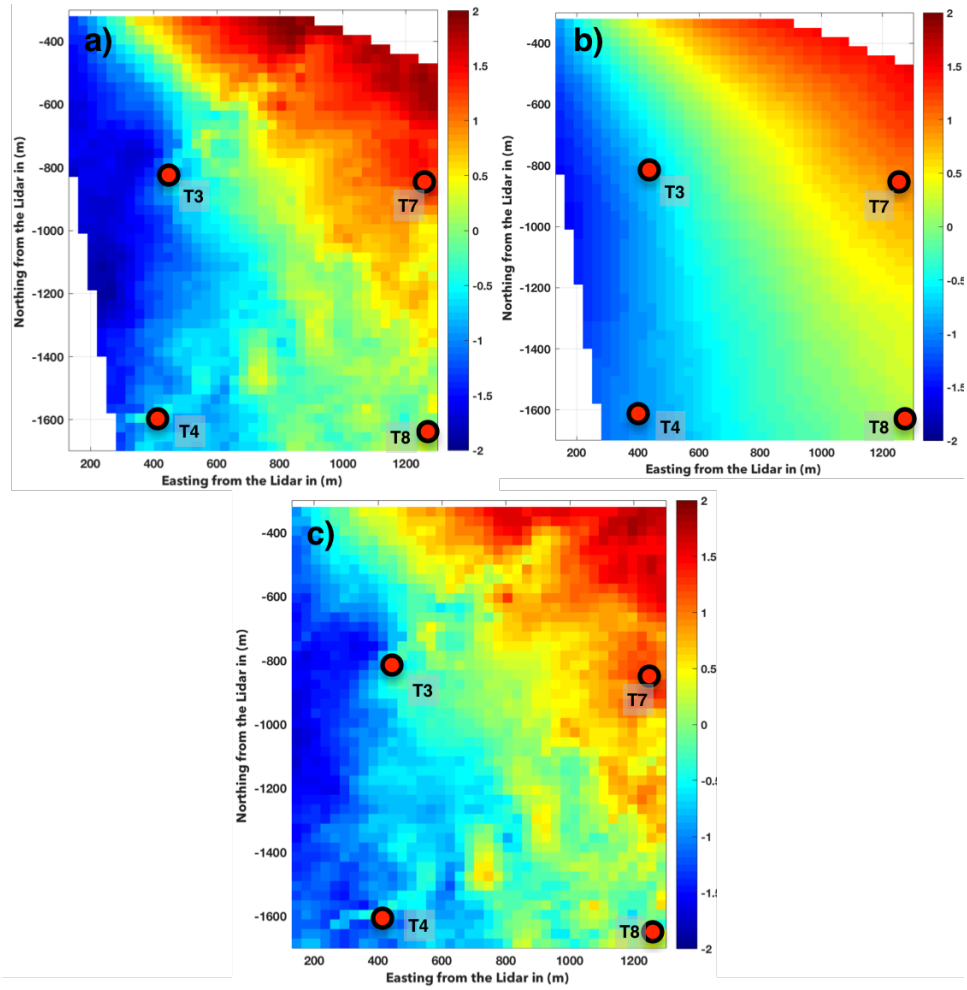
a)
b)
c)
T3
T4
T7
T8
Northing from the Lidar in (m)
Easting from the Lidar in (m)
-400
-600
-800
-1000
-1200
-1400
-1600
200
400
600
800
1000
1200
2
1.5
1
0.5
0
-0.5
-1
-1.5
-2

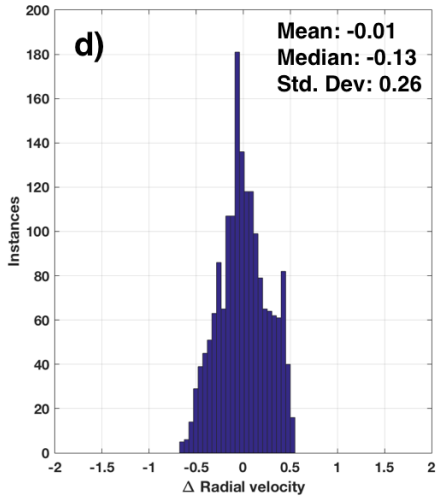
d)
Mean: -0.01
Median: -0.13
Std. Dev: 0.26
Instances
Δ Radial velocity
0
20
40
60
80
100
120
140
160
180
200
-2
-1.5
-1
-0.5
0
0.5
1
1.5
2

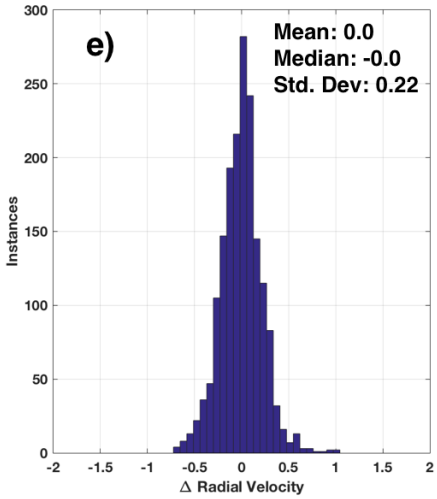
e)
Mean: 0.0
Median: -0.0
Std. Dev: 0.22
Instances
Δ Radial Velocity
0
50
100
150
200
250
300
-2
-1.5
-1
-0.5
0
0.5
1
1.5
2

Figure 32. (a) Radial velocity obtained from 2D-VAR, (b) Radial velocity obtained from VVP retrieval and (c) Observed radial velocity, (d) Histogram of radial velocity error for 2D-VAR, (e) Radial velocity error for VVP retrieval, for an instance where the flow is perpendicular to the lidar line of sight.

The general retrieval is based on a parameter identification (PI) method in which the parameters (vector field) is retrieved by seeking a solution which minimizes a cost function comprised of constraints pertaining to the flow field. While there have been 3D retrievals developed in the past based on PI technique, it was observed that for scans with low elevation angles the constraints in the cost function to be minimized, could be simplified and new constraints corresponding to the tangential velocity and the advection of radial velocity could be derived from the radial velocity equation. Expressions to calculate the weights for the respective constraints were derived based on the relative importance of the constraint in a given scenario, allowing the retrieval to be automated requiring minimal user intervention.

The retrieval was tested on data from two different lidars, a 1.6μm LMCT Windtracer lidar and a Leosphere's Windcube 200S lidar. data from recent field deployments at an onshore and an offshore wind farm respectively. The retrievals in both the cases were validated with measurements from a reference cup and vane anemometers. Although the results from the Tehachapi dataset showed large errors between the retrieval and the lidar, most of the variability could be ascribed to the location mismatch between the reference sensor and the lidar scan (~ 200m difference in elevation)..

The lidar data from the Alpha Ventus wind farm however, showed very good correlations and a very high accuracy for a single Doppler lidar vector retrieval, in the retrieved wind speed and direction when compared with data from a cup and vane anemometer located on the FINO-1 platform at roughly the same elevation as the lidar scan. One limitation of this study was that, the accuracy of the retrieval in the spatial domain could not be quantified due to the lack of instrumentation in the lidar scan region. However, analysis from this exploratory study showed that the algorithm while being computationally efficient with fast runtime (~ 3s in MATLAB running in a laptop powered by a 2.4GHz intel core i5 processor), was able to capture local structure in the flow including possible wakes from the wind turbines.

CHAPTER 4

ATMOSPHERIC DATA VISUALIZATION IN MIXED/AUGMENTED REALITY

Atmospheric science has seen a tremendous advancement in the tools and methods to study the atmosphere over the years. Remote sensors like lidars can make unseen structure in objects or flow fields visible with higher spatial and temporal resolutions. However, it is often difficult to connect static, two-dimensional graphics to a natural visual view of either an object or a three-dimensional flow field necessitating an interactive 3D visualization environment that is simple and intuitive to the user. Visualization in mixed reality provides one such environment that taps into intuitive human perception by merging computer generated views of digital objects (or flow fields) with natural views. This type of visualization is particularly useful in situations where the user's primary task requires him/her to shift focus away from the computer screen (E.g., Air traffic controllers, Pilots).

In this chapter a novel mixed reality data visualization application for atmospheric science data is explored and the methodology using game development platforms along with a few mobile applications demonstrating this technology are presented.

4.1 What is augmented reality and mixed reality?

Mixed reality/ Augmented reality taps into intuitive human perception by merging computer generated views of digital objects with natural views. Digital objects can be positioned in 3D space and can mimic real objects in the sense that walking around the object produces smoothly changing views toward the other side. Only recently have

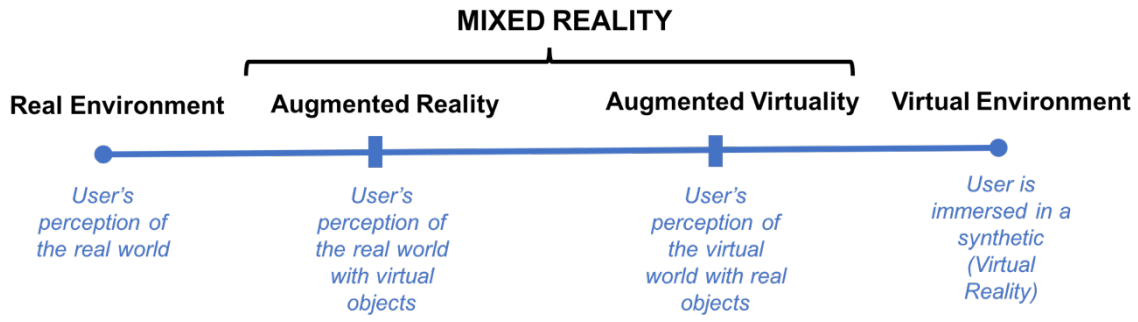

Figure 33. Mixed reality continuum as given in Milgram et al. (1994). It shows different interfaces which have various levels of immersion with real world on the left and fully immersive virtual reality interfaces on the right.

advances in gaming graphics advanced to the point that views of moving 3D digital objects can be calculated in real-time and displayed together with digital video streams. Auxiliary information can be positioned and timed to give the viewer a deeper understanding of a scene -- for example, a pilot landing an aircraft might "see" zones of shear or decaying vortices from previous heavy aircraft. A rotating digital globe might be displayed on a table top to demonstrate the evolution of El Nino (Figure 34b).

Although the concept of a transparent display has been around for some time (Sutherland, 1968), the term 'augmented reality' was first coined by Caudell & Mizell (1992) to describe the head-mounted displays used by workers at Boeing to guide them with the assembly process. "Mixed reality" (MR) is an umbrella term used to describe any system which combines real and virtual content (Milgram et al., 1994, Figure 33). If we place different user environments along a continuum with the real environment on one end and virtual environment (Virtual reality- Fully immersive displays) on the other,

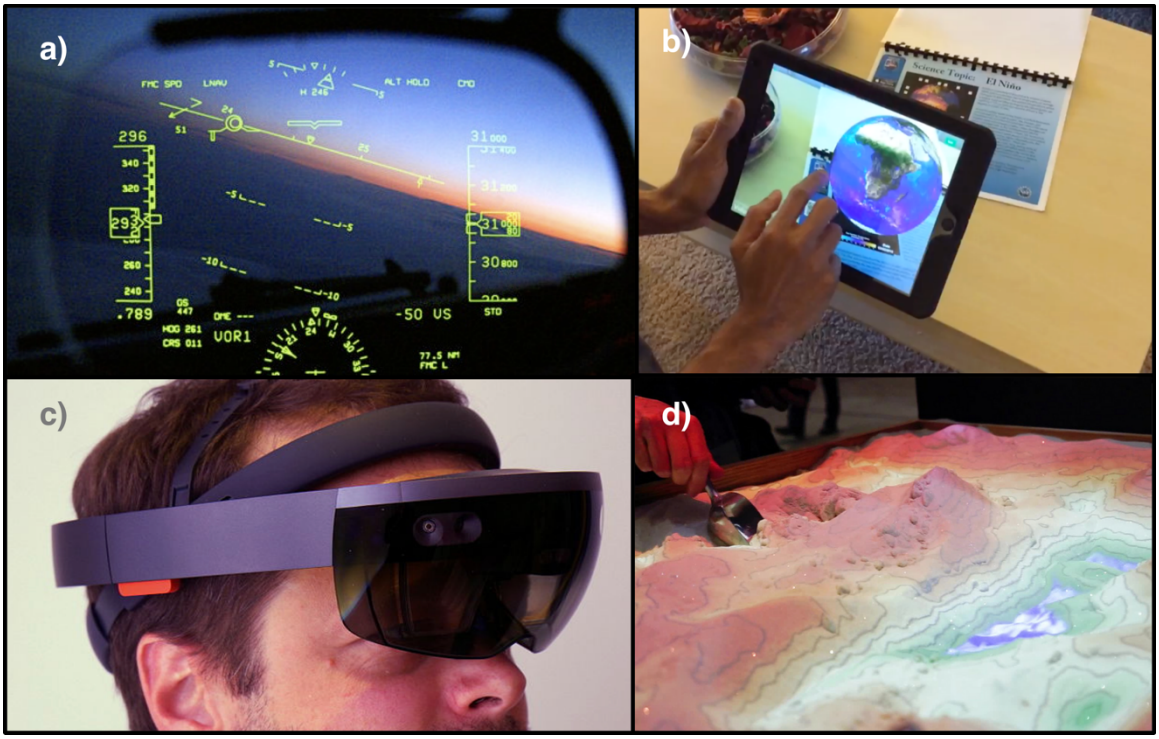

Figure 34. A few augmented reality examples (a) Heads up display (HUD) in an airplane, (Optical technology) *(Photo by Amber Case; CC by 2.0)* (b) Meteo-AR mobile application (handheld-video based application) (c) Microsoft's Hololens (Heads up display using optical technology) *(Photo by Kai Kowalewski; CC by 4.0*) (d) AR Sandbox (spatial-projector based Augmented reality) *(Photo by Trevor Dykstra; CC by 2.0)*

any environment in-between these two extremum can be classified as mixed reality (MR) of which Augmented reality (AR) is the best known and more popular- The other one being Augmented Virtuality (AV) in which a user's otherwise virtual world is augmented with real world objects. An example of an AV system would be a virtual reality system

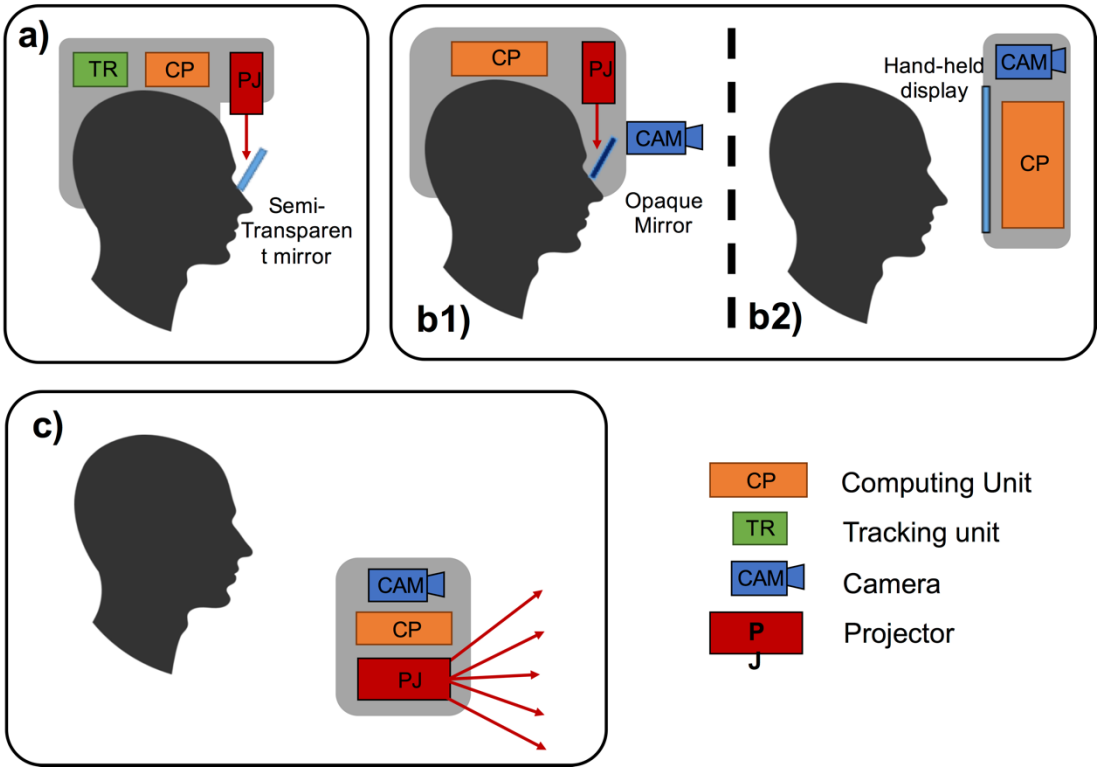

Figure 35. Schematic of different AR display systems classified based on the display technology; (a) Head-Mounted optical display system, (b1) Head-Mounted Video based display, (b2) Hand held video based system (c) Spatial AR system.

with a real rendering of the user's hands for interaction in the virtual world. Given the popularity of AR compared to AV, the terms MR and AR are often used interchangeably.

4.2 Types of AR systems:

For an interface to be classified as AR, it must satisfy three criteria (Azuma et al., 2001):

i. Present real and virtual content together in a real environment

One of the key features which distinguishes AR from other types of visualization

ii. *Virtual objects align with the real world and registers in 3D*

This distinguishes displays which form simple 2D-overlays over video feeds from AR

iii. *The content must be interactive in real time*

This helps in distinguishing popular visual effects often used in movies from AR (E.g. chroma key compositing used in Hollywood; which is a post-production technique and not interactive).

At the heart of any AR system is a display technology which combines the real and virtual (commonly called as a 'combiner'). There are three major types of AR systems classified based on the display technology (Carmigniani & Furht, 2011): a) Optical, c) Video based, d) Spatial. (See Figure 35)

a) ***Optical.*** In these systems, the user views the world through a semitransparent mirror onto which, a projector unit, projects relevant graphics. The mirror being semi-transparent, allows the user to view the real world along with the projected virtual objects. Smart glass based Head mounted displays (HMDs -Figure 34c) and Head-up displays (HUDs) (Figure 34a) fall in this category. Since the device needs to render/project only the virtual content, these systems have lower graphics requirements and were commonplace in almost all early implementations of AR. However, since the user has a direct view of the real world (which runs in real-time), even small errors in alignment of the virtual objects with the real world are instantly recognizable, increasing the dependence on a reliable and accurate tracking system. Moreover, these unconventional displays often tend to be

expensive and until recently have seen only military and industrial applications. Some of the recent consumer based AR systems which implement optical system are the Microsoft's Hololens (Figure 34c), Google Glass and Meta2 headset.

b) ***Video based.*** In video based AR, live video of the world from a camera is displayed on a screen placed in front of the user. Since the user now sees the world through a video feed, digital content can be blended/layered in the video feed prior to rendering, to create the AR experience. They could either be a head mounted VR display with cameras (E.g. Steptoe & Steed, 2014) or smartphone/tablet computer. These systems are gaining popularity due to the ubiquitous availability of smartphones and low cost VR headsets. Moreover, since cameras are integrated into the viewing device, the registration (tracking) issue can be solved by implementing computer vision based algorithms which have high accuracy compared to other registration techniques. An example of a handheld video based AR system is Volkswagen's MARTA (mobile augmented reality technical assistance) application used to visualize service information, steps and tools required to complete the maintenance task in real time in augmented reality (Stanimirovic et al., 2014). One of the limitations of HMDs using video based systems is that these devices tend to be bulky and are not suitable for extended usage in the current form (Rolland et al., 1995, Van Krevelen & Poelman, 2010).

c) ***Spatial.*** In spatial AR systems, the virtual content is projected onto real world objects by means of a projector, eliminating the need for the user to wear an HMD

or hold any display in his/her hands. An independent tracking system could be used to detect user input and adjusting the virtual objects. An example of such a system is the *Sixth sense technology* (Mistry et al., 2009) which is a wearable gestural AR interface. In this, virtual content is displayed on any surface by projecting information using a tiny projector and the user input is captured by a camera mounted on a hat or a wearable pendant around the neck. Another example is the *Augmented Reality Sandbox* (Reed et al., 2014), which allows students to learn earth science concepts by shaping real-world sand. As the students shape the real sand, a kinect sensor (Microsoft's IR based depth sensor) positioned on the top, registers the surface in real time to produce simulated topographic contour lines, and virtual water in real time (Figure 34d). However, these systems have lower mobility, lower resolution and a short depth of focus which limit their application to indoor settings.

4.3 Motivation for the current project

Visualization techniques have evolved over time and MR data visualization is emerging as the new paradigm for interacting with digital content. Although the concept of MR/AR (AR or augmented reality- considered as a subset of MR and the term often used interchangeability with MR) has been known for many years, the ubiquitous availability of smartphones and tablet computers has led to an extraordinary growth of its applications in the mainstream over the recent years. In addition, HMDs that were popular primarily in the aviation industry, military and specialized research organizations in the past have now become affordable and accessible to general public given their

increasing popularity in the gaming industry. On the software side, modern game development platforms (Software used to develop computer games) have made the application development process simpler because of their efficient game engines and compatibility with multiple computing devices.

The primary purpose of this study is to demonstrate a novel application of MR in conjunction with atmospheric science data and present a brief methodology using modern game development platforms.

4.4 Relevant applications with atmospheric data

Aragon et al. (2005) first conducted a flight simulator based usability study of an airflow hazard detection system for rotorcraft pilots using AR. The study demonstrated a "dramatic improvement" in the performance of the helicopter pilots who used AR visualization under stressful operational conditions. Nurminen et al. (2011) presented another application of MR as one of the features of HYDROSYS system- An environmental data analysis and monitoring platform in which simulation results from integrated sensor data was visualized in MR using a specialized portable handheld computer. In a similar study, Heuveline et al. (2011) demonstrated a mobile AR system to visualize computational fluid dynamics simulation of wind flow around buildings in an urban environment.

The data visualization application presented in this study differs from the previous works in three main aspects- (i) Type of data being visualized, (ii) Target devices, (iii) Tools used in the application development. Compared to just simulation data used in

previous studies, the current application uses multidimensional data from atmospheric sensors with close to real-time application capability in addition to simulation. Moreover, as opposed to specialized equipment and development tools used for visualization in previous studies, the current work leverages on the ubiquitous availability of smartphones and game development tools making the technology accessible to a larger user base including independent researchers, small research groups and general audience.

4.5 General working scenario

Consider a typical field deployment with multiple sensors (e.g., instruments on a meteorological mast, radiosonde, Doppler lidars, weather stations etc.) measuring different atmospheric variables (see Figure 36). The network between the sensors and the visualization devices is based on a client-server model i.e., the data being visualized is streamed from the sensors and stored at a server and all the devices used for visualization (e.g. smartphones, HMDs etc.) obtain the data from this server as clients. In addition to storing the raw data from the sensors, the server also processes the raw data to produce appropriate files for visualization. On the visualization device, the user can either choose to automatically stream the data to be visualized as it becomes available (real-time) or manually step through the data in a retrospective mode.

The application on the viewing device (client) is designed to have two modes of operation: (a) the “onsite mode”- where the data from the sensors is presented as an overlay at the sensor’s physical location when viewed through the mobile device or HMD and (b) The “tabletop mode”- where the data being visualized (along with a scaled down

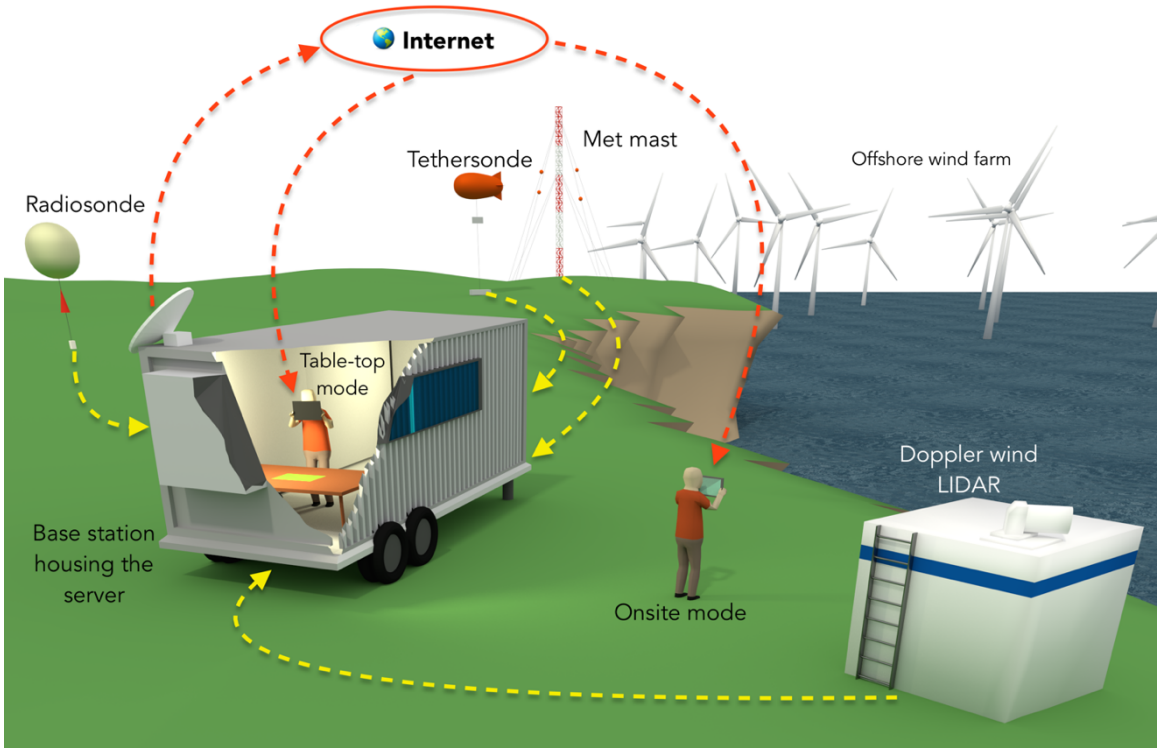

Figure 36. An illustration of a typical working scenario with data acquisition process shown with yellow dotted lines and visualization process shown with red dotted lines.

version of the 3D terrain) is overlaid on a surface when viewed through the mobile device or HMD.

4.6 Implementation on the viewing device

Computer games can be described as applications which enable human users to move and interact with virtual objects, driven by specific rules and mechanics, through a user interface. For instance, in the videogame 'Tetris', the user rotates and moves the tiles/blocks (virtual objects) using the computer keyboard (interaction) to match the patterns as they drop to the floor (mechanics). A game development platform is a

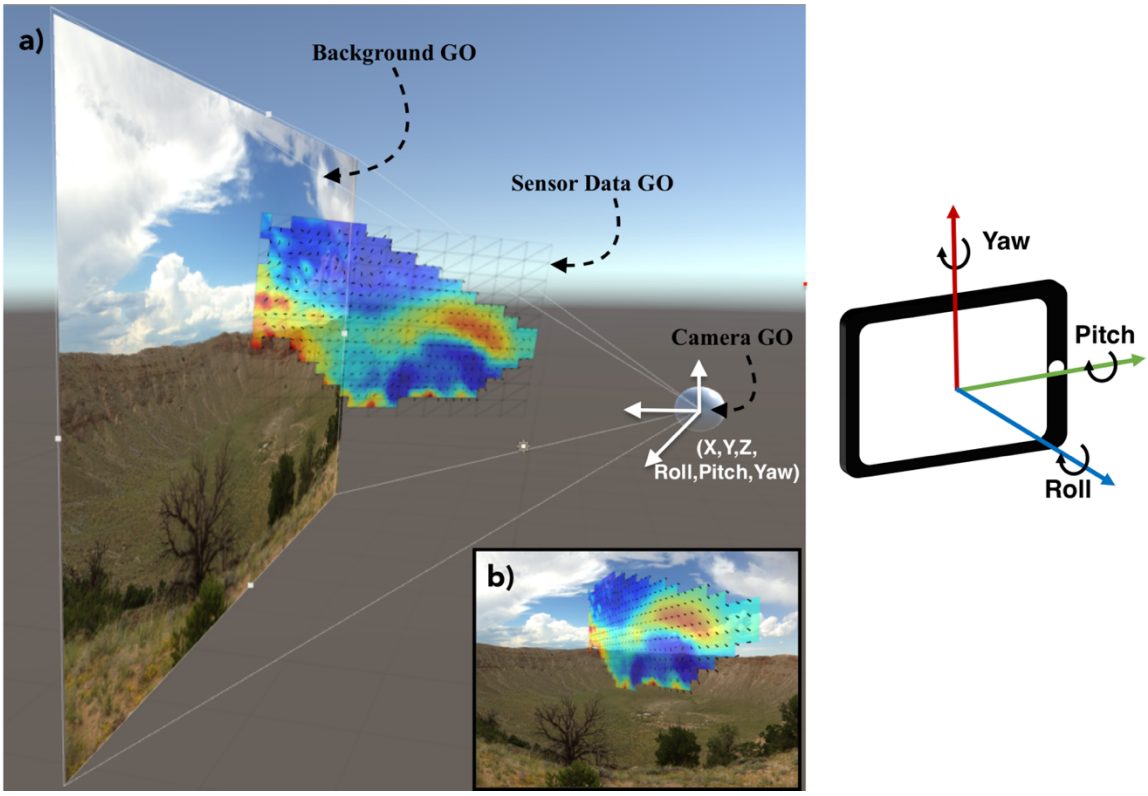

Figure 37. (a) An overview of the application setup in Unity, showing different GameObjects (GOs) used in the current project. The lines connecting the Camera GO with the Background GO denote the edges of the view frustum (Edges of the camera's field of view) of the Camera GO (b) The inset shows the output of the Camera GO (the user-view while running the application).

software system that provides a working environment to design these games, attach scripts (computer codes that specify the mechanics) and build the project (i.e., create an executable package through which the user can launch and play the game). An added advantage of using game development platforms is their multiplatform support, i.e.,

applications developed in the game development platform can be built for different devices (e.g. smartphones, tablet computers and many of the popular HMDs.)

A data visualization application was developed using Unity SDK (Unity Technologies, 2016). Following Unity's terminology, all virtual objects will be referred to as 'GameObjects' (GOs- basically objects inside a game) henceforth. There are three main GOs in this application (similar to the blocks in Tetris but in 3D): Sensor Data-GO, Camera-GO, and Background-GO (see Figure 37(a)). The Sensor Data-GO(s) corresponds to the data being visualized. In the example shown in Figure 37, it is a 2D vector field that is fixed at a known location in the virtual world. The location of the data is determined based on prior knowledge of the instrument's location. The Camera-GO functions as the eyes of the user into the virtual world, i.e., while running the application, the device's screen displays what the Camera-GO sees at the moment (see Figure 37(b)). Lastly, the Background-GO is a 2D plane that serves as a backdrop to the Camera-GO's output onto which live video from the device's physical camera is displayed (imagine a big screen that follows the Camera-GO as its backdrop wherever it currently points). Thus, the user can see the video streamed from the device's physical camera while simultaneously seeing the sensor data, whenever the Sensor Data-GOs comes within the field of view of the Camera-GO (Figure 37). The user interaction with this virtual world (and hence the MR experience) is controlled through the Camera-GO. The Camera-GO has 6 degrees of freedom (i.e., it can move along three directions in space (X, Y, Z) and rotate around each of these axes (roll, pitch, yaw)). By controlling these six parameters of the Camera-GO, the user can move and look around in the virtual world. The two

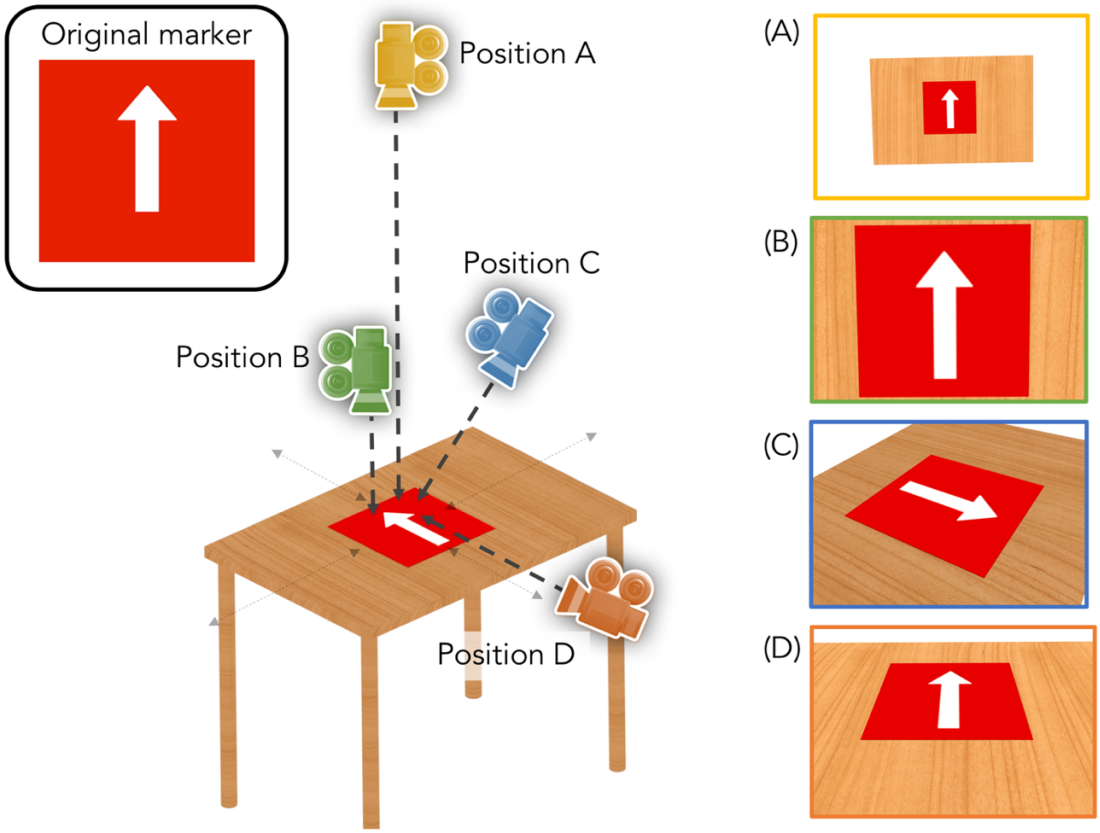

Figure 38. Working methodology of the table-top mode demonstrating how the image appears distorted based on the viewing angle of the device camera. The inset figures (A)-(D) correspond to the camera view at the corresponding positions. A marker detection framework (Vuforia SDK in this study) is used to calculate position and orientation of the camera relative to the marker.

modes of operation (i.e., the "on-site mode" and "table-top mode") differ primarily in input method of these 6 variables.

4.6.1 Onsite-Mode:

Smartphones, tablet computers and most of the wearable devices come equipped with GPS, magnetometer and gyroscope units. The onsite mode makes use of the data from these sensors to determine the 6 variables of the Camera-GO, i.e., GPS can be used to obtain the (X, Y, Z) position and the gyroscope (with the magnetometer) can provide the (roll, pitch, yaw) information. Thus, the Camera-GO aligns its view of the virtual world with the real world by mimicking the location and orientation of the viewing device. One of the major challenges of the onsite mode is the exact alignment of the atmospheric sensor data with real world objects relying solely on mobile sensors (GPS and IMU). The alignment process is limited by the accuracy of the location/orientation sensors, (i.e., the current GPS accuracy is about $\pm$10m) requiring the user to make fine corrections in the location while starting the application (After which the alignment holds without any user intervention). One way to address this issue in the future is by combining the current approach with a computer vision based approach (Klein & Murray, 2007).

4.6.2 Table-top mode:

The table-top mode uses a marker-based system to determine the position and orientation of the Camera-GO. Consider a square sheet of paper with some image (The marker) placed on a table (Figure 38). When this marker is viewed from different locations, the image appears distorted due to the perspective effect (Figure 38 (A)-(D)). By comparing this distorted image with the original image of the marker, the location and orientation of the camera relative to the location of the marker can be uniquely

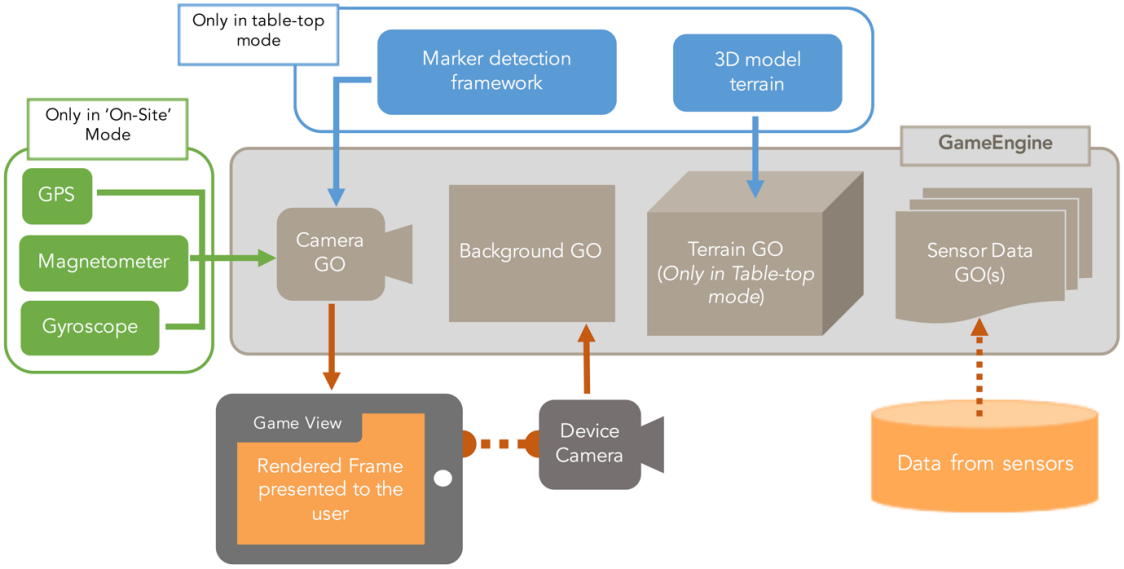

Figure 39. Illustration of the visualization process on the client side (i.e., in the mobile/tablet/HMD) running a game engine.

determined. This marker detection and tracking process is a well-studied problem in the field of computer vision and a number of frameworks are currently available. In the present study, this was implemented using the Vuforia SDK (PTK Inc., 2016)- a mobile SDK to create computer vision based AR systems. By centering the virtual objects at the location of the marker, the user can visualize these objects as an over lay on the live camera feed of the device. The virtual objects mentioned above could be static meshes (e.g., scaled version of the terrain) or interactive sensor data (e.g., windfield, temperature etc.) or a combination of both. The overall implementation on the device is given in figure 39.

4.7 Test case

For the purpose of demonstration, three different uses of the MR visualization were explored. First, the visualization method was tested with lidar data from METCRAX II field experiment. Figure 40a, 40b show the screenshots of the application running on a tablet computer in “on-site mode” and “table-top mode” respectively. The data being visualized is a 2D cross-section of the wind flow inside the Meteor Crater in Arizona, during a downslope windstorm-type flow (DWF) event. The DWF event is an intermittent, short lived wind flow in which the ambient flow over the crater descends inside the crater and rebounds along the crater side wall forming a rotor and a lee wave. The colors represent wind speed with the vectors showing wind direction. The dataset shown spans a two-hour time period with a temporal resolution of 1 minute and is visualized in retrospective mode (i.e., recorded data, although it has near real time capabilities limited by the bandwidth of the internet connection and the data acquisition time of the sensors). The example shown here with a tablet computer is meant to be proof of concept, and such a visualization will prove valuable in situations where decision makers need to quickly, identify and determine the physical location of an atmospheric event. For instance, a pilot landing an aircraft could use it to see zones of shear or decaying turbulent regions from previous aircraft in his plain sight through his head mounted display.

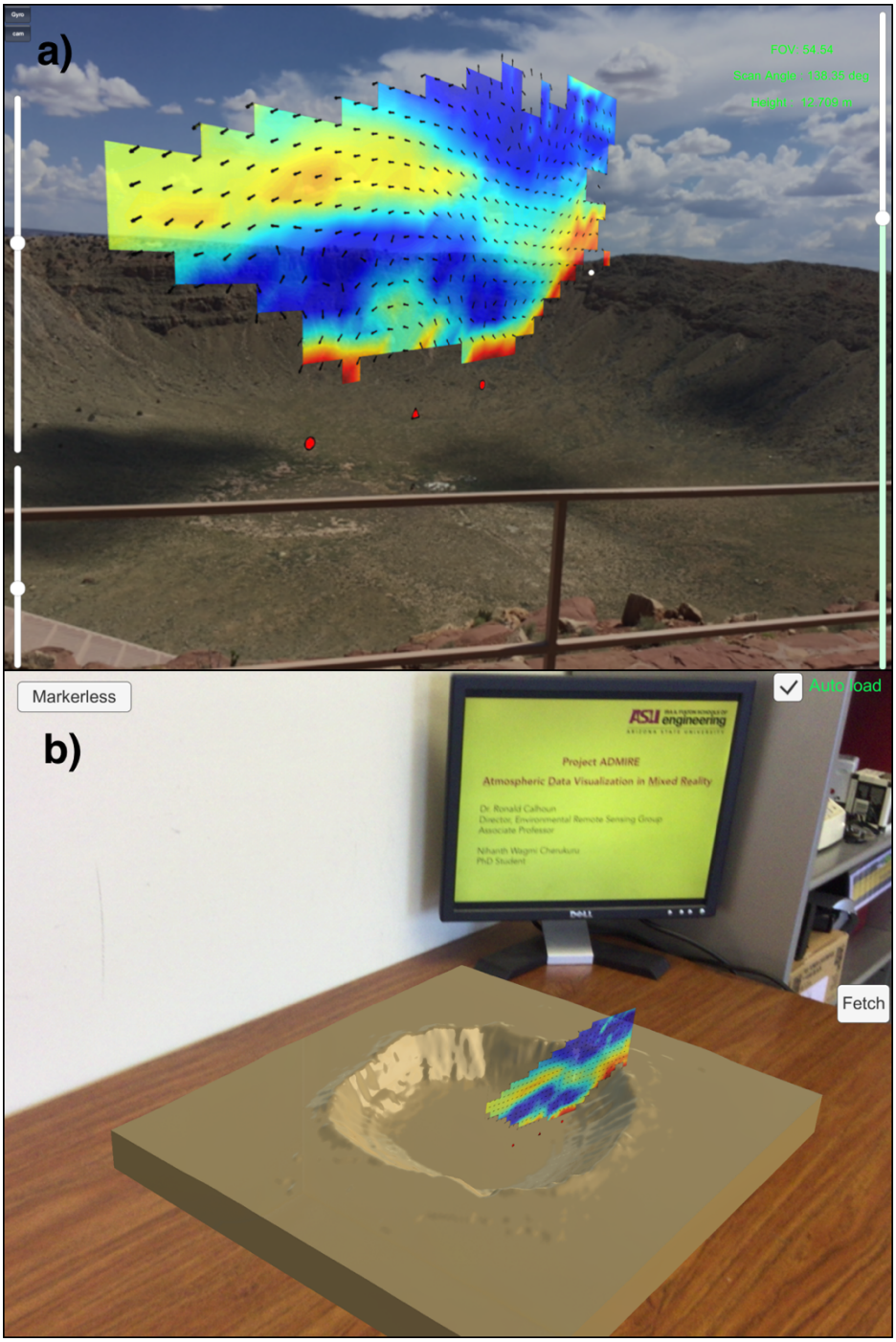

Figure 40. Screenshots from the tablet computer running the data visualization application. (a) Onsite mode- The scan was rotated about the vertical axis get a better viewing angle, (b) Table-top mode.

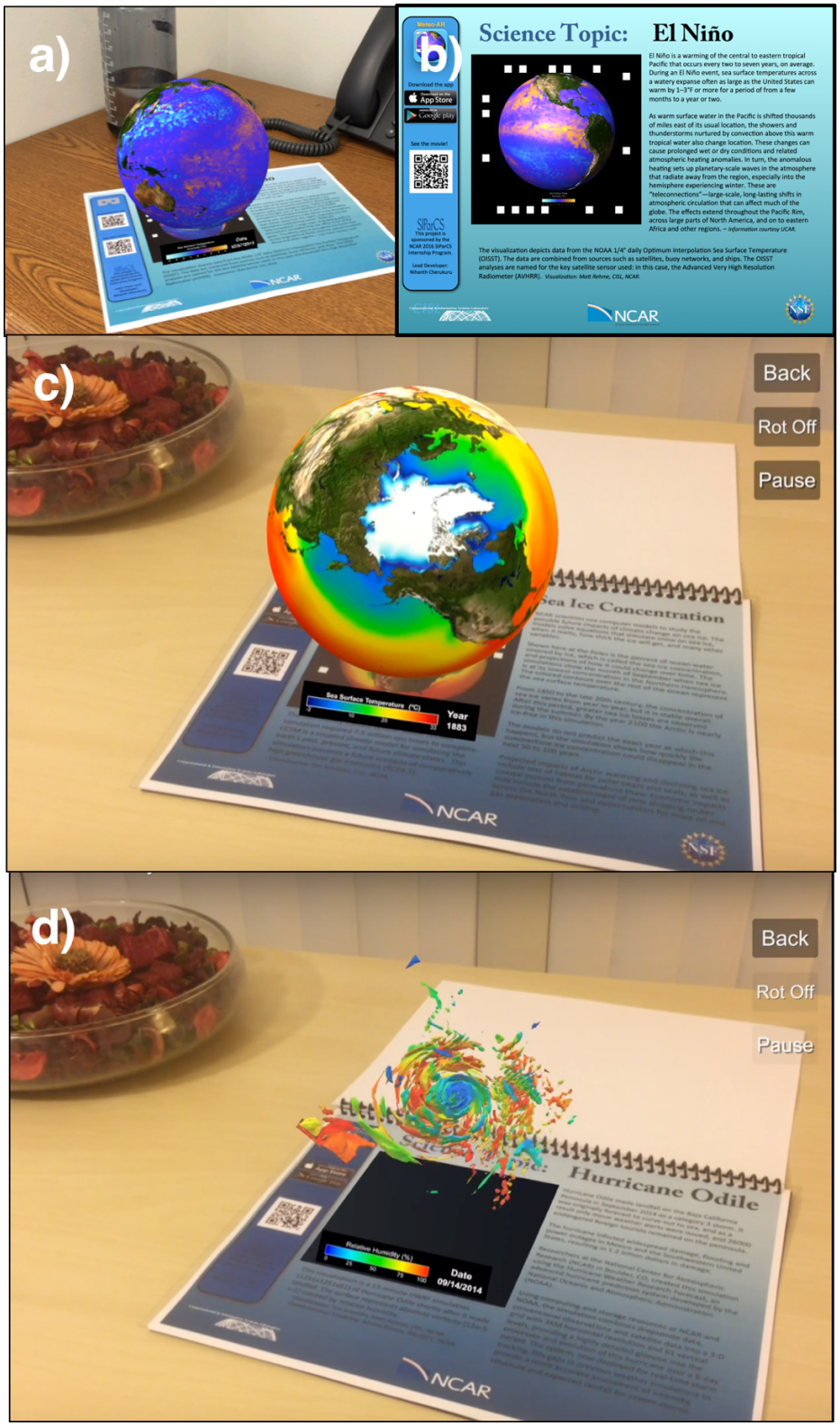
a)
b)
Science Topic: El Niño
El Niño is a warming of the central to eastern tropical Pacific that occurs every two to seven years, on average. During an El Niño event, sea surface temperatures across a watery expanse often as large as the United States can warm by 1–3°F or more for a period of from a few months to a year or two.
As warm surface water in the Pacific is shifted thousands of miles east of its usual location, the showers and thunderstorms nurtured by convection above this warm tropical water also change location. These changes can cause prolonged wet or dry conditions and related atmospheric heating anomalies. In turn, the anomalous heating sets up planetary-scale waves in the atmosphere that radiate away from the region, especially into the hemisphere experiencing winter. These are "teleconnections"—large-scale, long-lasting shifts in atmospheric circulation that can affect much of the globe. The effects extend throughout the Pacific Rim, across large parts of North America, and on to eastern Africa and other regions. – Information courtesy UCAR.
The visualization depicts data from the NOAA 1/4° daily Optimum Interpolation Sea Surface Temperature (OISST). The data are combined from sources such as satellites, buoy networks, and ships. The OISST analyses are named for the key satellite sensor used. In this case, the Advanced Very High Resolution Radiometer (AVHRR). Visualization: Matt Rehme, CISL, NCAR.
Download the app
App Store
Google play
See the movie!
SPaCS
This project is sponsored by the NCAR 2016 SPaCS Internship Program.
Lead Developer: Niharth Cherukuru
NCAR
c)
Back
Rot Off
Pause
Sea Surface Temperature (°C)
Year
1883
NCAR
d)
Back
Rot Off
Pause
Relative Humidity (%)
Date
09/14/2014
NCAR

Figure 41. Screenshots from the tablet computer running the METEO-AR data visualization application. (a) Screen shot of the application visualizing sea surface temperature anomaly showing the evolution of the 2015-2016 El Niño event, obtained from an optimal interpolation data assimilation scheme, (b) Science page corresponding to the El Niño dataset shown in (a). The pattern with the white dots surrounding the image in the marker help the marker detection routine to identify the correct dataset to render corresponding to the marker sheet, (c) An example showing the September Sea Ice concentration in the Arctic region, (d) Another example showing the application, rendering a 3D model of Hurricane Odile.

In an educational setting, AR/MR technologies make the atmospheric data tangible by allowing students to interact with the data as if they were physical objects providing an intuitive and richer learning experience. Figure 41 demonstrates one such application. Similar to the table-top mode, this application uses a marker based system to determine the location of the virtual objects. The user is provided with science pages which contain information pertaining to the dataset along with an image which serves as the marker. Figure 41b shows the science sheet corresponding to the dataset in figure 41c. This particular dataset depicts NOAA's 1/4° daily optimal interpolation sea surface temperature anomaly during the years 2015 to 2016, showing the evolution of the recent El Niño event. When viewed through a mobile device running the application (Meteo-AR), the 3D dataset appears on the page, allowing the user to interact and explore the

dataset in MR. To view a different dataset, the user simply swaps the science sheet. The placement of the white dots along the border of the image is unique to each dataset (See figure 41b) and they help the application determine which dataset to render.

4.8 Summary

Augmented reality provides a data visualization environment which is natural and intuitive to use. In this study, the application of this technology in the field of atmospheric science is explored leveraging on the ubiquitous availability of smartphones and tablet computers, along with the current enthusiasm for general consumer head mounted displays. 'Lack of content creation tools' was one of the major limitations reported by research studies in the past (Bacca et al., 2014). The present study addresses this issue by demonstrating an application and presenting methodology utilizing, accessible game development platforms.

In an educational setting, augmented reality was found to be beneficial in teaching concepts involving spatial structures and studies from desperate disciplines have observed that augmented reality based educational tools fostered collaboration and increased student motivation towards the educational content (Radu, 2012). Further, given the increased interest and familiarity with mobile technology among the millennial generation, the proposed AR technology could be ideal for teaching atmospheric science concepts as well as in weather education and public outreach activities.

CHAPTER 5

CONCLUSIONS & FUTURE SCOPE

Environmental remote sensing has seen rapid growth in the recent years and Doppler wind lidars have gained popularity primarily due to their non-intrusive, high spatial and temporal measurement capabilities. While lidar applications early on, relied on the radial velocity measurements alone, most of the practical applications in wind farm control and short term wind prediction require knowledge of the vector wind field. Over the past couple of years, multiple works on lidars have explored three primary methods of retrieving wind vectors viz., using homogeneous windfield assumption, computationally extensive variational methods and the use of multiple Doppler lidars. These works highlight a tradeoff between the presence of complex flow and the complexity of the vector retrieval.

Building on prior research, the first section of the present study demonstrates the capabilities of single and dual Doppler lidar retrievals built on the least squares formulation as a part of the METCRAX II field campaign at the Barringer Crater in Arizona. Vertical profiles of wind speed and direction with 5m resolution were retrieved from RHI and VAD scans which played a vital role in capturing the strength and depth of the nocturnal katabatic drainage flow over the surrounding plain, which were identified as an important factor leading to the development of downslope windstorm-type flows observed inside the crater. To capture the intermittent downslope windstorm-type flows, a coplanar dual Doppler lidar retrieval was implemented along a vertical plane inside the crater. A lidar simulator that runs on a prior LES simulation of the crater was developed

to study the dependence of various lidar parameters on the spatial, temporal and retrieval errors, using which, the instrument setting which best capture the intermittent downslope flow events were determined. A validation study to assess the accuracy of all the retrievals was performed using data from other instruments in the field. While most of the retrievals performed well, profiles from RHI scans showed a relatively big error in the 'u' component. A Gaussian error propagation analysis identified the RHI scan separation and the low SNR of the measurements to be the likely source of this error. While the single Doppler lidar retrievals implemented in METCRAX II highlight their capabilities in a horizontally homogeneous windfield, they would fail in complex flow situations. An example of one such situation is the flow around wind farms.

With the advancement of wind turbine technology and increased energy needs in the past 30 years, large wind farms with several hundred MW capacities with multi row wind turbines situated even on complex terrain are becoming common. However, with wind farms of such capacity, wakes from turbines in leading rows have been observed to alter the flow, hampering the entrainment of momentum and restricting the wake recovery within the wind farm - Known as the deep array affect (Nygaard, 2014). These wakes are the primary cause of increased turbulence within the wind farm, which inturn increase the turbine loads and reduce power output of the wind farm. Previous studies have measured average power losses due to wakes to be of the order of 10-20% of the total power output (Barthelmie et al., 2009). The use of turbine wake models to characterize wakes have their limitations of either underestimating or overestimating wake losses (Barthelmie et al., 2009; Larson et al., 2013). Moreover, wake meander

caused by large scale flow structures in the ambient flow is often difficult to characterize by models alone. One way to address this issue would be to adaptively and collectively control the wind turbines to maximize the power output based on upstream flow measurements with a Doppler lidar. A Doppler lidar could be used scan the atmosphere upstream and within the wind farm to derive the wind vectors, which could then be used in an optimization routine to determine individual turbine parameters to maximize the power output of the wind farm. This optimization process must start with an efficient Doppler lidar vector retrieval method which needs to retrieve wind vectors in real-time while preserving small scale, local flow structures. To address this requirement, a novel 2D-VAR based single Doppler lidar vector retrieval was developed and tested on Lidar data in the present study.

The retrieval obtains the vector field by minimizing a cost function formulated from a set of constraint equations pertaining to the flow. The constraints pertain to the radial velocity advection equation, tangential velocity equation from derivatives of radial velocity and the background from VVP. Expressions to determine the weights for each of these constraints based on their relative importance and confidence within the retrieval domain, were formulated. This retrieval was applied on lidar data from the Alpha Ventus wind farm in the North sea and validated with the data obtained from a cup and vane anemometer installed on a nearby research platform FINO-1. The intercomparison study demonstrated the accuracy and computational efficiency of the retrieval, while capturing wakes and their meander over time.

With these improved capabilities of Doppler lidar, we now have access to 2D and 3D measurements of the atmosphere, which make the unseen structure in the flow visible. However, for tasks requiring the user to shift his/her focus away from the computer screen frequently (E.g., Pilots), this process of connecting two-dimensional on-screen graphics to a natural visual view of either an object or a three-dimensional flow field could often be tedious, if not misleading. Visualization in Mixed/Augmented reality (MR/AR) could address this issue by providing a visualization environment in which the data regarding the surrounding atmosphere could be displayed within the user's real world view by means of a head mounted, hand held device. While AR visualizations have seen applications ranging from marketing to healthcare and is an active research area, there have been very few applications in the field of atmospheric science. The few previous works comprised of either usability studies or demonstrations with specialized hardware on simulation data alone. The current study differs from the previous works by present an AR visualization technique to visualize real sensor data leveraging on the ubiquitous availability from smartphones, tablet computers, and popularity of consumer grade head-mounted displays. A methodology using commonly available, game development platforms for the application development is also presented. The concept was tested on lidar data from METCRAX II and some NCAR's Earth science datasets for education and outreach activities.

In conclusion, this work aims to highlight the capabilities and limitations of the current Doppler lidar vector retrievals, establish the foundations for a fast 2D-VAR vector retrieval and demonstrate a novel Mixed/Augmented Reality based data

visualization technique for atmospheric data. Apart from the possible application of the 2D-VAR in collective wind farm control techniques, the general idea of using a Variational formulation could eventually pave way to a multiple sensor fusion based retrieval.

Variational methods have their roots in data assimilation techniques, in which multiple observations are incorporated into the model to deduce the current state of the atmosphere. Similar concept could be used to assimilate measurements from multiple sensors in the field to improve the resolution and accuracy of the 2D-VAR method developed in this study. Consider the general formulation of the cost function ($\mathrm{J}(\mathbf{X})$) from chapter 3;

$$\mathrm{J}(\mathbf{X}) = \frac{1}{2\Omega}\int \left(\sum \mathrm{W}_i \mathrm{C}_i^2\right)\ d\Omega \tag{5.1}$$

where, C_i's are the different constraints with their weights given by W_i. Apart from the constraints described in this study, additional background constraints for the wind vector could be formulated incorporating measurements from other instruments in the field such as, point measurements from sonic anemometers, line measurements from tethersondes, measurements from automatic weather stations etc., to name a few. The differences in spatial and temporal resolutions can be factored in through the careful selection of the weights W_i . To this end, techniques used in statistical methods like optimal interpolation which estimates the weights based on the error covariance length scales could be implemented.

Another possible extension of the work presented in this study would be in the formulation of an advection corrected, dual Doppler lidar retrieval. Work with the lidar simulator in chapter 2 pointed to spatial and temporal errors to be the main contributors to the overall error in the retrieval. While spatial error is dependent on the range gate size, the temporal errors are dependent on the scan speed and pulse averaging used. Often times, it is imperative to have a slow scan speed and a higher pulse averaging, in order to obtain measurements with high SNR, making temporal errors inevitable. Moreover, large acquisition times could also lead to the eventual violation of the wind field homogeneity assumption. For instance, the downslope windstorm type flows that were being studied were only observed during quiescent nights when the ambient wind speed was low. Thus, almost all the IOPs were conducted during clear-calm nights with poor aerosol content. This necessitated longer acquisition times and higher pulse averaging for each beam measured by the lidar to obtain data of acceptable quality. One possible remedy is to apply the retrieval in a moving frame of reference as demonstrated by Gal-Chen (1982) on data from Doppler weather radars. In this method, sequential backscatter or radial velocity scans could be used in a Variational formulation to deduce the mean wind speed and direction. The individual measurements from each line of sight and range gate are then corrected for their actual location using the advection equation, before running the dual Doppler algorithm to retrieve the higher resolution wind vectors.

PUBLICATIONS FROM CURRENT RESEARCH

Journal Publications

[J1] **Cherukuru, N.,** R. Calhoun, T. Scheitlin, M. Rehme, and R. Kumar, 2016: Atmospheric Data Visualization in Mixed Reality. *Bulletin of the American Meteorological Society*. doi:10.1175/BAMS-D-15-00259.1 *(Impact factor: 7.9)*

[J2] **Cherukuru, N. W.**, Calhoun R, Lehner M, Hoch SW, Whiteman C; Instrument configuration for dual-doppler lidar coplanar scans: metcrax ii (2015). J. Appl. Remote Sens. 0001;9(1):096090. doi:10.1117/1.JRS.9.096090

[J3] **Cherukuru, N. W**., R. Calhoun, R. Krishnamurthy, S. Benny, J. Reuder: 2D VAR single Doppler LIDAR vector retrieval and its application in offshore wind energy, *Energy Procedia (accepted)*

[J4] Lehner, M., Whiteman, C. D., Hoch, S. W., Crosman, E. T., Jeglum, M. E., **Cherukuru, N. W**., Calhoun, R ... & Horst, T. W. (2015). The METCRAX II field experiment-A study of downslope windstorm-type flows in Arizona's Meteor Crater. *Bulletin of the American Meteorological Society*, 2016 97:2, 217-235 *(Impact factor: 7.9)*

Conference publications

[C1] **Cherukuru, N. W.,** R. Calhoun: Augmented Reality Based Doppler Lidar Data Visualization: Promises and Challenges. 27th Int. Laser Radar Conf., New York; 07/2015.

[C2] **Cherukuru, N. W**., R. Calhoun, M. Lehner, S. W. Hoch, C. D. Whiteman, and W. O. J. Brown, 2014: Instrument configuration for dual-Doppler LiDAR co-planar scans: METCRAX II. 16th Conf. Mountain Meteor., San Diego, CA, 18-22 August 2014

[C3] **Cherukuru, N. W**., R. Calhoun, R. Krishnamurthy, S. Benny, J. Reuder: 2D VAR single Doppler LIDAR vector retrieval and its application in offshore wind energy, 14th Deep Sea Offshore Wind R&D Conference, EERA DeepWind'2017, Trondheim, Norway, 18-20 Jan 2017

[C4] Chatterjee. T, **N. W. Cherukuru,** Y. Peet, R. Calhoun: Incorporating realistic geophysical effects of mean wind from LIDAR measurements in Large Eddy Simulation of Wind Turbine Arrays, 55th AIAA Aerospace Sciences Meeting/35th ASME Wind Energy Symposium, January 9 - 13 2017 Grapevine, TX

[C5] Hoch, S. W., **N. W. Cherukuru**, R. Calhoun, C. D. Whiteman, M. Lehner, and W. O. J. Brown, 2014: LiDAR observations during METCRAX-II. 16th Amer. Meteor. Soc. Conf. on Mtn Meteor., San Diego, CA, 18-22 August 2014

[C6] Hoch, S. W., **N. W. Cherukuru**, R. Calhoun, C. D. Whiteman, M. Lehner, B. Adler, N. Kalthoff, and W. O. J. Brown, 2015: LiDAR observations during METCRAX-II. 33rd International Conference on Alpine Meteorology, Innsbruck, Austria, 31 Aug-4 Sept 2015

[C7] Lehner, M., C. D. Whiteman, S. W. Hoch, **N. W. Cherukuru**, R. Calhoun, B. Adler, and N. Kalthoff, 2014: Downslope-windstorm-type flows in Arizona's Meteor Crater - Initial findings from METCRAX II. EGU General Assembly 2014, Vienna, Austria, 27 April - 2 May 2014

[C8] Whiteman, C. D. M. Lehner, S. W. Hoch, E. Crosman, M. Jeglum, **N. W. Cherukuru**, R. Calhoun, T. W. Horst, W. O. J. Brown, S. Semmer, R. Rotunno, N. Kalthoff, B. Adler, R. Vogt, and M. Grudzielanek, 2014: The second Meteor Crater Experiment (METCRAX II) - An overview of the October 2013 field study. 16th Amer. Meteor. Soc. Conf. on Mtn Meteor., San Diego, CA, 18-22 August 2014

[C9] Whiteman, C. D., M. Lehner, S. W. Hoch, M. O. G. Hills, N. Kalthoff, B. Adler, R. Rotunno, R. Vogt, I. Feigenwinter, M. Grudzielanek, J. Cermak, T. Haiden, **N. W. Cherukuru**, and R. Calhoun, 2015: The second Meteor Crater Experiment (METCRAX II): Introduction and overview of recent results. 33rd International Conference on Alpine Meteorology, Innsbruck, Austria, 31 August-4 September 2015.

REFERENCES

Adler, B., Whiteman, C. D., Hoch, S. W., Lehner, M., & Kalthoff, N. (2012). Warm-air intrusions in Arizona's Meteor Crater. *Journal of Applied Meteorology and Climatology*, *51*(6), 1010-1025.

Aragon, C. R., and Long, K. R., (2005): Airflow hazard visualization for helicopter pilots: Flight simulation study results. *Annual Forum Proceedings of American Helicopter Society*, **61,** 1, 1-17.

Armijo, L. (1966). Minimization of functions having Lipschitz continuous first partial derivatives. *Pacific Journal of mathematics*, *16*(1), 1-3.

Azuma, R. T., (1997): A survey of augmented reality. *Presence*, ***6,*** 4, 355-385.

Azuma, R., Baillot, Y., Behringer, R., Feiner, S., Julier, S., & MacIntyre, B. (2001). Recent advances in augmented reality. *IEEE computer graphics and applications*, *21*(6), 34-47.

Bacca, J., Baldiris, S., Fabregat, R., & Graf, S. (2014). Augmented reality trends in education: a systematic review of research and applications. *Journal of Educational Technology & Society*, *17*(4), 133.

Banta, R. M., Olivier, L. D., Gudiksen, P. H., & Lange, R. (1996). Implications of small-scale flow features to modeling dispersion over complex terrain. *Journal of Applied Meteorology*, *35*(3), 330-342.

Banta, R. M., Pichugina, Y. L., Brewer, W. A., Lundquist, J. K., Kelley, N. D., Sandberg, S. P., ... & Weickmann, A. M. (2015). 3D Volumetric Analysis of Wind Turbine Wake Properties in the Atmosphere Using High-Resolution Doppler Lidar. *Journal of Atmospheric and Oceanic Technology*, *32*(5), 904-914.

Barthelmie, R. J., Hansen, K., Frandsen, S. T., Rathmann, O., Schepers, J. G., Schlez, W., ... & Chaviaropoulos, P. K. (2009). Modelling and measuring flow and wind turbine wakes in large wind farms offshore. *Wind Energy*, *12*(5), 431-444.

Boccippio, D. J. (1995). A diagnostic analysis of the VVP single-Doppler retrieval technique. *Journal of Atmospheric and Oceanic technology*, *12*(2), 230-248.

Browning, K. A., & Wexler, R. (1968). The determination of kinematic properties of a wind field using Doppler radar. *Journal of Applied Meteorology*, *7*(1), 105-113.

Calhoun, R., Heap, R., Princevac, M., Newsom, R., Fernando, H., & Ligon, D. (2006). Virtual towers using coherent Doppler lidar during the Joint Urban 2003 dispersion experiment. *Journal of Applied meteorology and climatology*, *45*(8), 1116-1126.

Cariou, J. P., & Boquet, M. (2011). Leosphere pulsed lidar principles. *Leosphere, Orsay (FR)*, 1-32.

Carmigniani, J., & Furht, B. (2011). Augmented reality: an overview. In *Handbook of augmented reality* (pp. 3-46). Springer New York.

Caudell, T. P., & Mizell, D. W. (1992, January). Augmented reality: An application of heads-up display technology to manual manufacturing processes. In *System Sciences, 1992. Proceedings of the Twenty-Fifth Hawaii International Conference on* (Vol. 2, pp. 659-669). IEEE.

Chai, T., Lin, C. L., & Newsom, R. K. (2004). Retrieval of microscale flow structures from high-resolution Doppler lidar data using an adjoint model. *Journal of the atmospheric sciences*, *61*(13), 1500-1520.

Chan, P. W., & Shao, A. M. (2007). Depiction of complex airflow near Hong Kong International Airport using a Doppler LIDAR with a two-dimensional wind retrieval technique. *Meteorologische Zeitschrift*, *16*(5), 491-504.

Chan, P. W., & Yu, F. (2010). Application of Variational Analysis of Wind Field based on LIDAR Conical Scans to Air Quality Monitoring. *Open Atmospheric Science Journal*, *4*, 64-77.

Cherukuru, N. W., Calhoun, R., Lehner, M., Hoch, S. W., & Whiteman, C. D. (2015). Instrument configuration for dual-Doppler lidar coplanar scans: METCRAX II. *Journal of Applied Remote Sensing*, *9*(1), 096090-096090.

Cherukuru, N., R. Calhoun, T. Scheitlin, M. Rehme, and R. Kumar, (2016): Atmospheric Data Visualization in Mixed Reality. Bull. Amer. Meteor. Soc. doi:10.1175/BAMS-D-15-00259.1, in press.

Choukulkar, A., Calhoun, R., Billings, B., & Doyle, J. D. (2012). A modified optimal interpolation technique for vector retrieval for coherent Doppler lidar. *Geoscience and Remote Sensing Letters, IEEE*, *9*(6), 1132-1136.

Choukulkar, A., Calhoun, R., Billings, B., & Doyle, J. (2012). Investigation of a complex nocturnal flow in owens valley, california using coherent doppler lidar. *Boundary-layer meteorology*, *144*(3), 359-378.

Clifton, Andrew. (2015). Remote Sensing of Complex Flows by Doppler Wind Lidar: Issues and Preliminary Recommendations (Technical Report). *National Renewable Energy Laboratory,* NREL/TP-5000-64634.http://www.nrel.gov/docs/fy16osti/64634.pdf

Davies, F., Collier, C. G., & Bozier, K. E. (2005). Errors associated with dual-Doppler-lidar turbulence measurements. *Journal of Optics A: Pure and Applied Optics*, *7*(6), S280.

Doviak, R. J. & Zrnic, D. S. (1993). Doppler Radar and Weather Observations, 2nd ed. *Academic Press*, 304 pp.

Durran, D. R. (2003), "Downslope Winds", in *Encyclopedia of Atmospheric Sciences*, Holton, James R. Curry, Judith A. Pyle, John A., Volumes 1-6, pp. 644-650, Elsevier.

Eberhard, W. L., Cupp, R. E., & Healy, K. R. (1989). Doppler lidar measurement of profiles of turbulence and momentum flux. *Journal of Atmospheric and Oceanic Technology*, *6*(5), 809-819.

Frehlich, R., Hannon, S. M., & Henderson, S. W. (1994). Performance of a 2-μm coherent Doppler lidar for wind measurements. *Journal of Atmospheric and Oceanic Technology*, *11*(6), 1517-1528.

Frehlich, R., Hannon, S. M., & Henderson, S. W. (1998). Coherent Doppler lidar measurements of wind field statistics. *Boundary-Layer Meteorology*, *86*(2), 233-256.

Frehlich, R., & Kelley, N. (2008). Measurements of wind and turbulence profiles with scanning Doppler lidar for wind energy applications. *Selected Topics in Applied Earth Observations and Remote Sensing, IEEE Journal of*, *1*(1), 42-47.

Gal-Chen, T. (1982). Errors in fixed and moving frame of references: Applications for conventional and Doppler radar analysis. *Journal of the Atmospheric Sciences*, *39*(10), 2279-2300.

Gal-Chen, T., Xu, M., & Eberhard, W. L. (1992). Estimations of atmospheric boundary layer fluxes and other turbulence parameters from Doppler lidar data. *Journal of Geophysical Research: Atmospheres*, *97*(D17), 18409-18423.

Gal-Chen, T., & Zhang, J. (1993). On the optimal use of reflectivities and single Doppler radar velocities to deduce 3D motions. In *Preprints, 26th Int. Conf. on Radar Meteorology, Norman, OK, Amer. Meteor. Soc* (pp. 414-416).

Gao, J., Xue, M., Shapiro, A., & Droegemeier, K. K. (1999). A variational method for the analysis of three-dimensional wind fields from two Doppler radars. *Monthly weather review*, *127*(9), 2128-2142.

Gao, J., Xue, M., Shapiro, A., Xu, Q., & Droegemeier, K. K. (2001). Three-dimensional simple adjoint velocity retrievals from single-Doppler radar. *Journal of atmospheric and oceanic Technology*, *18*(1), 26-38.

Gao, J., Xue, M., Lee, S. Y., Shapiro, A., Xu, Q., & Droegemeier, K. K. (2006). A three-dimensional variational single-Doppler velocity retrieval method with simple conservation equation constraint. *Meteorology and Atmospheric Physics*, *94*(1-4), 11-26.

Heuveline, V., Ritterbusch, S., and Ronnas, S., (2013): Augmented Reality for Urban Simulation Visualization. *Int. J. Advances in Systems and Measurements*, **6**, 1, 26-39.

Hill, M., Calhoun, R., Fernando, H. J. S., Wieser, A., Dörnbrack, A., Weissmann, M., ... & Newsom, R. (2010). Coplanar Doppler lidar retrieval of rotors from T-REX. *Journal of the Atmospheric Sciences*, *67*(3), 713-729.

Horn, B. K., & Schunck, B. G. (1981, November). Determining optical flow. In *1981 Technical symposium east* (pp. 319-331). International Society for Optics and Photonics.

International Civil Aviation Organization (ICAO) (1998). International Standards and Recommended Practices, Annex 3 to the Convention of International Civil Aviation, Meteorological Service for International Air Navigation. Chapter 4, "Meteorological Observations and Reports." Thirteenth edition – July 1998

Koscielny, A. J., Doviak, R. J., & Rabin, R. (1982). Statistical considerations in the estimation of divergence from single-Doppler radar and application to prestorm boundary-layer observations. *Journal of Applied Meteorology*, *21*(2), 197-210.

Kring, D. A (2007). "Guidebook to the Geology of Barringer Meteorite Crater, Arizona (aka Meteor Crater)", Field guide for the 70th Annual Meeting of the Meteoritical Society. LPI Contribution no. 1355, Lunar and Planetary Institute, Houston, TX

Krishnamurthy, R., Calhoun, R., Billings, B., & Doyle, J. (2011). Wind turbulence estimates in a valley by coherent Doppler lidar. *Meteorological Applications*, *18*(3), 361-371.

Krishnamurthy, R., Choukulkar, A., Calhoun, R., Fine, J., Oliver, A., & Barr, K. S. (2013). Coherent Doppler lidar for wind farm characterization. *Wind Energy*, *16*(2), 189-206.

Lane, S. E., Barlow, J. F., & Wood, C. R. (2013). An assessment of a three-beam Doppler lidar wind profiling method for use in urban areas. *Journal of Wind Engineering and Industrial Aerodynamics*, *119*, 53-59.

Laroche, S., & Zawadzki, I. (1994). A variational analysis method for retrieval of three-dimensional wind field from single-Doppler radar data. *Journal of the atmospheric sciences*, *51*(18), 2664-2682.

Larsen, T. J., Madsen, H. A., Larsen, G. C., & Hansen, K. S. (2013). Validation of the dynamic wake meander model for loads and power production in the Egmond aan Zee wind farm. *Wind Energy*, *16*(4), 605-624.

Lehner, M., Whiteman, C. D., Hoch, S. W., Crosman, E. T., Jeglum, M. E., Cherukuru, N. W., ... & Horst, T. W. (2015). The METCRAX II field experiment-A study of downslope windstorm-type flows in Arizona's Meteor Crater. *Bulletin of the American Meteorological Society*.

Lewis, J. M., & Derber, J. C. (1985). The use of adjoint equations to solve a variational adjustment problem with advective constraints. *Tellus A*, *37*(4), 309-322.

Lhermitte, R. M., & Atlas, D. (1961, October). Precipitation motion by pulse Doppler radar. In *Proc. Ninth Weather Radar Conf* (pp. 218-223). Boston, MA: Amer. Meteor. Soc..

Lhermitte, R. M., & Miller, L. J. (1970, November). Doppler radar methodology for the observation of convective storms. In *Preprints, 14th Conf. on Radar Meteorology, Tucson, AZ, Amer. Meteor. Soc* (pp. 133-138).

Lucas, B. D., & Kanade, T. (1981, August). An iterative image registration technique with an application to stereo vision. In *IJCAI* (Vol. 81, pp. 674-679).

Lundquist, J. K., Churchfield, M. J., Lee, S., & Clifton, A. (2015). Quantifying error of lidar and sodar Doppler beam swinging measurements of wind turbine wakes using computational fluid dynamics. *Atmospheric Measurement Techniques*, *8*(2), 907-920.

Mann, J., Cariou, J. P., Courtney, M. S., Parmentier, R., Mikkelsen, T., Wagner, R., ... & Enevoldsen, K. (2008). Comparison of 3D turbulence measurements using three staring wind lidars and a sonic anemometer. In *IOP Conference Series: Earth and Environmental Science* (Vol. 1, No. 1, p. 012012). IOP Publishing.

Mayor, S. D., Lowe, J. P., & Mauzey, C. F. (2012). Two-Component Horizontal Aerosol Motion Vectors in the Atmospheric Surface Layer from a Cross-Correlation Algorithm Applied to Scanning Elastic Backscatter Lidar Data. *Journal of Atmospheric and Oceanic Technology*, *29*(11), 1585-1602.

Mikkelsen, T., Mann, J., Courtney, M., & Sjöholm, M. (2008). Windscanner: 3-d wind and turbulence measurements from three steerable doppler lidars. In *IOP conference series: earth and environmental science* (Vol. 1, No. 1, p. 012018). IOP Publishing.

Milgram, P., and Kishino, F., (1994): A taxonomy of mixed reality visual displays. *IEICE Transactions on Information and Systems*, **77**, 12, 1321-1329.

Mistry, P., Maes, P., & Chang, L. (2009, April). WUW-wear Ur world: a wearable gestural interface. In *CHI'09 extended abstracts on Human factors in computing systems* (pp. 4111-4116). ACM.

Newman, J. F., Bonin, T. A., Klein, P. M., Wharton, S., & Newsom, R. K. (2016). Testing and validation of multi-lidar scanning strategies for wind energy applications. *Wind Energy*.

Newman, J. F., Klein P. M., Wharton S., Sathe A., Bonin T. A., Chilson P. B., Muschinski A (2015). Evaluation of three lidar scanning strategies for turbulence measurements. *Atmospheric Measurement Techniques Discussions,* **8**: 12329–12381.

Newsom, R. K. (2012). *Doppler Lidar (DL) Handbook* (No. DOE/SC-ARM/TR-101). DOE Office of Science Atmospheric Radiation Measurement (ARM) Program (United States).

Newsom, R. K., & Banta, R. M. (2003). Shear-flow instability in the stable nocturnal boundary layer as observed by Doppler lidar during CASES-99. *Journal of the atmospheric sciences*, *60*(1), 16-33.

Newsom, R. K., & Banta, R. M. (2004a). Assimilating coherent Doppler lidar measurements into a model of the atmospheric boundary layer. Part I: Algorithm development and sensitivity to measurement error. *Journal of Atmospheric and Oceanic Technology*, *21*(9), 1328-1345.

Newsom, R. K., & Banta, R. M. (2004b). Assimilating coherent Doppler lidar measurements into a model of the atmospheric boundary layer. Part II: Sensitivity analyses. *Journal of Atmospheric and Oceanic Technology*, *21*(12), 1809-1824.

Newsom, R. K., Berg, L. K., Shaw, W. J., & Fischer, M. L. (2015). Turbine-scale wind field measurements using dual-Doppler lidar. *Wind Energy*, *18*(2), 219-235.

Newsom, R., Calhoun, R., Ligon, D., & Allwine, J. (2008). Linearly organized turbulence structures observed over a suburban area by dual-Doppler lidar. *Boundary-layer meteorology*, *127*(1), 111-130.

Newsom, R. K., Ligon, D., Calhoun, R., Heap, R., Cregan, E., & Princevac, M. (2005). Retrieval of microscale wind and temperature fields from single-and dual-Doppler lidar data. *Journal of applied meteorology*, *44*(9), 1324-1345.

Nurminen, A., Kruijff, E., and Veas, E., 2011: HYDROSYS–A mixed reality platform for on-site visualization of environmental data. *Web and Wireless Geographical Information Systems, **6574***, 159-175.

Nygaard, N. G. (2014). Wakes in very large wind farms and the effect of neighbouring wind farms. In *Journal of Physics: Conference Series* (Vol. 524, No. 1, p. 012162). IOP Publishing.

Qiu, C. J., Shao, A. M., Liu, S., & Xu, Q. (2006). A two-step variational method for three-dimensional wind retrieval from single Doppler radar. *Meteorology and Atmospheric Physics*, *91*(1-4), 1-8.

Qiu, C. J., & Xu, Q. (1992). A simple adjoint method of wind analysis for single-Doppler data. *Journal of Atmospheric and Oceanic Technology*, *9*(5), 588-598.

Qiu, C. J., & Xu, Q. (1996). Least squares retrieval of microburst winds from single Doppler radar data. *Monthly weather review*, *124*(6), 1132-1144.

Radu, I. (2012, November). Why should my students use AR? A comparative review of the educational impacts of augmented-reality. In *Mixed and Augmented Reality (ISMAR), 2012 IEEE International Symposium on* (pp. 313-314). IEEE.

Reed, S. E., Kreylos, O., Hsi, S., Kellogg, L. H., Schladow, G., Yikilmaz, M. B., ... & Sato, E. (2014, December). Shaping watersheds exhibit: An interactive, augmented reality sandbox for advancing earth science education. In *AGU Fall Meeting Abstracts* (Vol. 1, p. 01).

Rinehart, R. E., & Garvey, E. T. (1978). Three-dimensional storm motion detection by conventional weather radar. *Nature, 273, 287-289.*

Rolland, J. P., Holloway, R. L., & Fuchs, H. (1995, December). Comparison of optical and video see-through, head-mounted displays. In *Photonics for Industrial Applications* (pp. 293-307). International Society for Optics and Photonics.

Rothermel, J., Kessinger, C., & Davis, D. L. (1985). Dual-Doppler lidar measurement of winds in the JAWS experiment. *Journal of Atmospheric and Oceanic Technology*, *2*(2), 138-147.

Sasaki, Y. (1970a). Numerical variational analysis formulated under the constraints as determined by longwave equations and a low-pass filter. Mon. Wea. Rev, 98(12), 884-898.

Sasaki, Y. (1970b). Numerical variational analysis with weak constraint and application to surface analysis of severe storm gust. *Mon. Wea. Rev*, *98*(12), 899-910.

Sasaki, Y. (1970c). Some basic formalisms in numerical variational analysis. *Monthly Weather Review*, *98*(12), 875-883.

Sathe, A., Banta, R., Pauscher, L., Vogstad, K., Schlipf, D., & Wylie, S. (2015). Estimating Turbulence Statistics and Parameters from Ground-and Nacelle-Based Lidar Measurements. DTU Wind Energy

Sathe, A., Mann, J., Gottschall, J., & Courtney, M. S. (2011). Can wind lidars measure turbulence? *Journal of Atmospheric and Oceanic Technology*, *28*(7), 853-868.

Sathe, A., & Mann, J. (2013). A review of turbulence measurements using ground-based wind lidars. *Atmospheric Measurement Techniques*, *6*(11), 3147.

Sathe, A., Mann, J., Vasiljevic, N., & Lea, G. (2015). A six-beam method to measure turbulence statistics using ground-based wind lidars. *Atmospheric Measurement Techniques*, *8*(2), 729-740.

Savage, L. C., Zhong, S., Yao, W., Brown, W. J., Horst, T. W., & Whiteman, C. D. (2008). An observational and numerical study of a regional-scale downslope flow in northern Arizona. *Journal of Geophysical Research: Atmospheres*, *113*(D14).

Schols, J. L., & Eloranta, E. W. (1992). Calculation of area-averaged vertical profiles of the horizontal wind velocity from volume-imaging lidar data. *Journal of Geophysical Research: Atmospheres*, *97*(D17), 18395-18407.

Shapiro, A., Gal-Shen, T., Zhang, J., Zhao, L., Xu, Q., Gu, H., ... & Tuttle, J. (1995). Highlights from a single-Doppler velocity retrieval intercomparison project('bake-off'). In *Conference on Aviation Weather Systems, 6th, Dallas, TX* (pp. 541-546).

Shun, C. M. (2003). Ongoing research in Hong Kong has led to improved wind shear and turbulence alerts. *ICAO Journal*, *58*(2), 4-6.

Shun, C. M., & Chan, P. W. (2008). Applications of an infrared Doppler lidar in detection of wind shear. *Journal of Atmospheric and Oceanic Technology*, *25*(5), 637-655.

Siemen, S., & Holt, A. R. (2000). A modified VAD technique for analysing wind fields with Doppler radar. *Physics and Chemistry of the Earth, Part B: Hydrology, Oceans and Atmosphere*, *25*(10), 1201-1204.

Spera, D. A., and Richards T. R., "Modified power law equations for vertical wind profiles," in *Proceedings of the Conference and Workshop on Wind Energy Characteristics and Wind Energy Siting*, Portland, Ore, USA, June 1979.

Srivastava, R. C., Matejka, T. J., & Lorello, T. J. (1986). Doppler radar study of the trailing anvil region associated with a squall line. *Journal of the atmospheric sciences*, *43*(4), 356-377.

Stanimirovic, D., Damasky, N., Webel, S., Koriath, D., Spillner, A., & Kurz, D. (2014, September). [Poster] A Mobile Augmented reality system to assist auto mechanics. In *Mixed and Augmented Reality (ISMAR), 2014 IEEE International Symposium on* (pp. 305-306).

Stawiarski, C., Träumner, K., Knigge, C., & Calhoun, R. (2013). Scopes and challenges of dual-Doppler lidar wind measurements—an error analysis. *Journal of Atmospheric and Oceanic Technology*, *30*(9), 2044-2062.

Steptoe, W., Julier, S., & Steed, A. (2014, September). Presence and discernability in conventional and non-photorealistic immersive augmented reality. In *Mixed and Augmented Reality (ISMAR), 2014 IEEE International Symposium on* (pp. 213-218). IEEE.

Sun, J., Flicker, D. W., & Lilly, D. K. (1991). Recovery of three-dimensional wind and temperature fields from simulated single-Doppler radar data. *Journal of the Atmospheric Sciences*, *48*(6), 876-890.

Sutherland, I. E. (1968, December). A head-mounted three dimensional display. In *Proceedings of the December 9-11, 1968, fall joint computer conference, part I* (pp. 757-764). ACM.

Tang, W., Chan, P. W., & Haller, G. (2011). Lagrangian coherent structure analysis of terminal winds detected by lidar. Part I: Turbulence structures. *Journal of Applied Meteorology and Climatology*, *50*(2), 325-338.

Taylor, G. I. (1938, February). The spectrum of turbulence. In *Proceedings of the Royal Society of London A: Mathematical, Physical and Engineering Sciences* (Vol. 164, No. 919, pp. 476-490). The Royal Society.

Tuttle, J. D., & Foote, G. B. (1990). Determination of the boundary layer airflow from a single Doppler radar. *Journal of Atmospheric and oceanic Technology*, *7*(2), 218-232.

Van Krevelen, D., & Poelman, R. (2010). A Survey of Augmented Reality Technologies, Applications and Limitations. *The International Journal of Virtual Reality*, Vol. 9, No. 2.

Wang, H., Barthelmie, R. J., Clifton, A., & Pryor, S. C. (2015). Wind Measurements from Arc Scans with Doppler Wind Lidar. *Journal of Atmospheric and Oceanic Technology*, *32*(11), 2024-2040.

Werner, C. (2005). *Doppler wind lidar* (pp. 325-354). Springer New York.

Whiteman, C. D., & Whiteman J. G. (1974)., "An historical climatology of damaging downslope windstorms at Boulder, Colorado," *NOAA Technical report ERL,* 336-APCL 35, NOAA/ERL, Boulder, Colorado.

Whiteman, C. D., Muschinski, A., Zhong, S., Fritts, D., Hoch, S. W., Hahnenberger, M., ... & Clements, C. B. (2008). METCRAX 2006: Meteorological experiments in Arizona's Meteor crater. *Bulletin of the American Meteorological Society*, *89*(11), 1665.

Xia, Q., Lin, C. L., Calhoun, R., & Newsom, R. K. (2008). Retrieval of urban boundary layer structures from Doppler lidar data. Part I: Accuracy assessment. *Journal of the Atmospheric Sciences*, *65*(1), 3-20.

Xu, Q., & Gong, J. (2003). Background error covariance functions for Doppler radial-wind analysis. *Quarterly Journal of the Royal Meteorological Society*, *129*(590), 1703-1720.

Xu, Q., & Qiu, C. J. (1994). Simple adjoint methods for single-Doppler wind analysis with a strong constraint of mass conservation. *Journal of Atmospheric and Oceanic Technology*, *11*(2), 289-298.

Xu, Q., & Qiu, C. J. (1995). Adjoint-method retrievals of low-altitude wind fields from single-Doppler reflectivity and radial-wind data. *Journal of Atmospheric and Oceanic Technology*, *12*(5), 1111-1119.

Xu, Q., Qiu, C. J., & Yu, J. X. (1994). Adjoint-method retrievals of low-altitude wind fields from single-Doppler reflectivity measured during Phoenix II. *Journal of Atmospheric and Oceanic Technology*, *11*(2), 275-288

Zhang, J., & Gal-Chen, T. (1996). Single-Doppler wind retrieval in the moving frame of reference. *Journal of the atmospheric Sciences*, *53*(18), 2609-2623.

APPENDIX A

EQUIVALENCY FOR AVERAGED RETRIEVAL TECHNIQUE AND LEAST SQUARES ALGORITHM

Consider a cell in the domain that receives 'm' hits from lidar-1 and 'n' hits from lidar-2 within a specified time window. Eq. (A1) gives the relationship between the velocity components and the radial velocity for each instance.

$$\begin{aligned} u\cos\varphi_{1j} + w\sin\varphi_{1j} &= v_{r1j} \\ u\cos\varphi_{2k} + w\sin\varphi_{2k} &= v_{r2k} \end{aligned} \tag{A1}$$

Where u and w are the horizontal and vertical velocity components in the plane of scan, φ is the elevation angle and v_r is the radial velocity as seen by the lidar at the corresponding range gate. The subscripts 1 and 2 refer to lidar-1 and lidar-2 respectively. The subscripts j and k indicate each hit and they run from 1 to m and 1 to n respectively. A total of $(m+n)$ equations are obtained which can be solved for the velocity components using a least squares algorithm[11]. Eq. (A2) is the matrix representation of Eq. (A1).

$$\mathbf{AU} = \mathbf{R} \tag{A2}$$

Where $\mathbf{A}_{(m+n),2} = \begin{pmatrix} \cos\varphi_{1j} & \sin\varphi_{1j} \\ \cos\varphi_{2k} & \sin\varphi_{2k} \end{pmatrix}$, $\mathbf{U}_{\mathbf{2,1}} = \begin{pmatrix} u \\ w \end{pmatrix}$ and $\mathbf{R}_{(m+n),2} = \begin{pmatrix} v_{r1j} \\ v_{r2k} \end{pmatrix}$

One shortcoming of this approach is that, for large grid spacing, matrix '$\mathbf{A}$' could become ill-conditioned. This can be avoided by reducing the system of equations given in Eq. (A1) to just two equations as outlined below. Eq. (A2) can be written as:

$$(\mathbf{A^T WA})\mathbf{U} = \mathbf{A^T WR} \tag{A3}$$

$$(\mathbf{A^T WA})_{11} = \sum_{j=1}^{m} \widetilde{\mathrm{w}}_j \cos^2 \varphi_{1j} + \sum_{k=1}^{n} \widetilde{\mathrm{w}}_k \cos^2 \varphi_{2k},$$

$$(\mathbf{A^T WA})_{22} = \sum_{j=1}^{m} \widetilde{\mathrm{w}}_j \sin^2 \varphi_{1j} + \sum_{k=1}^{n} \widetilde{\mathrm{w}}_{\mathrm{k}} \sin^2 \varphi_{2k}$$

$$(\mathbf{A^T WA})_{12} = (\mathbf{A^T WA})_{21} = \sum_{j=1}^{m} \widetilde{\mathrm{w}}_j \cos\varphi_{1j} \sin\varphi_{1j} + \sum_{k=1}^{n} \widetilde{\mathrm{w}}_k \cos\varphi_{2k} \sin\varphi_{2k}$$

$$(\mathbf{A^T WR})_{11} = \sum_{j=1}^{m} \widetilde{\mathrm{w}}_j v_{r1j} \cos\varphi_{1j} + \sum_{k=1}^{n} \widetilde{\mathrm{w}}_k v_{r2k} \cos\varphi_{2k},$$

$$(\mathbf{A^T WR})_{21} = \sum_{j=1}^{m} \widetilde{\mathrm{w}}_j v_{r1j} \sin\varphi_{1j} + \sum_{k=1}^{n} \widetilde{\mathrm{w}}_k v_{r2k} \sin\varphi_{2k}$$

'**W**' is the weighting function matrix. Let $\widetilde{\varphi}_1$ and $\widetilde{\varphi}_2$ denote the angles made by the centroid of the cell with respect to each lidar. For small grid spacing, we can replace φ_{1j} & φ_{2k} with $\widetilde{\varphi}_1 \& \widetilde{\varphi}_2$. The linear system given in Eq. (A3) can now be written as

$$\begin{aligned}
&(m\,\overline{\mathrm{w}}_1 \cos^2\widetilde{\varphi}_1 + n\,\overline{\mathrm{w}}_2 \cos^2\widetilde{\varphi}_2)u + (m\,\overline{\mathrm{w}}_1 \cos\widetilde{\varphi}_1 \sin\widetilde{\varphi}_1 + n\,\overline{\mathrm{w}}_2 \cos\widetilde{\varphi}_2 \sin\widetilde{\varphi}_2)w = m\bar{v}_{r1} \cos\widetilde{\varphi}_1 + n\bar{v}_{r2} \cos\widetilde{\varphi}_2 \\
&(m\,\overline{\mathrm{w}}_1 \cos\widetilde{\varphi}_1 \sin\widetilde{\varphi}_1 + n\,\overline{\mathrm{w}}_2 \cos\widetilde{\varphi}_2 \sin\widetilde{\varphi}_2)u + (m\,\overline{\mathrm{w}}_1 \sin^2\widetilde{\varphi}_1 + n\,\overline{\mathrm{w}}_2 \sin^2\widetilde{\varphi}_2)w = m\bar{v}_{r1} \sin\widetilde{\varphi}_1 + n\bar{v}_{r2} \sin\widetilde{\varphi}_2
\end{aligned} \tag{A4}$$

Where, $\bar{v}_{r1}$ and $\bar{v}_{r2}$ are the mean radial velocities, given by $\bar{v}_{r1} = (1/m)\sum_{j=1}^{m}(\widetilde{\mathrm{w}}_j v_{r1})$ and $\bar{v}_{r2} = (1/n)\sum_{k=1}^{n}(\widetilde{\mathrm{w}}_k v_{r2})$. $\overline{\mathrm{w}}_1 \&$ $\overline{\mathrm{w}}_2$ are given by $\overline{\mathrm{w}}_1 = (1/m)\sum_{j=1}^{m}(\widetilde{\mathrm{w}}_j)$ and $\overline{\mathrm{w}}_2 = (1/n)\sum_{k=1}^{n}(\widetilde{\mathrm{w}}_k)$

On further simplification of Eq. (A4) and rearranging the terms in matrix form, we obtain

$$\begin{pmatrix} m\cos\tilde{\varphi}_1 & n\cos\tilde{\varphi}_2 \\ m\sin\tilde{\varphi}_1 & n\sin\tilde{\varphi}_2 \end{pmatrix}\begin{pmatrix} H_{11} \\ H_{21} \end{pmatrix} = 0_{2,1} \tag{A5}$$

Where $H_{11} = u\cos\tilde{\varphi}_1 + w\sin\tilde{\varphi}_1 - (\bar{v}_{r1}/\overline{\mathrm{w}}_1)$ and $H_{22} = u\cos\tilde{\varphi}_2 + w\sin\tilde{\varphi}_2 - (\bar{v}_{r2}/\overline{\mathrm{w}}_2)$. H_{11} and H_{21} are identically zero only when $mn\sin(\tilde{\varphi}_1 - \tilde{\varphi}_2) \neq 0$. Thus, when $m \neq 0, n \neq 0, \tilde{\varphi}_1 \neq \tilde{\varphi}_2$ and $(\tilde{\varphi}_1 + \tilde{\varphi}_2) \neq \pi$, Eq. (A1) can be replaced with,

$$\begin{aligned} u\cos\tilde{\varphi}_1 + w\sin\tilde{\varphi}_1 &= (\bar{v}_{r1}/\overline{\mathrm{w}}_1) \\ u\cos\tilde{\varphi}_2 + w\sin\tilde{\varphi}_2 &= (\bar{v}_{r2}/\overline{\mathrm{w}}_2) \end{aligned} \tag{A6}$$

APPENDIX B

QUASI NEWTON ALGORITHM FOR OPTIMIZATION

algorithm **Quasi-Newton method with Davidon-Fletcher-Powell method**

input: $\boldsymbol{X^0}, J(\boldsymbol{X^0}), \nabla J(\boldsymbol{X^0}), \boldsymbol{D^0}$

output: $\boldsymbol{X}$ at a local minimum of $J(\boldsymbol{X})$

$k = 0$

while $\|\nabla J(\boldsymbol{X}^k)\|_2 < \varepsilon$ *(or)* $|\Delta J(\boldsymbol{X}^k)| < \delta$

$\boldsymbol{D}^k = -\boldsymbol{H}^k \nabla J(\boldsymbol{X}^k)$

find 'α' using any 'Line-search algorithm'

$\boldsymbol{X}^{k+1} = \boldsymbol{X}^k + \alpha \boldsymbol{D}^k$

$\boldsymbol{a} = \boldsymbol{X}^{k+1} - \boldsymbol{X}^k$

$\boldsymbol{b} = \nabla J(\boldsymbol{X}^{k+1}) - \nabla J(\boldsymbol{X}^k)$

for each *grid point i*

$$\boldsymbol{H}_i^{k+1} = \boldsymbol{H}_i^k + \frac{\boldsymbol{a}\boldsymbol{a}^{\mathrm{T}}}{\boldsymbol{a}^{\mathrm{T}}\boldsymbol{b}}\bigg|_i - \frac{\boldsymbol{H}^k \boldsymbol{b}\boldsymbol{b}^{\mathrm{T}} \boldsymbol{H}^k}{\boldsymbol{b}^{\mathrm{T}} \boldsymbol{H}^k \boldsymbol{b}}\bigg|_i$$

end for

$\boldsymbol{H}^k = \boldsymbol{H}^{k+1}$

$k = k + 1$

end while

A simple backtracking line search algorithm (Armijo 1966) could be used to determine the optimal step size "α". (cont…)

algorithm **Line Search**

input: $J(\boldsymbol{X}), \nabla J(\boldsymbol{X}), \boldsymbol{D}, p, q$

output: optimal step size: α

while $J(\boldsymbol{X} + \alpha \boldsymbol{D}) > J(\boldsymbol{X}) + \sum p\alpha \nabla J(\boldsymbol{X})^{\mathrm{T}} \boldsymbol{D}$

$\alpha = q\alpha$

end while